Alma Mater Studiorum – Università di Bologna
in cotutela con **University of Iceland**

DOTTORATO DI RICERCA IN
SCIENZE DELLA TERRA

Ciclo XXVII

Settore Concorsuale di afferenza: 04 / A4
Settore Scientifico disciplinare: GEO 10

Characteristics and geological origin of earthquakes and tremor at Katla volcano (S-Iceland)

Presentata da
Giulia Sgattoni

Coordinatore Dottorato
Prof. Jo H. A. De Waele

Relatori
Dott. Federico Lucchi
Prof. Páll Einarsson

Co-relatore
Prof. Ólafur Guðmundsson

Esame finale anno 2016

ABSTRACT

Katla is a hazardous volcano in south Iceland, in large part covered by the Mýrdalsjökull glacier. It hosts a large caldera with several active geothermal areas and is characterised by persistent seismicity. Katla is one of the most active volcanoes in Iceland with at least 20 phreatomagmatic eruptions in the last 1100 years associated with catastrophic jökulhlaups. The last occurred in 1918. The present repose time is the longest known in history and the 2010 eruption of the neighbouring Eyjafjallajökull volcano prompted scientists' concerns because the two volcanoes are tectonically connected. The seismic network around Katla was therefore densified. No visible eruption occurred, but in July 2011 a 23 hour tremor burst was associated with a glacial flood which caused damage to infrastructure. This event was accompanied by deepening of the geothermally fed ice cauldrons, increased earthquake activity within the caldera and new seismicity on the south flank. The question arose whether or not a subglacial eruption occurred, i.e. whether the tremor was generated by magmatic processes or by the flood. Analysis of seismic data, including development of new location strategies, and a geological field study of the south flank were conducted to interpret the seismic sources and the volcanological significance of the 2011 unrest. July 2011 marked a change in the seismicity pattern at Katla that suggests a modification of the volcanic system. The tremor burst consisted of two phases originated at the active cauldrons and associated with hydrothermal or magmatic processes and a third phase generated by the flood. The increased seismicity rate inside the caldera and evidence of rapid melting of the glacier may indicate that the tremor was caused by a subglacial eruption. Alternatively, tremor may have been generated by hydrothermal boiling and/or explosions induced by the flood. An increase of heat released by the volcano is required in any case. The seismicity at the southern edge of the glacier in the Gvendarfell area consists of long-period repeating events occurring with regular time intervals, modulated by seasons (higher occurrence in summer). Because of the temporal evolution of the seismicity, hypocentre depth distribution, features of the glacier and coincidence with the 2011 unrest, volcano-related processes are considered more likely than glacial to generate this seismicity. A hydrothermal source may be easier to reconcile with the seasonal pattern than a magmatic one, although no direct indication of hydrothermal activity has been observed. A field survey revealed previously unknown flank eruption sites within the Gvendarfell area. Renewed volcano-related processes are therefore plausible and a magmatic source for the Gvendarfell events should not be discarded. This observation is of major importance for hazard assessment of the south flank of Katla. This work highlights the difficulty of discerning glacial and volcanic signals for the study and monitoring of subglacial volcanoes.

Contents

1. INTRODUCTION

Subglacial volcanoes are particularly hazardous as magma-ice interaction can produce highly explosive eruptions often associated with catastrophic jökulhlaups (glacial floods). This was exemplified by the 2010 Eyjafjallajökull summit eruption and its associated jökulhlaup that caused major air traffic disruption, despite its mild-explosive character. The study and monitoring of subglacial volcanoes is therefore crucial, but problematic, as it cannot count on field-based methods and indirect information such as seismic data has to be used. Moreover, a number of different seismic signals can be recorded at glacier-clad volcanoes, in association with both volcanic and glacial processes. It is very important to be able to discern between these different signals and processes, particularly in Iceland, where a number of large volcanoes are covered by ice. Katla volcano, in south Iceland, is a prime example.

The Katla volcanic system consists of a central volcano mostly covered by the Mýrdalsjökull ice cap and a 75 km long fissure swarm extending to the north east of the central volcano. The central volcano hosts a caldera up to 14 km wide entirely covered by the glacier, with several active geothermal areas forming depressions on the ice surface (ice cauldrons). Katla is one of Iceland's most active and hazardous volcanoes as its eruptive activity is characterized by frequent hydromagmatic eruptions. At least 300 subglacial explosive eruptions are known during the Holocene, 20 of which have occurred with an average repose time of 47 years since AD 1500 (Larsen, 2000; Óladóttir et al., 2005). The last verified eruption occurred almost 100 years ago, in 1918, and the current repose time is the

longest known in history (Larsen, 2000). The seismic behaviour of Katla is different from other Icelandic volcanoes, consisting of anomalously intense and persistent seismicity, even during periods of volcanic quiescence. Most of its seismicity, consisting of VT (Volcano-Tectonic; Chouet, 2003; McNutt, 2005), hybrid and LP (Long-Period; Chouet, 2003) events, has been primarily recorded within the summit caldera and along the western flank of Mýrdalsjökull named Goðabunga (Einarsson, 1991; Einarsson and Brandsdóttir, 2000; Sturkell et al., 2010). Katla, therefore, offers a wide variety of seismic signals to obtain insight into the volcano's internal dynamics.

Katla's eruptive activity appears to be connected to the neighbouring Eyjafjallajökull volcano (Einarsson and Hjartardóttir, 2015). For this reason, the 2010 Eyjafjallajökull's eruption enhanced scientists' concerns regarding a possible eruption at Katla and the seismic network around the volcano was densified. Although no visible eruption occurred, increased seismicity within the caldera and a 23 hour tremor burst were recorded on July 8-9th 2011, associated with deepening of several ice cauldrons on the ice cap and a jökulhlaup from the south-eastern caldera rim, which swept away a bridge and a part of the main road to eastern Iceland. The question arose whether or not this episode was related to a minor subglacial eruption not breaking the ice, i.e. whether the tremor was generated by magmatic processes or by the flood. Moreover, in coincidence with the 2011 unrest, a new cluster of LP seismic events was detected on the south flank, just west of the Gvendarfell ridge, around 4 km south of the caldera. Being located in a partly glaciated area, they may be associated with either volcanic or glacial processes. Seismic events in this area of Katla had never been recorded before and they are important when assessing Katla's volcanic hazard, as the south coast of Iceland is a farming area and a popular tourist destination.

In light of these events, the main research objectives presented in this thesis are i) characterization and geological interpretation of the new seismicity on Katla's south flank, ii) understanding the volcanological significance of the 2011 unrest and associated seismicity. This was done by analysing seismic data from a dense seismic network consisting of 10 permanent stations operated by the Icelandic Meteorological Office (IMO) and 9 temporary stations deployed by Uppsala University between July 2011 and August 2013. Moreover, three additional stations were deployed during the summer of 2014 on the south flank, in order to better constrain the absolute location of the Gvendarfell seismic cluster. In addition, the location of this seismic cluster at the edge of the glacier, encouraged a pilot field study of the Gvendarfell area, aimed at identifying the main geological and tectonic features possibly connected with seismic sources.

Although the LP events located on Katla's south flank resemble in some aspects those of other volcanoes, they show some peculiar characteristics, especially in their time evolution,

which have not been previously described. A detailed analysis of the seismic sequence was carried out, in terms of waveform characteristics, temporal evolution, first motion description, non-linear absolute location and relative relocation of the hypocenters. The relocation strategy was specifically designed to minimize and carefully evaluate the uncertainty, in order to obtain meaningful results in terms of size and shape of the seismic cluster.

The tremor signal that occurred in July 2011 was analysed together with the associated earthquake activity. The time evolution of tremor attributes, such as amplitude and frequency, compared with direct hydrological observations and the evolution of the earthquake activity were used to constrain the possible origin. Cross-correlation methods were used to locate the tremor source(s), including a new double-correlation approach.

Subsequently, the 2011 seismic event was placed in the broader context of Katla's geology, eruption and seismic history, by integrating literature information, analysis of the IMO seismic catalogue from 1998 and geological observations carried out in the Gvendarfell area.

References

Chouet. B.A., 2003. Volcano Seismology. Pure appl. geophys. 160, 739-788.

Einarsson, P., 1991. Earthquakes and present-day tectonism in Iceland. Tectonophysics 189, 261–279.

Einarsson, P., Brandsdóttir, B., 2000. Earthquakes in the Mýrdalsjökull area, Iceland, 1978–1985: Seasonal correlation and relation to volcanoes. Jökull 49, 59–73.

Einarsson, P., Hjartardóttir, Á. R., 2015. Structure and tectonic position of the Eyjafjallajökull volcano, S-Iceland. Jökull, in press.

Larsen, G., 2000. Holocene eruptions within the Katla volcanic system, south Iceland: characteristics and environmental impact. Jökull 49, 1–28.

Óladóttir, B.A., Larsen, G., Thordarson, Th., Sigmarsson, O., 2005. The Katla volcano, S-Iceland: holocene tephra stratigraphy and eruption frequency. Jökull 55, 53–74.

McNutt, S.R., 2005. Volcanic Seismology, Ann. Rev. Earth Planet. Sci. 33. doi: 10.1146/annurev.earth.33.092203.122459

Sturkell, E., Einarsson, P., Sigmundsson, F., Hooper, A., Ófeigsson, B. G., Geirsson, H., Ólafsson, H., 2010. Katla and Eyjafjallajökull Volcanoes. In: Schomacker, A., Krüger, J., Kjær, K.H. (Eds). The Mýrdalsjökull icecap, Iceland. Glacial processes, sediments and landforms on an active volcano. Developments in Quaternary Science 13. Elsevier, Amsterdam. ISBN 1571-0866, pp. 5–21.

2. STRUCTURE OF THE THESIS

The thesis is organized in 4 main chapters, each consisting of a paper manuscript already submitted or ready to be submitted for publication, and an additional last chapter with general conclusions. The topics and methodology covered by each main chapter are here summarized:

- Chapter 3, the Gvendarfell seismic cluster: Submitted paper that describes the seismicity in terms of waveform characteristics, temporal evolution and absolute location of the cluster and discusses possible source interpretations. Correlation methods were used to improve event detection in the continuous seismic record in order to study in detail the temporal evolution of the sequence. A detailed analysis of the waveform characteristics at different stations and through time was carried out, including a first motion description of the source. The absolute location of the cluster was obtained with a non-linear location method using a local network installed during the summer of 2014. Possible source interpretations are discussed in this chapter, based on observations and comparison with other volcanoes worldwide.
- Chapter 4, relative relocation of the Gvendarfell seismic events: Submitted paper that describes the relative relocation methodology that was developed in order to estimate the size and shape of the hypocentre distribution and their implication for the source interpretation. The proposed relocation strategy was designed to optimize both cross-correlation measurements (to obtain differential-time measurements used for relative relocation) and the relative relocation. A synthetic test was set up to determine the best

parameters for differential-time measurements and to estimate their uncertainties, specifically for each waveform. Differently than the usual relocation approaches that rely on a 1D velocity model, the relocation strategy here presented was designed to work without a predefined velocity model, by formulating and inverting the problem to seek changes in both location and slowness. This approach inverts for azimuth, take-off angles and velocity deviations from a 1D model. The inversion was solved explicitly in order to propagate data errors through the calculation.

- Chapter 5, the July 2011 tremor episode and earthquake activity inside the caldera: Paper manuscript ready to be submitted. The 23 hour tremor signal that occurred in July 2011 was analysed together with the associated earthquake activity using data from 10 seismic stations, 3 of which were located on the caldera rim. The signal was described in its frequency/amplitude features and their temporal evolution. Back-projection of cross-correlation envelopes was used to locate the tremor sources. A double-correlation technique is proposed and compared with the common single-correlation approach. The seismic observations were integrated with hydrological data in order to suggest possible interpretations of the tremor sources.
- Chapter 6, the July 2011 unrest episode and its volcanological implications: Paper manuscript ready to be submitted describing the seismological, geological and eruption history context of the 2011 unrest at Katla. The changes in the seismicity pattern that occurred in 2011 were analysed based on the IMO seismic catalogue from 1998 to 2015. A review of the main features of the Katla volcanic system is presented, together with geological observations carried out in the Gvendarfell area, volcanological implications of the 2011 unrest at Katla and possible source processes for the seismic activity.

3. PAPER 1

Long-period events with strikingly regular temporal patterns on Katla volcano's south flank (Iceland)

Giulia Sgattoni[1,2,3*], Zeinab Jeddi[3,4], Ólafur Guðmundsson[3], Páll Einarsson[2], Ari Tryggvason[3], Björn Lund[3], Federico Lucchi[1]

[1] Department of Biological, Geological and Environmental Sciences, University of Bologna, Bologna, Italy

[2] Institute of Earth Sciences, Science Institute, University of Iceland, Reykjavik, Iceland

[3] Department of Earth Sciences, Uppsala University, Uppsala, Sweden

[4] CNDS, Centre for Natural Disaster Science, Uppsala University, Uppsala, Sweden

**Corresponding author:* giulia.sgattoni2@unibo.it

Submitted to *Journal of Volcanology and Geothermal Research*

Abstract

Katla is a threatening volcano in Iceland, partly covered by the Mýrdalsjökull ice cap. The volcano has a large caldera with several active geothermal areas. A peculiar cluster of long-period seismic events started on Katla's south flank in July 2011, during an unrest episode in the caldera that culminated in a glacier outburst. The seismic events were tightly clustered at shallow depth in the Gvendarfell area, 4 km south of the caldera, under a small glacier stream on the southern margin of Mýrdalsjökull. No seismic events were known to have occurred in this area before. The most striking feature of this seismic cluster is its temporal pattern, characterized by regular intervals between repeating seismic events, modulated by a seasonal variation. Remarkable is also the stability of both the time and waveform features over a long time period, around 3.5 years. No comparable examples have been found in the literature. Both volcanic and glacial processes can produce similar waveforms and therefore have to be considered as potential seismic sources. Discerning between these two causes is critical for monitoring glacier-clad volcanoes and has been controversial at Katla. For this new seismic cluster on the south flank we regard volcano-related processes as more likely than glacial ones for the following reasons: 1) the seismic activity started during an unrest episode involving sudden melting of the glacier and a jökulhlaup; 2) the glacier stream is small and stagnant; 3) the seismicity remains regular and stable for years; 4) there is no apparent correlation with short-term weather changes, such as rain storms. We suggest that a small, shallow hydrothermal system was activated on Katla's south flank in 2011, either by a minor magmatic injection or by changes of permeability in a local crack system.

Keywords: Katla volcano, Iceland, long-period earthquakes, volcanic processes, glacial processes

1. Introduction

Katla is one of the most active and threatening volcanoes in Iceland. Partly covered by Mýrdalsjökull glacier, its volcanic activity has been dominated by large explosive phreatomagmatic eruptions, the last occurring in 1918. The current repose time is the longest known in history (Larsen, 2000). Katla is located just east of Eyjafjallajökull and the two volcanoes appear to be tectonically connected (Einarsson and Brandsdóttir, 2000). Several cases are known in history when Katla's eruption followed its neighbour's. For this reason, the 2010 Eyjafjallajökull eruption prompted scientists' concerns about a possible imminent Katla's eruption and the seismic network around the volcano was densified.

Seismic events at volcanoes are highly variable in terms of waveforms and temporal sequence evolution. They can be generated by multiple, geothermal, volcanic or tectonic processes. LP events (Long-Period; Chouet, 1996) are of particular interest as they often accompany or precede volcanic eruptions, but they are still not well understood (Chouet, 2003; McNutt, 2005). They can be related to a number of different magmatic and hydrothermal processes, usually associated with fluid movements inside the volcano. Recent studies offer new modelling of LP events as slow-rupture failure in unconsolidated volcanic materials (Bean et al., 2014).

As Katla is largely covered by Mýrdalsjökull glacier, extending over a ~600 km^2 area and entirely covering the summit caldera, direct field studies are not feasible and indirect methods such as seismic data analysis are important to study and monitor the volcano. Katla offers a wide variety of seismic signals to obtain insight into the volcano's internal dynamics. In this respect, it is an unusual volcano in Iceland because of its anomalously high and persistent seismicity (even during volcanic quiescence) despite its tectonic location, out of the main deformation zones. The only other Icelandic volcanoes comparable to Katla with respect to intense seismicity are located along the plate boundaries (Hengill and Bárðarbunga volcanoes; Einarsson, 1991; Jakobsdóttir, 2008).

Most of Katla's seismicity, consisting of VT (Volcano-Tectonic; Chouet, 2003; McNutt, 2005) and LP events, has primarily been recorded in two distinct source areas (e.g. Sturkell et al., 2010): i) within the summit caldera and ii) in a region in western Mýrdalsjökull named Goðabunga (Fig. 1). In July 2011, though, this general pattern changed. An increase in seismicity and a 23 hour tremor burst were recorded on July 8-9th 2011, associated with deepening of ice cauldrons on the ice cap and flooding from the south east rim of Mýrdalsjökull glacier that destroyed a bridge on the main road. At the same time, a new cluster of LP seismic events was detected on the south flank, just west of the Gvendarfell rise, around 4 km south of the caldera rim. Seismic events in this area of Katla had never been recorded before and they are of major interest when assessing Katla's volcanic hazard, as the south coast of Iceland is a farming area and a popular tourist destination.

At subglacial volcanoes, seismic events associated with glaciers (such as basal slip, ice falls, crevassing) and shallow low-frequency earthquakes associated with volcanic activity can produce similar waveforms (Métaxian et al., 2003; West et al., 2010; Thelen et al., 2013). The ability to distinguish between such sources is critical for monitoring glacier-clad volcanoes. In this respect, Katla aroused controversial interpretations of its seismicity, for its subglacial location and for the unusually frequent occurrence of LP seismicity during periods of volcanic quiescence (Soosalu et al., 2006; Jónsdóttir et al., 2009).

Although the LP events located on Katla's south flank in some aspects resemble those of other volcanoes, they show some peculiar characteristics, especially in their time evolution, which we have not found described in the literature. These are the subjects of the paper herein. The improved seismic network operating around Katla during 2011-2013 provided a good dataset for this purpose. Moreover, in order to improve the location estimates of these events further, a temporal deployment of three stations was done in 2014 in the epicentral area, in order to better define the absolute location of the cluster. We used cross-correlation methods to improve the event detection, thus highlighting striking time-sequence features, and a probabilistic non-linear method for the absolute location of the cluster. We also attempted to retrieve the focal mechanisms from first motion polarities.

2. Study area

The Katla volcanic system is located just south of the intersection between the East Volcanic Zone and the transform boundary of the South Iceland Seismic Zone (Sturkell et al., 2008). It consists of a central volcano with a 110 km^2 summit caldera (up to 14-km wide; Fig. 1) covered by Mýrdalsjökull glacier (Björnsson et al., 2000) and the Eldgjá fissure system which extends 75 km to the northeast (Larsen, 2000; Thordarson et al., 2001; Fig. 1). The central volcano's activity is dominated by explosive phreatomagmatic eruptions due to magma-ice interaction. Several ice cauldrons (at least 16) are located within and at the caldera rim, representing the surface expression of subglacial geothermal activity. Changes in their geometry are monitored to detect variations of geothermal heat release (Guðmundsson et al., 2007).

Seismic undershooting within the Katla caldera has revealed a zone where P wave velocities are reduced and S waves are absent; this anomaly is interpreted as evidence of a magma chamber (Guðmundsson et al., 1994). Moreover, results from an aeromagnetic survey indicate the presence of a non-magnetic body within the region of the postulated magma chamber (Jónsson and Kristjánsson, 2000). This is supported by geobarometry analyses on historical tephra samples, conducted by Budd et al. (2014), but questioned by tephra stratigraphy studies by Óladóttir et al. (2008).

Since the first sensitive seismographs were installed (in the 1960s), seismic activity has been observed in two distinct main areas: within the caldera and at Goðabunga on the western flank (Einarsson and Brandsdóttir, 2000). The seismicity inside the caldera consists of high frequency and hybrid events, probably associated with the subglacial geothermal activity (Sturkell et al., 2010) and volcano-tectonic processes. The Goðabunga cluster consists mainly of long-period shallow events and has a controversial interpretation, as a response to a slowly-

rising viscous crypto-dome (Soosalu et al., 2006) or in association with ice fall events (Jónsdóttir et al., 2009). Katla's seismicity shows a seasonal variation which is stronger at Goðabunga, where the peak occurs in autumn. A less pronounced peak of activity in the caldera occurs instead during the summer (July/August; Jónsdóttir et al., 2007). This seasonal correlation has been interpreted either as a result of ice-load change and resulting pore-pressure change at the base of the glacier (Einarsson and Bransdóttir, 2000) or as enhanced glacial motion during periods of distributed subglacial water channels (Jónsdóttir et al., 2009).

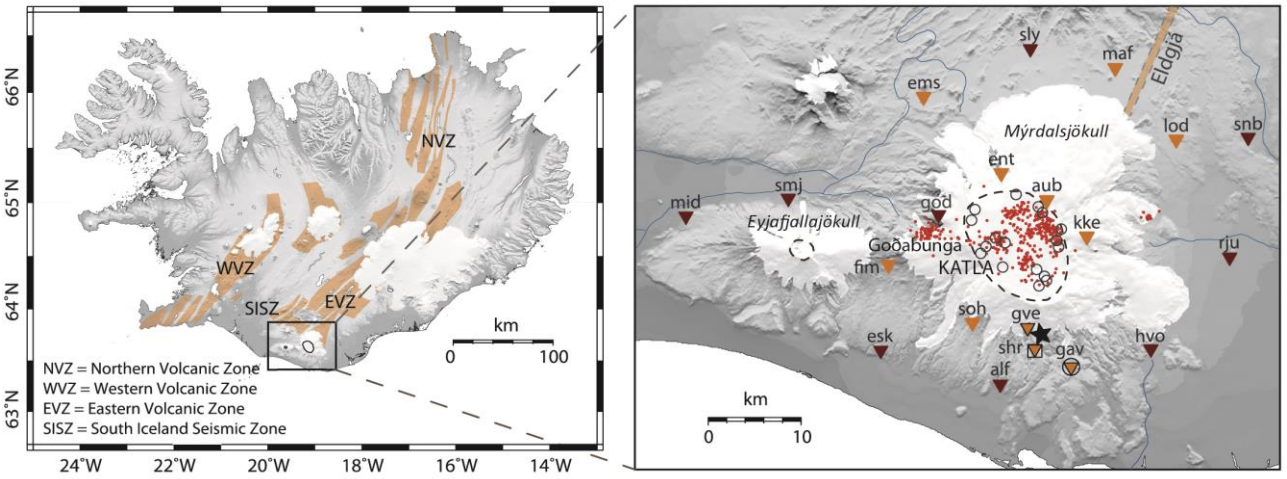

Fig. 1. Map of Iceland showing the different volcanic systems (in orange; from Einarsson and Sæmundsson, 1987) and the different segments of the plate boundary. In the inset, the seismic network and main seismic and geological features of Katla are shown. Dark brown triangles: permanent IMO seismic stations. Orange triangles: temporary Uppsala University seismic stations operating between July 2011-August 2013 (no outline) and between July 2014-August 2014 (black outline). The black open circle marks a temporary station (GAV) that has been operating on both time periods. The black square at station SHR on the south flank indicates the location of a GPS station operating in summer 2014. Red dots: seismic clusters at Katla before July 2011. These are mostly localized in two distinct source areas, within the caldera and on the western flank at Goðabunga. The star marks the new cluster on the south flank. The Katla and Eyjafjallajökull caldera rims are outlined by dashed lines. Open circles correspond to ice cauldrons (Guðmundsson et al., 2007). White areas are glaciers. To the NE, the location of Eldgjá fissure is shown.

Although no visible eruptions have occurred after 1918, evidence of unrest was observed in 1955, 1999 and 2011, possibly associated with minor subglacial eruptions. In 1955 this probably took place at the eastern rim of the caldera: two shallow ice-cauldrons formed and a small jökulhlaup (glacial flood) drained from Kötlujökull, south-east Mýrdalsjökull (Thorarinsson, 1975; Rist, 1967). A similar event took place in July 1999: the seismic stations around the glacier recorded earthquakes and bursts of tremor that culminated in the release of a jökulhlaup from Sólheimajökull, south-west Mýrdalsjökull (Sigurðsson et al., 2000;

Roberts et al., 2003). A new cauldron also formed on the surface of the glacier (Guðmundsson et al., 2007).

From 1999 to 2004, GPS measurements on nunataks exposed on the caldera edge revealed steady uplift of the volcano, interpreted to result from 0.01 km^3 magma accumulation (Sturkell et al., 2006; 2008). A recent study by Spaans et al. (2015), suggested instead that the uplift may be due to glacial isostatic adjustment as a consequence of mass loss of Iceland's ice caps. Guðmundsson et al. (2007) showed that increased geothermal heat output occurred in 2001-2003, based on the evolution of ice cauldrons. As this was also accompanied by greatly increased seismicity and ground uplift, they interpreted these phenomena as a result of magma accumulation and consequent dilation of the edifice leading to enhanced permeability and increased geothermal activity, in accordance with Sturkell et al. (2006).

3. The unrest episode of July 2011

Between August 2010 and July 2011, most of the ice cauldrons on the Mýrdalsjökull glacier uplifted by 6-8 m, interpreted by Guðmundsson et al. (2013) as water accumulation under the glacier. The greatest rise, 11-12 m was observed at cauldron 16 (Fig. 2; Guðmundsson et al., 2013).

In July 2011, the seismicity intensified at Katla and remained high until winter. The unrest culminated on July 8-9th when a burst of tremor was recorded by the Icelandic Meteorological Office (IMO) seismic network. No signs of eruption breaking the ice were seen, but a jökulhlaup drained from Kötlujökull and deepening of some ice cauldrons was observed on the surface of Mýrdalsjökull in the southern and eastern parts of the caldera (Fig. 2).

The tremor burst lasted for about 23 hours, beginning at about 19:00 GMT on July 8th. The jökulhlaup (~18 million m^3) swept away the bridge over Múlakvísl river around 05:00 GMT on July 9th, one hour after rising water level was detected at the gauging station Léreftshöfuð, located a few km south of Kötlujökull (IMO, 2011) and ~6 km upstream from the bridge (Fig. 2). Another gauging station, located on the bridge over Múlakvísl river on the main road 1 (Fig. 2), began to show increased conductivity early on July 8th (IMO, 2011).
This unrest episode has been interpreted in association with volcanic processes, such as enhanced geothermal activity, shallow magma intrusion or possibly a minor subglacial eruption (Sgattoni et al., 2015).

The earthquake activity accompanying these events was mainly concentrated inside the caldera, mostly in its south-eastern part. The tremor also originated inside the caldera, in a similar location to the earthquakes (Sgattoni et al., 2015). In addition, a new source of

seismic events was activated on the south flank, near Gvendarfell rise, at the southern edge of Mýrdalsjökull glacier (Hafursárjökull), around 4 km south of the southern caldera rim (Fig. 2).

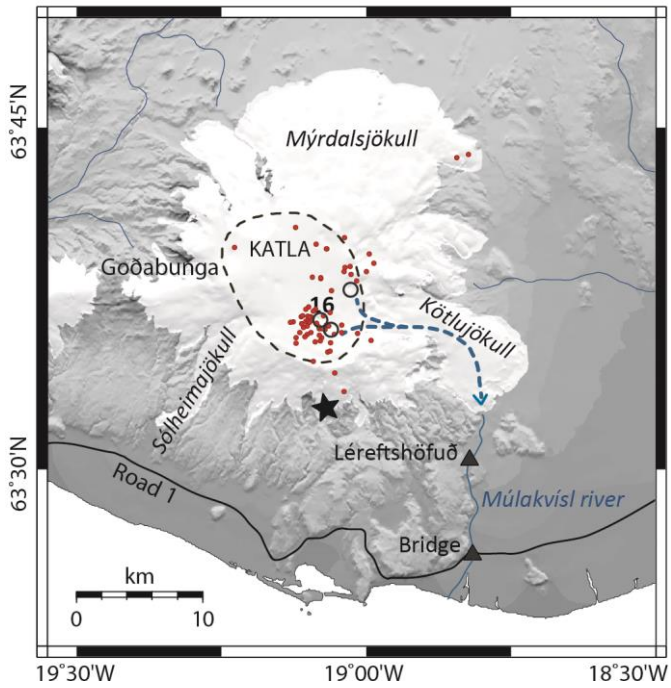

Fig. 2. Map of Katla showing the features related to the July 2011 unrest. Black open circles are the ice cauldrons that deepened during the unrest. Number 16 is the cauldron that showed biggest changes before and during the unrest. The dashed blue arrow shows the presumed flood path. Red dots are the earthquakes that occurred on July 8th and 9th. The 2 gauging stations are marked with black triangles; the southern one corresponds to the bridge over Múlakvísl river. The star marks the southern seismic cluster which is studied herein.

4. Seismic network and data

Following the eruption of Eyjafjallajökull volcano in 2010, the IMO augmented the seismic monitoring network around Katla from 5 to 9 stations. Moreover, 9 temporary stations were deployed by Uppsala University between July 2011 and August 2013.

Most of the stations were equipped with broadband sensors, 5 Guralp ESPA , 4 Guralp CMG3-ESPC and 1 Geotech KS-2000(LLC), all with flat response from 60 s to the Nyquist frequency (50 Hz). 5-second Lennartz populated the remaining 8 stations. Data were recorded and digitized with Guralp and Reftek systems at 100 sps. Stations were powered with batteries, wind generators and solar panels. All the instruments recorded in continuous mode, but some technical problems (e.g. power failure) mainly due to harsh weather condition (especially in winter time), prevented some stations from working continuously during the whole operation time.

During the operation time of the dense network described above, the closest station to the Gvendarfell cluster, object of this study, was GAV, around 6 km away. Therefore, the hypocentral location was poorly constrained, especially in depth (uncertainty on the order of a km). Since this seismicity continued with similar characteristics, we decided to install two additional stations, around 1 and 2 km away from the source, during the summer of 2014 to improve the hypocentral location of the cluster. Station GAV was also reactivated to minimize biases in hypocentral estimations caused by the change in network geometry. In addition, a GPS station was deployed during the same period (Fig. 1).

5. Waveform characteristics

The Gvendarfell seismicity is characterized by small magnitude (~ -0.5-1.2 M_L), long-period earthquakes with an emergent P wave and unclear (usually not identified) S wave (Fig. 3).

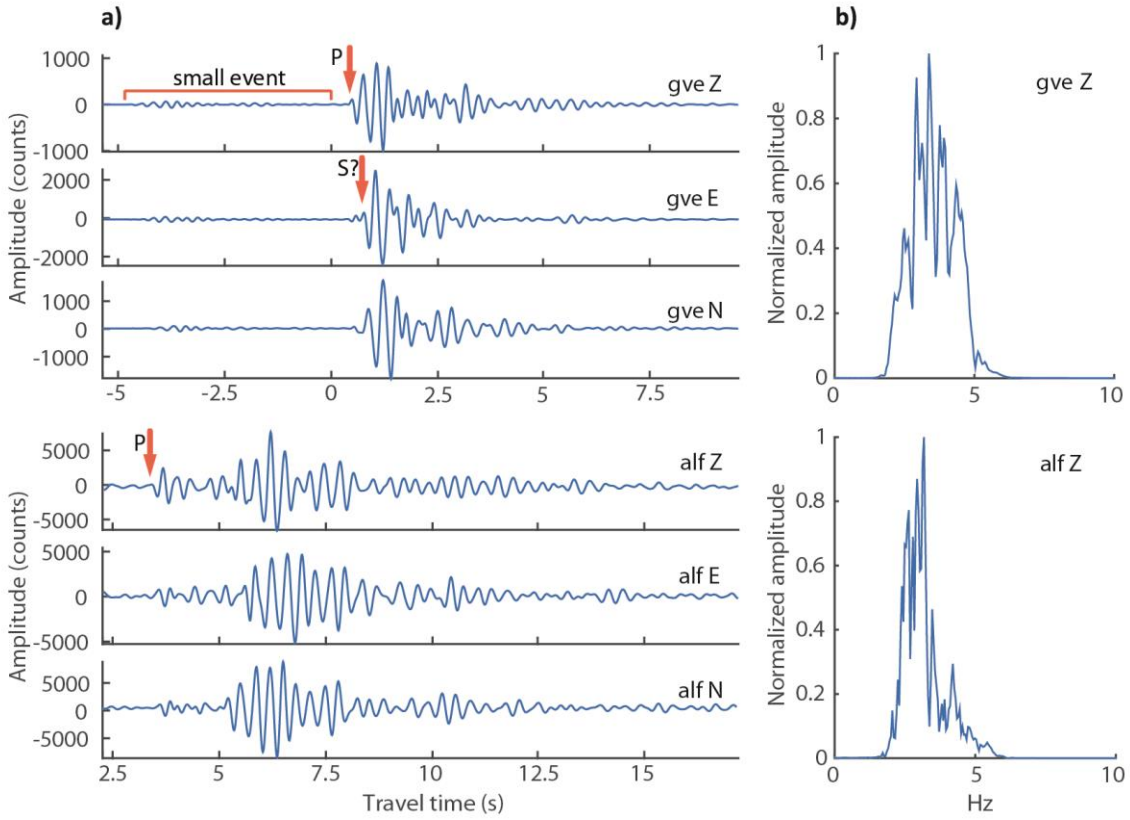

Fig. 3. a) Example seismograms of two different events at stations GVE and ALF. Notice the small event before the main one at GVE. The amplitude unit is digital counts, proportional to velocity. The arrows mark the P and S wave arrivals, where identified. b) Normalised amplitude spectra of the Z component at stations GVE and ALF.

All events have remarkably similar, nearly identical waveforms with correlation coefficient ≥ 0.9 at the nearest stations. Fig. 4 shows examples of waveforms throughout the whole time period, starting from March 2011, when the first small events were recorded. The similarity of the waveforms is striking and only slight changes can be noticed, from August 2012. The frequency content is narrow banded around 3-4 Hz at the closest station GVE and nearly monochromatic around 3 Hz at most other stations (Figs. 3 and 4).

The signals are characterized by a number of distinct seismic phases that we tried to interpret with particle motion plots. This however didn't help to discern and understand the different phases, which appear to be generated by interference of direct and scattered waves propagating in a heterogeneous medium. The complexity of the waveforms and their duration are therefore highly dependent on the distance from the source. A 6-7 sec long wave-train recorded at ~1 km distance, becomes more than 20 sec long, at 30-40 km. This is indicative of strong path effects, generating a number of secondary phases that increase the complexity of the seismograms (Fig. 5).

Another interesting feature is that the larger events were often preceded by smaller events, only recorded by the closest station GVE. At more distant stations, the small events disappear into the background noise (Fig. 3).

6. Time evolution

Visual observation of the seismic data indicated that a significant improvement in detectability could be achieved, compared with the IMO catalogue. As the waveforms are highly repeatable, cross-correlation of a sample waveform with continuous data was applicable to improve the event detection (cf. Lindblom et al., 2015 for a description of the correlation method). For this purpose we used data from station ALF, as it is close to the source and has been working continuously since February 2011. The best event in terms of signal to noise ratio was chosen from the IMO catalogue as a reference event (occurred on Oct 10th, 2011). Its waveform was band-pass filtered between 2-4 Hz and a 3 second window starting 0.5 sec before the P wave arrival was cross-correlated with the continuous data from February 2011 to August 2013. Around 1800 events were detected with a cross-correlation coefficient higher than 0.9 (mostly ≥ 0.95), significantly more compared to the 720 events of the IMO catalogue (Fig. 6). All the events were checked for possible false detections and visual inspection of 3 months of data proved that the cross-correlation analysis detected all visible events successfully. Moreover, in order to check whether other similar events had occurred also before 2011, data from station ESK (operating at Katla before the network was augmented) were used for cross-correlation with continuous data from 2010. In this case, no events were

detected that matched a minimum correlation coefficient threshold set as 0.7. This confirms that seismic activity at Gvendarfell was absent before 2011.

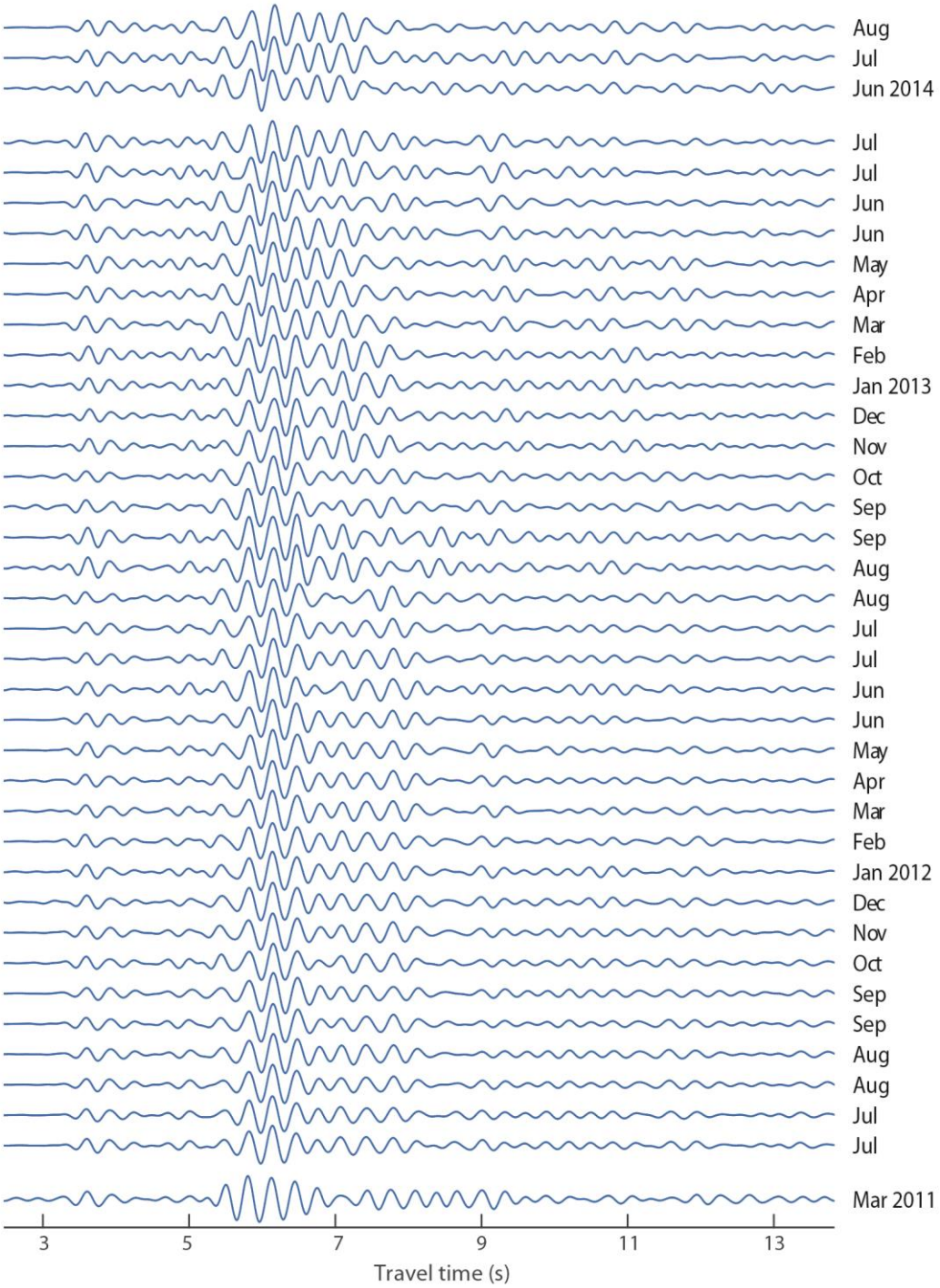

Fig. 4. Example waveforms of the Z component at station ALF (~6 km from the source) throughout the entire period of study, showing their similarity. One event per month is shown for cold seasons and two events per month for warm seasons.

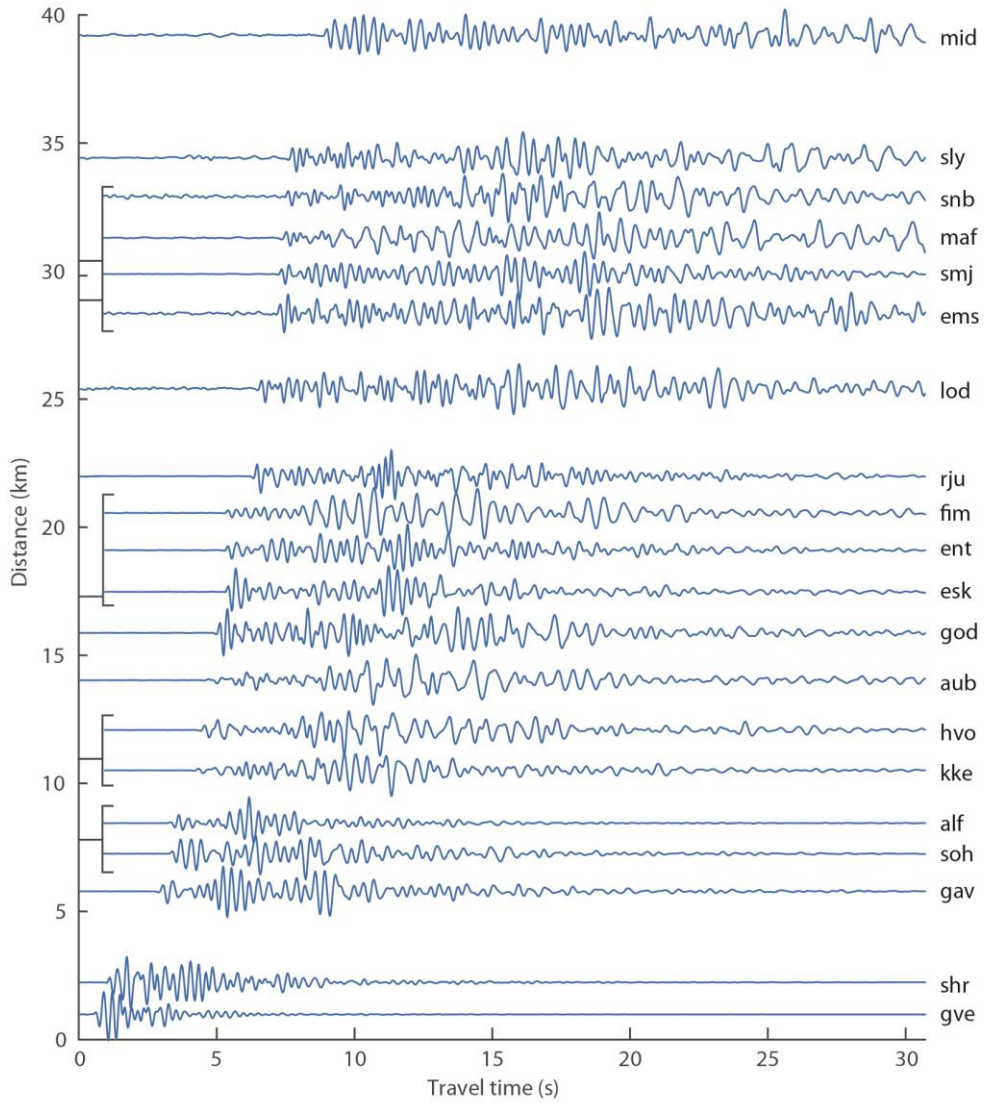

Fig. 5. Stacked Z component seismograms of all events recorded at each station. The approximate epicentral distance is reported on y-axis.

The local magnitude ML of the events was evaluated by calibrating the amplitude at ALF with the IMO magnitude estimation (moment magnitude Mw and local magnitude ML). The events overlapping between our improved catalogue and the IMO catalogue were used as a reference. Fig. 7 shows a logarithmic plot of the maximum amplitude at ALF versus ML, showing a clear linear relation. A line fitting of the ML plot was used to translate ALF amplitudes (from our catalogue) into magnitudes (Fig. 7a).

The first Gvendarfell events detected at ALF occurred in March 2011 and were very small, around 0.2 ML. A sudden increase in magnitude occurred on July 7th and a striking time feature started on this day: a regular time pattern with 6 events per day at 4 hour intervals began a few hours before the tremor burst of the 2011 unrest episode (Fig. 9). Before

that time, this pattern was not observed. A seasonal variation in the event rate is also observed, with maximal activity in late summer 2011, 2012 and 2013, which could not be discerned from the IMO catalogue (Figs. 6, 8a and 9). This correlation is not as clear in the cumulative moment release plot (Fig. 8b), showing a sharp increase in the summer of 2011 and less clear increases in the following summers. The regular event rate is observed also during periods of lower activity, with occurrence frequency gradually decreasing to 1 event every 1-2 days in winter and then increasing again to the maximum rate (6 to 8 events per day, depending on the year) during summer (Fig. 9). No diurnal variability or correlation with precipitation rates have been observed. This pattern is seen for the whole time period analysed in this article (July 2011-August 2014), although the clearest regularity is observed during the summer of 2011. Some exceptions to this general pattern can be noticed, for example in March 2013 (Fig. 8a), when a small swarm of events was recorded, not correlated with any volcanic/geothermal or meteorological event. According to the latest data from IMO, the seismic activity at Gvendarfell seems to be fading out and became insignificant in February 2015.

The amplitude behaviour with time also has interesting features. It increased by a factor of 10 at the onset of the tremor and stayed high for a year (Fig.8). After 1 year, the amplitude decreased by a factor of 2. A non-monotonic size distribution is also observed, with small events occurring in the background, mainly during periods of high seismic activity (Figs. 8a and 9). The regular time pattern is mainly observed for the class of larger events, whereas smaller events seem to occur at more random time intervals (Fig. 9), however this could be due to incompleteness of the catalogue below $M_L = 0$.

Fig. 10 shows the relation between the magnitude and the cumulative number of events. The size of the events does not follow the conventional empirical relation of Gutenberg-Richter ($\log N = a - bM$). The non-monotonic size of the events shows up clearly in the non-cumulative plot in Fig. 10, with a peak around $M_L = 1$ and a minimum around $M_L = 0.4$. Another peak is present at around $M_L = 0$. It is not clear if this is simply caused by incompleteness at magnitudes < 0 or if this is a feature of the physical distribution. Note that it is impossible to estimate the magnitude of completeness in this case because the earthquakes do not follow any standard model.

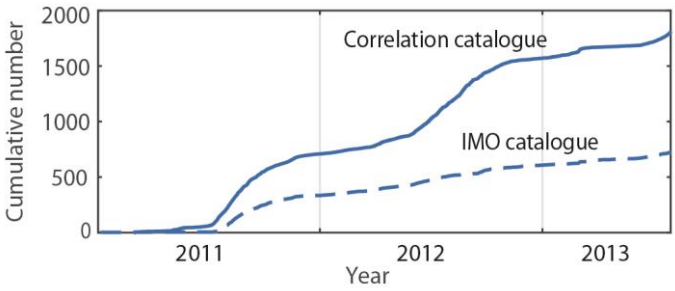

Fig. 6. Cumulative number of events at Gvendarfell. The event detection of the catalogue obtained with cross-correlation is highly improved. A seasonal variation, with more events during warm seasons (corresponding to the steeper segments of the curve), is also clear on the top curve.

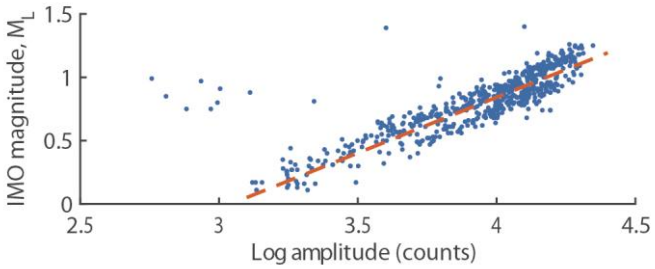

Fig. 7. Magnitude calibration. The maximum log amplitude at station ALF is plotted for all events of our catalogue overlapping with IMO catalogue. Linear correlation between ALF amplitude and IMO local magnitude, M_L. The dashed line is the line fitted to the data to convert amplitudes to M_L.

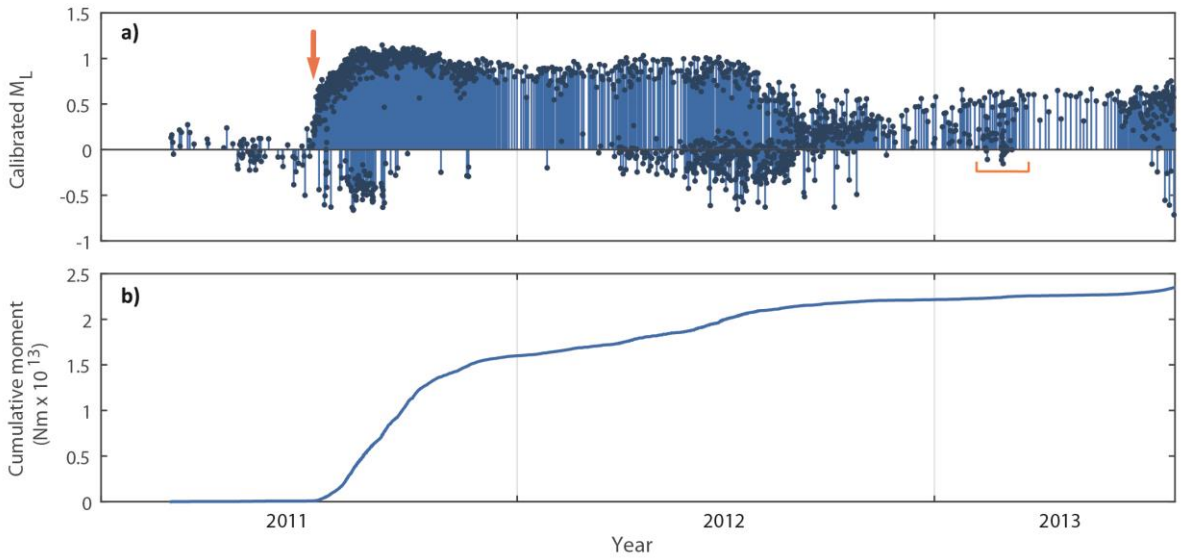

Fig. 8. a) Magnitude (M_L) - time evolution of the Gvendarfell seismic sequence between January 2011 and July 2013. The arrow indicates the time of the tremor burst (July 8th-9th). The March 2013 swarm is also outlined (orange squared line). b) Cumulative seismic moment release in the same time interval as panel (a). The moment-magnitude relation used is $\log M_0 = 1.5M + 9.1$, where M_0 is the moment and M is the magnitude. As we don't have an estimation of Mw, we used M_L in this relation. Therefore, our estimates of seismic moment are uncertain.

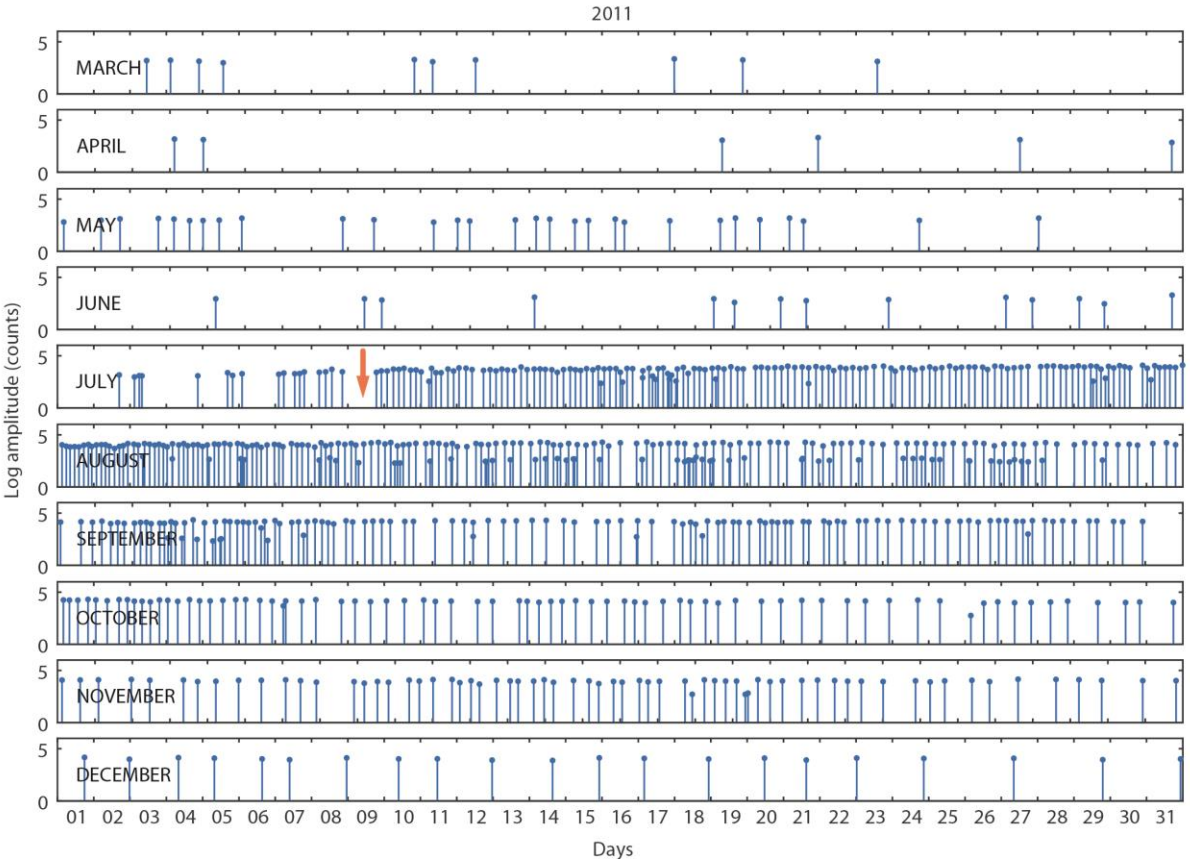

Fig. 9. Time evolution of the Gvendarfell seismic sequence in 2011. The arrow indicates the time of the tremor burst, same as Fig. 8, corresponding to the beginning of the regular time pattern. Inter-event times vary between 4 hours in July-August to 1-2 days in December.

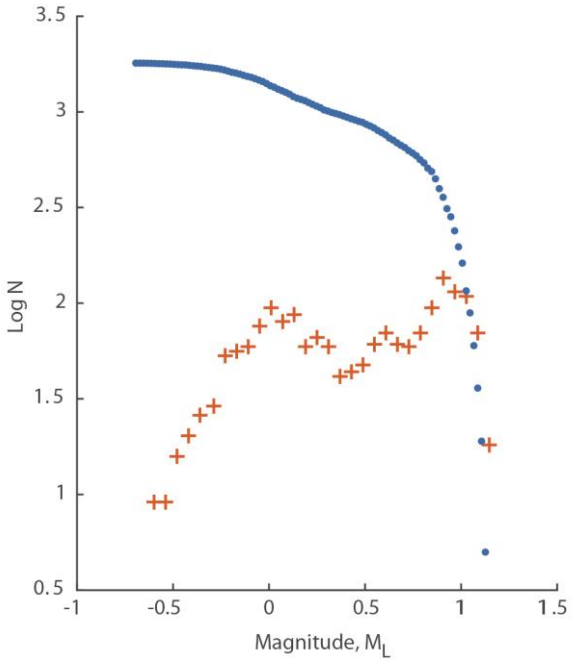

Fig. 10. Magnitude (M_L) – number (log N) relation, both cumulative (dots) and non-cumulative (crosses).

7. Absolute location

The absolute locations from the IMO catalogue show a cloud of hypocentres, dispersed over a large area, several km in diameter (Fig. 11) around the Hafursárjökull glacial valley, on the southern side of Mýrdalsjökull glacier. However, the similarity of all the waveforms suggests a much smaller distribution of foci, which we can crudely estimate by requiring the phase difference to be smaller than a fraction of a period, in order to explain such high correlation. By taking this fraction as a quarter of a wavelength and assuming a dominant frequency of 3.5 Hz and an average velocity of 3.5 km/s, we can infer the maximum size of the hypocentre distribution to be ≤ 250 m. Reported uncertainty is on the order of 1 km in the horizontal and several km in the vertical, i.e. smaller than the distribution of locations, suggesting that significant and variable (because of changes in station geometry) bias due to three-dimensional heterogeneity is present in the locations.

7.1 Non-linear location method

We selected the best recorded events during the summer of 2014 (when 2 additional stations were deployed nearby) to be relocated. For this we used a probabilistic, non-linear method, mapping the likelyhood function for each event around the centre of the IMO location cloud with an exhaustive grid search (Lomax et al., 2000). The error distributions of arrival-time data and their predictions are assumed to be Gaussian. The error is not known. A distance weighting is assigned for stations farther than 3 km from the source to simulate increasing uncertainty with increasing distance. This defines a data covariance matrix, less an unknown scaling. This scaling is estimated based on the residual variance at minimum misfit and thus represents the combined error of observation and prediction. The velocity model used is one dimensional and based on tomographic results in the area (Jeddi et al. 2015). Scalar station corrections (estimated based on time residuals) are introduced to absorb effects of lateral heterogeneity with an iterative procedure, starting from no corrections and iterating until converging to stable corrections.

The grid search extended over a 5x5 km^2 area around the average IMO location of the events recorded in 2011-2013, down to 5 km depth, with 50 m resolution in the horizontal directions and 100 m in the vertical. As the phase composition of the wave forms is unclear (as explained above), particular care was taken when picking the P and S arrival times. The P wave was carefully identified first in the stacked wave forms and then consistently in the individual events (details of the stacking are explained below). The S wave was only picked at

the closest station, GVE. The iterative process of relocation and station-correction estimation converged at the second iteration. The resulting rms correction was 0.17 sec.

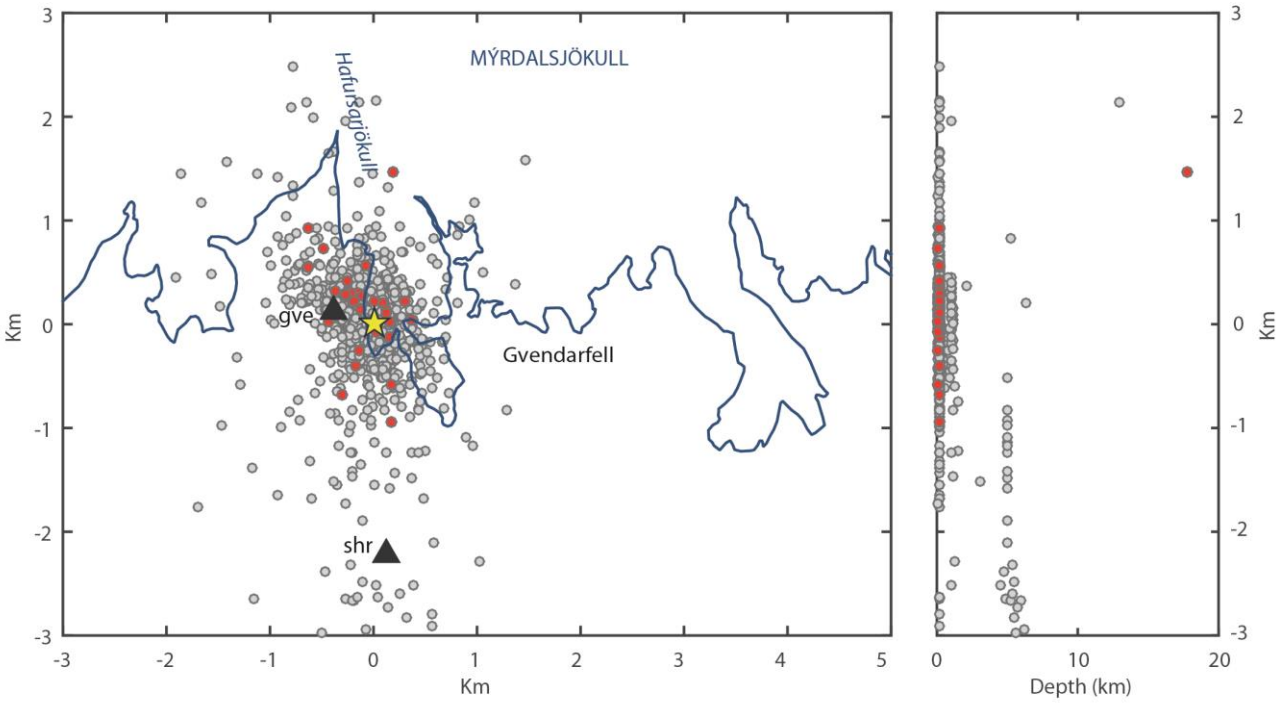

Fig. 11. Locations and depth distribution of the Gvendarfell seismic events, from IMO catalogue: grey = all locations 2011-2013; red = 30 events in summer 2014, same relocated with nonlinear method (see Fig. 12). The star is the average IMO location (N63º32.772', W19º06.588') and corresponds to the origin of the axes of Fig. 12. Black triangles are the seismic stations. The glacier outline (in blue) is derived from LiDAR DEM obtained in 2010 (Jóhannesson et al., 2013).

7.2 Location results

Fig. 12 shows the resulting combined probability density of the hypocentre locations. The origin of the coordinate system is the average IMO location (at N63º32.772' and W19º06.588') and depth is referred to the average elevation in the source region (at 800 m.a.s.l.). Our relocations do not differ much from the IMO average, except for a ~500 m shift to the east. The distribution of hypocentres is much smaller than in the IMO catalogue locations (Figs. 11 and 12a). The uncertainty of the relocations is around 400 m in the horizontal dimensions and 500-600 m in depth, as inferred from the probability distributions of the locations of single events (Fig. 12b). The cluster appears to be located in the shallow sub surface, between 0.5 and 0.9 km depth. It is clear from comparing Fig. 12a, showing the combined distribution of the cluster, and Fig. 12b, showing the distribution for an individual event, that the cluster distribution is dominated by the uncertainty. Therefore, the cluster may be much smaller in extent than Fig. 12a suggests. The eastward shift of the centre of

mass of the distribution compared to the average IMO location is marginally resolved. The depth is marginally resolved to differ from zero. A clear correlation (trade off) is persistent between depth and easting. This is controlled by the station geometry, with the nearest station GVE, yielding S picks, a few km to the west-northwest. Some trade off exists between depth and origin time, but inclusion of S picks from station GVE reduces that significantly.

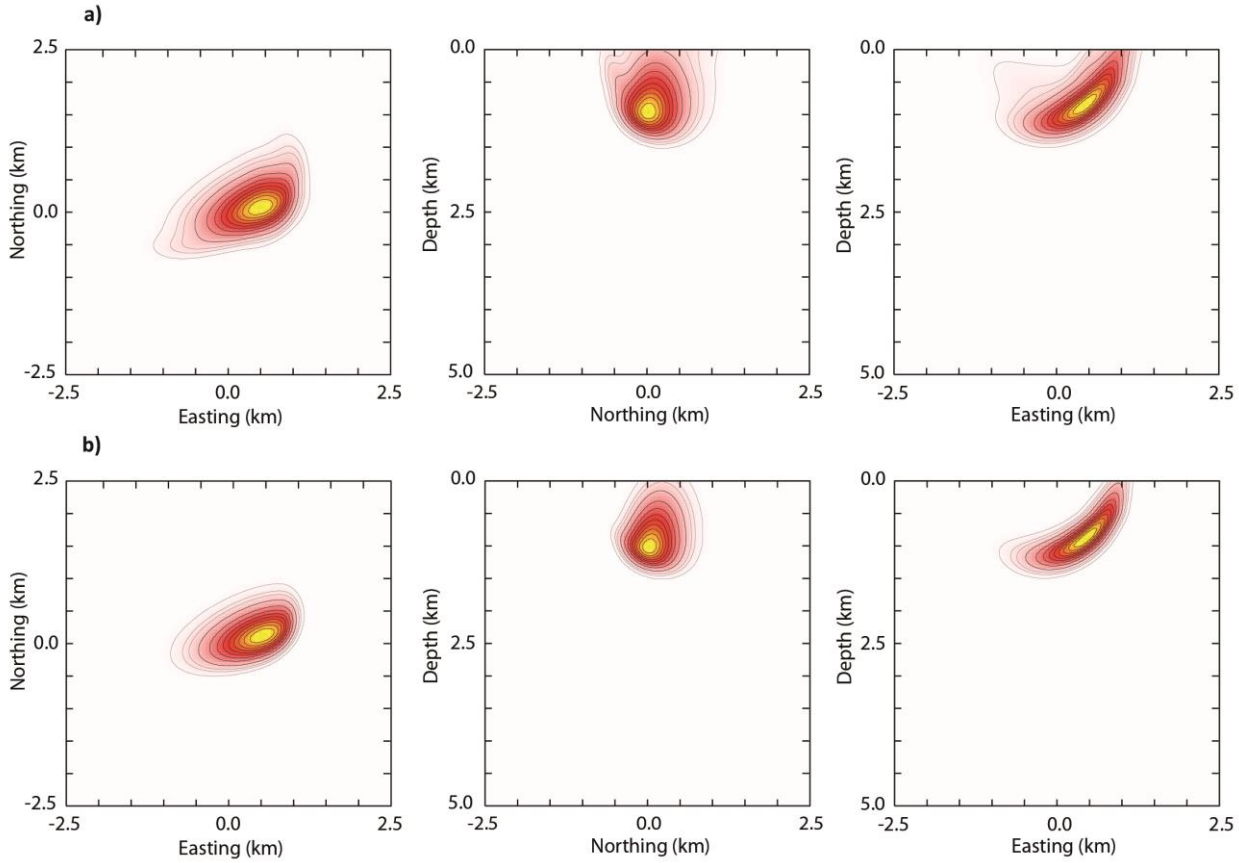

Fig. 12. a) Non-linear locations of the Gvendarfell seismic events: combined probability density of all locations (34 events in total occurred in summer 2014). b) Probability density of the location of one example event, to show the single event uncertainty. The scale is normalised and the density ranges from 1 (yellow, in the centre of the distribution) to zero (white). The black contour lines correspond to 0.9 – 0.1 with 0.1 spacing. The grey contour lines are 0.05, 0.03, 0.01.

8. Focal mechanisms

Although we do not know what kind of source generates the Gvendarfell events, we tried to obtain some description of it using regular earthquake source analysis (e.g. focal mechanism based on first motion polarities). If the source is different from that of a tectonic earthquake (e.g. geothermal/volcanic processes involving fluids), a shearing type focal mechanism would be inappropriate, but the first motion descriptions still valuable.

The waveforms of the Gvendarfell seismic events are strongly affected by path effects. In addition, the geometry of the network was unfavourable for source studies, with most stations located several km away from the source, mainly because of the glacier. Therefore, it was not considered promising to use a full waveform inversion to determine the source mechanism. Such a method is also very sensitive to erroneous velocity models, particularly at shallow depth (Bean et al., 2008), which strongly affects stations farther from the source. Therefore, an attempt to retrieve the focal mechanism was done based on the first motion polarities. The emergent P onset is difficult to identify for low-frequency events. Therefore, the signal-to-noise ratio was improved by aligning and stacking all the waveforms at each station (20 stations in total). This was possible thanks to the extreme similarity of the waveforms. Each waveform was weighted according to its signal-to-noise ratio and the uncertainty of the stack evaluated as variance of the weighted mean.

The first arrivals, however, remained unclear at many stations. A closer insight in the zoomed P waves, showed that the first wiggles of all waveforms are highly correlated between different stations. Therefore, by taking the clearest onset (positive polarity at the closest station GVE) as reference, we were able to interpret all the others. We did this by correlating the reference GVE onset with the stacked P onset at all other stations, first the original ones and then the reversed. The stations resulting in the best correlation for the original onset were assigned a positive polarity and vice-versa. The reason for this is intuitive and looks clear from Fig. 13, showing the resulting polarities and the beginning of the seismogram for all stations.

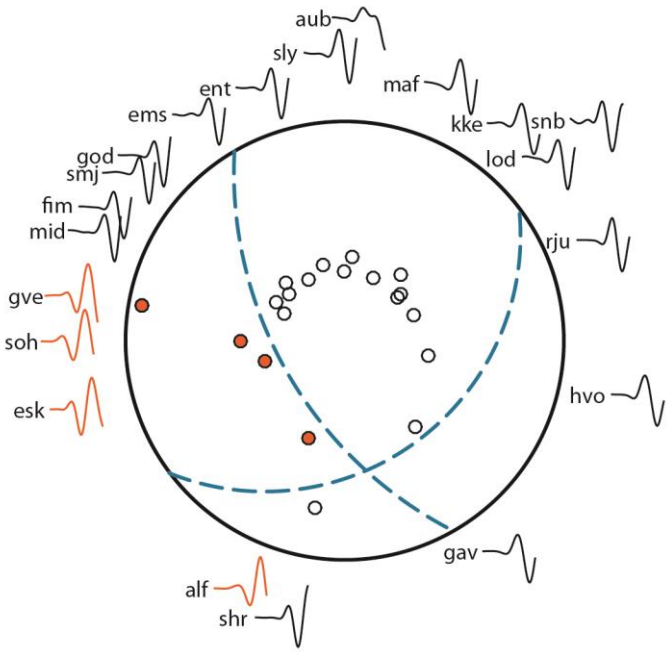

Fig 13. First motion polarities of the Gvendarfell events, for all seismic stations. Orange dots for positive polarities and white for negative. The beginning of the Z component seismogram for each station is also plotted, with colour corresponding to the polarity. A tentative fault plane solution consistent with normal faulting is drawn.

The interpretation of the first motions, however, is not trivial and no unique solution of the focal mechanism can be obtained. This arises mainly from the poor coverage of the focal sphere. Also, as the source is located in the shallow, low-velocity layers, take-off angles can vary considerably and strong scattering effects due to the heterogeneous medium are expected to affect azimuth angles. A tentative fault plane solution is drawn, consistent with normal faulting. This is however not well constrained and other mechanisms, with different combinations of CLVD (Compensated Linear Vector Dipole) and volumetric components might be invoked. Certainly, the polarities are not consistent neither with thrust faulting, nor with pure implosion/explosion.

9. Discussion

9.1 Event classification

The Gvendarfell seismic events have low frequency content, observed at all stations, from the closest (around 1 km) to the farthest (around 40 km). Path effects seem to be important at most stations, as seen from increasing complexity of the waveforms with distance from the source. Moreover, the presence of the glacier might also play a role as a filter for high frequencies (Weaver and Malone, 1979; Métaxian et al., 2003). If this was dominant, we would expect the same effect for the caldera events as well, where the glacier is much thicker, up to 700 m, compared to few tens of meters at Hafursárjökull above the Gvendarfell seismic source. However, we point out that other shallow events originating inside the Katla caldera contain a broader spectrum of frequencies, up to 10-15 Hz, with higher frequencies not completely attenuated by path effects. We therefore interpret the low frequency content of the Gvendarfell events as a source property and classify them as LP events. Moreover, other features of the waveforms are similar to those of LP events at other volcanoes: i) similarity of waveforms, ii) emergent onset of P wave, iii) unclear S wave, iv) narrow peaked spectra with typical frequencies between 0.5 and 5 Hz (Chouet, 2003).

9.2 Glacial vs volcano-related source

As the depth of the cluster is not distinguishable with certainty from the surface and the location corresponds to a glacier stream, glacial processes must be considered also as possible sources of the Gvendarfell seismicity. Glacial earthquakes can be associated with glacier sliding, e.g. stick-slip ice motion (Weaver & Malone, 1979; Ekström et al., 2006; Wiens et al, 2008; Thelen et al., 2013) or with ice avalanches and ice falls (Weaver & Malone, 1979; Caplan-Auerbach and Huggel C., 2007; Roux et al., 2008; Jónsdóttir et al., 2009). Resonance of

ice cracks (Métaxian et al., 2003) or resonance of the glacier (Wolf and Davies, 1986) can also generate LP events, but for the reasons discussed below, we consider resonance processes unlikely.

A glacial origin of these events could be in accordance with the seasonal variation observed, as it is usual for glacier seismicity to peak during warm seasons (e.g. Wolf and Davies, 1986; West et al., 2010; Moore et al., 2013). Glacier movements are enhanced due to summer melting, which in Iceland peaks in July and August, after the summer thaw. An example of regular and repetitive glacial seismicity over years has been observed in a Transantartic Mountains glacier (Winberry et al., 2015). The size (likely a few hundred meters) and slip-rate (50 m per year) of that glacier are however much bigger compared to Hafursárjökull glacier. Hafursárjökull is a small, stagnant alpine glacier, not more than few tens of meters thick, and is unlikely to be capable of producing such a persistent seismicity. Fig. 14 shows a picture of the glacier, highlighting its small size and showing its actual margin, compared to the outline drawn in Fig. 11. Alpine glaciers' seismicity is usually highly variable in amplitude, recurrence interval, waveforms and often shows changes on diurnal basis and correlation with precipitation rates (Thelen et al., 2013).

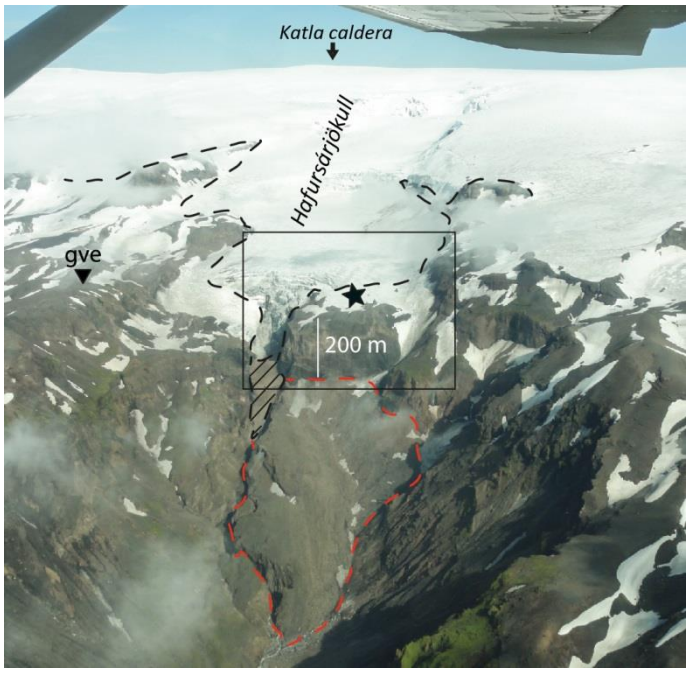

Fig. 14. Aerial view of Hafursárjökull glacier. The red dashed line is the glacier outline shown in Fig. 11. The black dashed line is the actual glacier limit as it is at the time we are writing (August 2015). The area marked with black lines is ice covered by debris. The star corresponds to the approximate location of the centre of the absolute hypocentre locations (obtained with the non-linear method, Fig. 12) and the box crudely indicates its uncertainty. The approximate location of the seismic station GVE is also drawn with a black triangle.

None of these characteristics are seen at Gvendarfell, where only one family of nearly identical seismic events has been observed for more than 3 years. In addition, if a relation existed between the Gvendarfell seismicity and glacial processes, it would be difficult to understand why similar events are not observed at more active glacier streams nearby or at other glaciers in Iceland. As a final consideration, the time association with the unrest episode in July 2011 seems easier to reconcile with volcanic or geothermal processes.

9.3 Interpretation of the source process

Due to their association with eruptions, it is commonly thought that LP events are caused by fluid movements within the volcano, for example magma injection into fractures or crypto-dome formation (Okada et al., 1981; Cruz and Chouet, 1997; Rowe et al. 2004; Neuberg et al., 2006), or processes related to hydrothermal systems (Moran et al., 2000; Saccorotti et al., 2007; Guðmundsson and Brandsdóttir, 2010; Jousset et al., 2010; Matoza and Chouet, 2010; Arciniega-Ceballos et al., 2012). The narrow-banded frequency range of LP seismograms at volcanoes is often associated with resonance processes in which the dominant frequency of the source is related to specific geometries and/or fluid characteristics.

In particular, monochromatic, volcanic LP events may be interpreted in terms of resonance of fluid-filled cracks (e.g. Chouet, 1996; Kumagai and Chouet, 1999; Saccorotti et al., 2007). However, a resonance process is expected to generate a long coda of decaying harmonic oscillations, which is not observed in the Gvendarfell events. While most stations record a long-duration signal, resembling resonance, the proximal observation from GVE station is short in duration and indicative of a source more pulse-like rather than resonating. This feature of LP events has been described by Bean et al. (2014) and explained as a strong path effect, very pronounced for shallow sources in the low-velocity, near-surface layers. They carried out a dynamic rupture simulation and showed that long-period signals can be generated by slow-rupture failure in unconsolidated volcanic materials. This indicates that LP events are not necessarily generated in association with fluid movements. Their simulations also show a spread of hypocentres, which seems to be not the case of the Gvendarfell seismicity, generated at a very small source, stable with time and always producing the same waveform. At Gvendarfell there is neither variability of waveforms, nor evidence for multiple structures acting as seismic sources, as described by Bean et al. (2014).

The high repeatability of waveforms and regular occurrence of LP events characteristic of the Gvendarfell seismicity have been observed at other volcanoes worldwide (Cruz and Chouet, 1997; Ramos et al., 1999; Green and Neuberg, 2006; Rowe et al. 2013), often associated with rising domes (e.g. Okada et al., 1981; Neuberg et al., 2006) or with the

interaction of hydrothermal and magmatic systems. For example, repetitive LP events at Popocatépetl were associated with the non-destructive process of repetitive injection of hydrothermal fluid into a fracture resulting in a sudden discharge when a critical pressure is reached (Arciniega-Ceballos et al., 2012). Matoza and Chouet (2010) interpreted repetitive LP events occurring at Mt. St. Helens with regular inter-event time spacing in terms of rapid heating of water and dissolved volatiles in a shallow hydrothermal crack, with events triggered by phase changes from liquid to vapour. In most cases, repeating LP seismicity has been observed either prior to or during eruptions, their repeatability lasts for days to months and the regular time intervals between successive events are on seconds to minutes scale. The Gvendarfell events, instead, did not precede or accompany an eruption (at least not in the same area), although they started in coincidence with a tremor event recorded inside the caldera. Moreover, the same waveforms have been recorded for around 3.5 years, occurring with regular inter-event times ranging from hours to days, depending on the season. These features make the Gvendarfell seismicity a unique case.

The Gvendarfell events are also different compared to the other LP events recorded at Katla, most of which are located at Goðabunga, on the western flank of the volcano. The other Katla LP events have a wider spectrum of frequencies, with higher frequencies in the beginning of the waveform decreasing towards the end, as opposed to the nearly monochromatic waveforms at Gvendarfell. In addition, no other cluster at Katla is composed of only one family of waveforms and no other cluster has a similar regular time pattern. The seasonal correlation also differs: the Goðabunga activity peaks later in autumn (Einarsson and Brandsdóttir, 2000; Jónsdóttir et al., 2009) as opposed to July/August at Gvendarfell and the caldera events have a less pronounced seasonality.

The non-monotonic size distribution is also peculiar and is reflected in the magnitude-cumulative number curve, where it is difficult to identify a unique b-value (Fig. 10). Earthquakes below $M_L = 1$ clearly dominate, implying that the source size is restricted and not capable of producing events larger than a threshold size. A similar case, with minor events occurring in the background of larger LP events, was observed at Mt. St. Helens during the 2004-2008 eruption period and interpreted in terms of less energetic fluid to gas phase changes, involving a smaller volume of fluid in a shallow hydrothermal crack (Matoza and Chouet, 2010). Non-linear magnitude-frequency relationship is commonly observed at volcanoes, e.g. the earthquakes accompanying the dyke injection at Krafla in September 1977 (Brandsdóttir and Einarsson, 1979).

Since we couldn't model the source mechanism, for the reasons discussed in section 8, we are not able to discuss in detail the physical process generating the Gvendarfell events. However, the striking time evolution, together with the repeatability of the waveforms over years, are

indicative of a remarkably stable, process repeating itself at regular time intervals, modulated by seasons, for an unusually long time. Although glacial processes cannot be completely ruled out, we regard volcano-related processes as more likely to generate such a stable seismicity.

Among volcanic processes, both magma-related (e.g. magma intrusion, dome formation) and non-magma related hydrothermal processes (e.g. fluid instabilities, thermal cracking) are candidate sources. The former interpretation fits with the geological evidence of silicic extrusive bodies at the caldera rim and on the eastern and southern flanks of Katla (Lacasse et al., 2007; Jóhannesson and Sæmundsson, 2009). This makes a rising shallow viscous magma body a plausible geological processes in the Gvendarfell area. A normal faulting mechanism with a dilatational component, consistent with the first motion polarities shown in Fig. 14, could fit with the hypothesis of an intruding dike. The time association with the tremor episode of the 2011 unrest would also fit with such magma-related interpretation. However, the GPS station operating during the summer of 2014 near the Gvendarfell area did not report evidence of ground deformation to support this hypothesis of a slowly intruding dyke. Moreover, the seasonal correlation of the seismicity appears difficult to reconcile with magma-related processes. Thus, we regard hydrothermal processes as more likely than magma movements to explain this seismicity. A minor hydrothermal system, lasting for about 3.5 years, might have been activated on Katla's south flank during the unrest episode in July 2011. The regular time pattern of the seismicity could be associated with a steady process of cyclic heating and cooling of the fluid phase in a hydrothermal crack system with LP events generated by phase changes between liquid and vapour (Matoza and Chouet, 2010). In this scenario, the seasonal correlation of the seismicity could be explained in terms of varying supply of ice melt water to the hydrothermal system, with peaks correlating with the warm seasons. Less energetic phase changes, involving smaller volumes of fluids, might explain the subset of smaller events. The first motion polarities, although not univocally interpretable, can be consistent with non-double-couple mechanisms observed at other geothermal areas such as Hengill in Iceland (e.g. Miller et al., 1998). However, we point out that there is no visible evidence of geothermal activity, new or old, in the area. The new hydrothermal system, therefore, has to be entirely concealed. Furthermore, a new hydrothermal system needs a new heat source. A small dyke injection into the southern caldera wall or changes to a permeable crack system in conjunction with the thermal event in July 2011 are possible scenarios. A summary of possible interpretations and corresponding pros and cons is reported in Table 1.

Process	Pros	Cons
GLACIAL e.g. glacier sliding, ice-falls	- seasonal correlation - shallow depth	- small, stagnant glacier - no correlation with precipitation rates - association with unrest episode - stability of the process over long time - depth (?)
VOLCANIC (magma involved) e.g. dome rising, viscous magma injection	- geological evidences: silicic extrusive bodies at the caldera rim and south/east flanks - association with unrest episode - normal faulting mechanism (?)	- seasonal correlation - no ground deformation detected
HYDROTHERMAL (no magma involved) e.g. phase changes of the geothermal fluid, thermal cracking	- shallow depth - high repeatability - association with unrest episode - seasonal correlation can be explained - regular time pattern can be explained	- no evidence of geothermal activity

Table 1. Summary of pros and cons of the three suggested interpretations of the source process of the Gvendarfell seismic events.

10. Conclusions

Since July 2011 the seismicity pattern at Katla volcano has shown changes: a new cluster of shallow, repeating LP seismic events has been observed on Katla's south flank, at the southern edge of Mýrdalsjökull glacier, 4 km south of the caldera rim. The onset of this seismicity coincided with an unrest episode culminated in a glacial flood from the south-east rim of the glacier, on July 9th, 2011. The seismicity on the south flank had never been observed before and continued for around 3.5 years with the same features.

Since these seismic events are located in a glaciated area, both volcanic and glacial processes must be taken into account as possible sources. Because of the characteristics of the small glacier stream and because of the remarkable stability of the main features of the seismicity over years, we regard volcano-related processes as more likely to generate this seismicity. However, we cannot rule out a glacial source and this study highlights the difficulty and the importance of discriminating glacial and volcanic sources at subglacial volcanoes.

Although they share some common features with LP earthquakes at other volcanoes worldwide, the seismic events we have described represent a peculiar case study because of

their temporal behaviour and because they did not accompany an eruption. We have not found a similar case in the literature. They also differ significantly from other Katla's LP events.

Among volcano-related process, we suggest a shallow hydrothermal system is more likely than magma movement to explain this seismicity, mainly because the clear seasonal correlation is easier to reconcile with a process involving water. The extremely regular time pattern over a long time (at least 3.5 years) together with the similarity of all the waveforms, point to a stable, non-destructive source mechanism over time. We regard the regular seismic rate, modulated by seasonality, as the most striking feature of this seismicity. Therefore, we look for a steady source process, in both location and mechanism, in which some critical parameter induces the regular time interval between events. This might be related to a steady process of heating and cooling of a fluid phase, in a geyser-like process. As the fluid phase is supplied by the glacier, a seasonal correlation can be expected as a response to the summer ice melting. Our hypothesis is therefore that a small, shallow hydrothermal system might have been activated on Katla's south flank, in coincidence with the 2011 unrest episode. As a power source, we suggest either a short lived dike intrusion towards the south flank or a crack connection to a heat source established during the unrest. However, no evidence of old or new hydrothermal activity has been seen in the area.

Further studies, such as relative relocation of the hypocentres and further insights into the tremor episode of July 2011, will help interpreting the source processes and volcanological implications of this peculiar cluster of LP events on the south flank of Katla.

Acknowledgements

The authors would like to thank the Icelandic Met Office for access to waveform data and catalogue data of the Gvendarfell events. The temporary deployments producing data for this study were supported by CNDS (Centre for Natural Disaster Science, www.cnds.se) at Uppsala University and the Volcano Anatomy project, financed by the Icelandic Science Foundation. This work was funded by the University of Bologna, University of Iceland and Uppsala University, as a part of a joint PhD project. We thank also the sheriff in Vík for logistic support and Vincent Drouin for the flight over the area.

References

Arciniega-Ceballos, A., Dawson, P., Chouet, B. a., 2012. Long period seismic source characterization at Popocatépetl volcano, Mexico. Geophys. Res. Lett. 39, 1–5. doi:10.1029/2012GL053494

Bean, C., Lokmer, I., O'Brien, G., 2008. Influence of near-surface volcanic structure on long-period seismic signals and on moment tensor inversions: Simulated examples from Mount Etna. J. Geophys. Res., 113, B08308. doi:10.1029/2007JB005468

Bean, C.J., De Barros, L., Lokmer, I., Metaxian, J.P., O'Brien, G., Murphy, S., 2014. Long-period seismicity in the shallow volcanic edifice formed from slow-rupture earthquakes. Nature Geoscience, 7 (1), 71-75.

Björnsson, H., Pálsson, F., Guðmundsson, M.T., 2000. Surface and bedrock topography of the Mýrdalsjökull ice cap, Iceland: The Katla caldera, eruption sites and routes of jökulhlaups. Jökull 49, 29-46.

Bransdóttir, B., Einarsson, P., 1979. Seismic activity associated with the September 1977 deflation of the Krafla central volcano in northeastern Iceland. J. Volcanol. Geotherm. Res. 6 (3), 197-212.

Budd, D.A., Troll., V.R., Dahren, B., Burchardt, S., 2014. Persistent shallow magma storage beneath Katla Volcano. Paper presented at: Goldschmidt Annual Meeting, Sacramento, USA.

Chouet, B.A., 1996. Long-period volcano seismicity: its source and use in eruption forecasting. Nature, 380, 309-316.

Chouet. B.A., 2003. Volcano Seismology. Pure appl. geophys. 160, 739-788.

Cruz, F.G., Chouet, B.A., 1997. Long-period events, the most characteristic seismicity accompanying the emplacement and extrusion of a lava dome in Galeras Volcano, Colombia, in 1991. J. Volcanol. Geotherm. Res., 77, 121-158.

Ekström, G., Nettles, M., Tsai, V. C., 2006. Seasonality and increasing frequency of Greenland glacial earthquakes. Science, 311, 1756– 1758.

Einarsson, P., 1991. Earthquakes and present-day tectonism in Iceland. Tectonophysics 189, 261–279.

Einarsson, P., Brandsdóttir, B., 2000. Earthquakes in the Mýrdalsjökull area, Iceland, 1978–1985: Seasonal correlation and relation to volcanoes. Jökull 49, 59–73.

Einarsson, P., Sæmundsson, K., 1987. Earthquake epicenters 1982-1985 and volcanic systems in Iceland. In Þ.I.Sigfússon, ed. *Í hlutarins eðli*, Festschrift for Þorbjörn Sigurgeirsson. Menningarsjóður, Reykjavík (map).

Green, D.N., Neuberg, J., 2006. Waveform classification of volcanic low-frequency earthquake swarms and its implication at Soufrière Hills Volcano, Montserrat. J. Volcanol. Geotherm. Res. 153, 51–63. doi:10.1007/1-4020-4287-6_4

Guðmundsson, Ó., Brandsdóttir, B., 2010. Geothermal noise at Ölkelduháls, SW Iceland. Jökull 60, 89-102.

Guðmundsson, Ó., Brandsdóttir, B., Menke, W., Sigvaldason, G.E., 1994. The crustal magma chamber of the Katla volcano in South Iceland revealed by 2-D seismic undershooting. Geophys. J. Int. 119, 277–296.

Guðmundsson, M.T., Högnadóttir, Þ., Kristinsson, A.B., Guðbjörnsson, S., 2007. Geothermal activity in the subglacial Katla caldera, Iceland, 1999–2005, studied with radar altimetry. Annals of Glaciology 45, 66–72.

Guðmundsson, M.T., Larsen, G., Sigmarsson, O., 2013. In: Sólnes, J., Sigmundsson, F., Bessason, B. (Eds.), Náttúruvá Á Íslándi. Eldgos og Jarðskjálftar. Viðlagatrygging Íslands/Háskólaútgáfan, p. 2013.

IMO, Icelandic Meteorological Office, 2011. http://en.vedur.is/.

Jakobsdóttir, S.S., 2008. Seismicity in Iceland: 1994–2007. Jökull 58, 75–100.

Jeddi, Z., Tryggvason, A., Guðmundsson, Ó., IMO-SIL monitoring group, 2015. 3D Velocity structure of the Katla volcano - Southern Iceland. Poster session presented at: 26th IUGG General Assembly 2015. Prague, Czech Republic.

Jóhannesson, T., Björnsson, H., Magnússon, E., Guðmundsson, S., Pálsson, F., Sigurðsson, O., Thorsteinsson, T., Berthier, E., 2013. Ice-volume changes, bias estimation of mass-balance measurements and changes in subglacial lakes derived by lidar mapping of the surface Icelandic glaciers, Ann. Glaciol., 54(63), 63–74. doi:10.3189/2013AoG63A422

Jóhannesson, H., Sæmundsson, K., 2009. Geological Map of Iceland. 1:600.000. Bedrock Geology, 1st edition. Icelandic Institute of Natural History, Reykjavík.

Jónsdóttir, K., Roberts, R., Phjola, V., Lund, B., Shomlai, Z. H., Tryggvason, A., Bodvarsson, R., 2009. Glacial long period seismic events at Katla volcano, Iceland. Geophys. Res. Lett. 36, L11402.

Jónsdóttir, K., Tryggvason, A., Roberts, R., Lund, B., Soosalu, H., Bodvarsson, R., 2007. Habits of a glacier covered volcano: seismicity and a structure study of the Katla volcano, South Iceland. Annals of Glaciology 45, 169–177.

Jónsson, G., Kristjánsson, L., 2000. Aeromagnetic measurements over Mýrdalsjökull and vicinity. Jökull 49, 47–58.

Jousset, P., Haberland, C., Bauer, K., Arnason, K., Weber, M., Fabriol, H., 2010. Seismic Tomography and Long-Period Earthquakes Observation and Modelling at the Hengill Geothermal Volcanic Complex , Iceland. Proc. World Geotherm. Congr. 2010 25–29.

Kumagai, H., Chouet, B.A., 1999. The complex frequencies of longperiod seismic events as probes of fluid composition beneath volcanoes. Geophys. J. Int. 138, F7–F12.

Lacasse, C., Sigurðsson, H., Carey, S.N., Jóhannesson, H., Thomas, L.E., Rogers, N.W., 2007. Bimodal volcanism at the Katla subglacial caldera, Iceland: Insight into the geochemistry and petrogenesis of rhyolitic magmas. Bulletin of Volcanology 69, 373–399.

Larsen, G., 2000. Holocene eruptions within the Katla volcanic system, south Iceland: characteristics and environmental impact. Jökull 49, 1–28.

Lindblom, E., Lund, B., Tryggvason, A., Uski, M., Bödvarsson, R., Juhlin, C., Roberts, R., 2015. Microearthquakes illuminate the deep structure of the endglacial Pärvie fault, northern Sweden. Geophys. J. Int., 201, 1704–1716.

Lomax, A., Virieux, J., Volant, P., Berge, C., 2000. Probabilistic earthquake location in 3D and layered models: Introduction of a Metropolis-Gibbs method and comparison with linear locations. In: Thurber, C.H., Rabinowitz, N. (eds.), Advances in Seismic Event Location, Kluwer, Amsterdam, 101-134.

Matoza, R. S., Chouet, B. A., 2010. Subevents of long-period seismicity: Implications for hydrothermal dynamics during the 2004–2008 eruption of Mount St. Helens. J. Geophys. Res., 115, B12206. doi:10.1029/2010JB007839

McNutt, S.R., 2005. Volcanic Seismology, Ann. Rev. Earth Planet. Sci. 33. doi: 10.1146/annurev.earth.33.092203.122459

Métaxian, J.-P., Araujo, S., Mora, M., Lesage P., 2003. Seismicity related to the glacier of Cotopaxi Volcano, Ecuador. Geophys. Res. Lett. 30(9), 1483. doi: 10.1029/2002GL016773

Miller, A.D., Foulger, G.R., Julian, B.R., 1998. Non double-couple earthquakes 2. Observations. Rev. Geophys. 36, 551-568.

Moore, P. L., Winberry, J. P. , Iverson, N. R., Christianson, K. A., Anandakrishnan, S., Jackson, M., Mathison, M. E., Cohen., D., 2013. Glacier slip and seismicity induced by surface melt. Geology, 41(12), 1247-1250.

Moran, S.C., Zimbelman, D.R., Malone, S.D., 2000. A model for the magmatic–hydrothermal system at Mount Rainier, Washington, from seismic and geochemical observations. Bull. Volcanol. 61, 425–436. doi:10.1007/PL00008909

Neuberg, J. W., Tuffen, H., Collier, L., Green, D., Powell, T., Dingwell, D., 2006. The trigger mechanism of low-frequency earthquakes on Montserrat. J. Volcanol. Geotherm. Res. 153, 37-50.

Okada, H., Watanabe, H., Yamashita, H., Yokoyama, I., 1981.Seismological significance of the 1977–1978 eruptions and the magma intrusion process of Usu volcano, Hokkaido. J. Volcanol. Geotherm. Res. 9, 311 –334.

Óladóttir, B.A., Sigmarsson, O., Larsen, G., Thordarson, T., 2008. Katla volcano, Iceland: Magma composition, dynamics and eruption frequency as recorded by Holocene tephra layers. Bull. Volcanol. 70, 475–493. doi:10.1007/s00445-007-0150-5

Ramos, E., Hamburger, M.W., Pavlis, G.L., Laguerta, E.P., 1999. The low-frequency earthquake swarms at Mount Pinatubo, Philippines: implication for magma dynamics. J. Volcanol. Geotherm. Res. 92, 295–320.

Roberts, M. J., Tweed, F. S., Russell, A. J., Knudsen, Ó., Harris, T. D., 2003. Hydrological and geomorphic effects of temporary ice-dammed lake formation during jökulhlaups. Earth Surf. Processes Landforms 28, 723– 737.

Roux, P. F., Marsan, D., Métaxian, J. P., O'Brien, G., Moreau, L., 2008. Microseismic activity within a serac zone in an alpine glacier. J. Glaciol., 54, 157– 168.

Rowe, C.A., Thurber, C.H., White, R.A., 2004. Dome growth behavior at Soufriere Hills Volcano, Montserrat, revealed by relocation of volcanic event swarms, 1995-1996. J. Volcanol. Geotherm. Res.134, 199-221.

Saccorotti, G., Petrosino, S., Bianco, F., Castellano, M., Galluzzo, D., La Rocca, M., Del Pezzo, E., Zaccarelli, L., Cusano, P., 2007. Seismicity associated with the 2004–2006 renewed ground uplift at Campi Flegrei caldera, Italy. Phys. Earth Planet. Inter. 165, 14–24. doi:10.1016/j. pepi.2007.07.006.

Sgattoni, G., Guðmundsson, Ó., Tryggvason, A., Lucchi, F., Einarsson, P., 2015. The 2011 unrest at Katla volcano: location and interpretation of the tremor source. Poster session presented at: 26th IUGG General Assembly 2015. Prague, Czech Republic.

Sigurðsson, O., Zóphoníasson, S., Ísleifsson, E., 2000. Jökulhlaup úr Sölheimajökli 18. júlí 1999 (The jökulhlaup from Sólheimajökull July 18, 1999, in Icelandic with English summary), Jökull 49, 75–80.

Soosalu, H., Jónsdóttir, K., Einarsson, P., 2006. Seismicity crisis at the Katla volcano, Iceland – signs of a cryptodome?. J. Volcanol. Geotherm. Res. 153, 177–186.

Spaans, K., Hreinsdóttir, S., Hooper, A., Ófeigsson, B.G., 2015. Crustal movements due to Iceland's shrinking ice caps mimic magma inflow signal at Katla volcano. Sci. Rep. 5, 10285. doi: 10.1038/srep10285

Sturkell, E., Einarsson, P., Sigmundsson, F., Geirsson, H., Ólafsson, H., Pedersen, R., de Zeeuw-van Dalfsen, E., Linde, A.T., Sacks, S.I., Stefánsson, R., 2006. Volcano geodesy and magma dynamics in Iceland. J. Volcanol. Geotherm. Res. 150, 14–34. doi:10.1016/j.jvolgeores.2005.07.010

Sturkell, E., Einarsson, P., Roberts, M.J., Geirsson, H., Guðmundsson, M.T., Sigmundsson, F., Pinel, V., Guðmundsson, G.B., Olafsson, H., Stefansson, R., 2008. Seismic and geodetic insights into magma accumulation at Katla subglacial volcano, Iceland: 1999 to 2005. J. Geophys. Res. 113, B03212.

Sturkell, E., Einarsson, P., Sigmundsson, F., Hooper, A., Ófeigsson, B. G., Geirsson, H., Ólafsson, H., 2010. Katla and Eyjafjallajökull Volcanoes. In: Schomacker, A., Krüger, J., Kjær, K.H. (Eds). The Mýrdalsjökull icecap, Iceland. Glacial processes, sediments and landforms on an active volcano. Developments in Quaternary Science 13. Elsevier, Amsterdam. ISBN 1571-0866, pp. 5–21.

Thelen, W. A., Allstadt, K., De Angelis, S., Malone, S. D., Moran, S. C., Vidale J., 2013. Shallow repeating seismic events under an alpine glacier at Mount Rainier, Washington, USA. J. Glaciol. 59, 214.

Thorarinsson, S., 1975. Katla og annall Kotlugosa. Arbok Ferdafelags Islands. Ferdafelag Íslands, Reykjavık, 125–149.

Thordarson, T., Miller, D.J., Larsen, G., Self, S., Sigurðsson, H., 2001. New estimates of sulfur degassing and atmospheric mass-loading by the 934 AD Eldgjá eruption, Iceland. J. Volcanol. Geotherm. Res. 108, 33–54.

Weaver, C. S., Malone, S. D., 1979. Seismic evidence for discrete glacier motion at the rock-ice interface. J. Glaciol. 23, 171– 184.

West, M.E., Larsen, C.F., Truffer, M., O'Neel, S., LeBlanc, L., 2010. Glacier microseismicity. Geology, 38(4), 319–322. doi:10.1130/G30606.1

Wiens, D. A., Anandakrishnan, S., Winberry, J.P., King, M.A., 2008. Simultaneous teleseismic and geodetic observations of the stick-slip motion of an Antarctic ice stream. Nature, 453, 770– 774.

Winberry, J.P., Conway, H., Huerta, A.D., Anandakrishnan, S., Aster, R.C., Koutnik, M., Nyblade, A., Wiens, D.A., 2015. Periodic, episodic, and complex behavior of glacial earthquakes. Paper presented at: 26th IUGG General Assembly 2015. Prague, Czech Republic.

4. PAPER 2

Relative relocation of earthquakes without a predefined velocity model: an example from a peculiar seismic cluster on Katla volcano's south-flank (Iceland)

Giulia Sgattoni[1,2,3*], Ólafur Guðmundsson[3], Páll Einarsson[2], Federico Lucchi[1]

[1] *Department of Biological, Geological and Environmental Sciences, University of Bologna, Bologna, Italy*

[2] *Institute of Earth Sciences, Science Institute, University of Iceland, Reykjavik, Iceland*

[3] *Department of Earth Sciences, Uppsala University, Uppsala, Sweden*

**Corresponding author:* giulia.sgattoni2@unibo.it

Submitted to *Geophysical Journal International*

Abstract

Relative relocation methods are commonly used to precisely relocate earthquake clusters consisting of similar waveforms. Repeating waveforms are often recorded at volcanoes, where, however, the crust structure is expected to contain strong heterogeneities and therefore the 1D velocity model assumption that is usually made in most location strategies is not likely to describe reality. A peculiar cluster of repeating low-frequency seismic events was recorded on the south flank of Katla volcano (Iceland) from July 2011. No seismicity had been reported in the same area before. As the hypocentres are located at the rim of the glacier, the seismicity may be due to volcanic or glacial processes. Information on the size and shape of the seismic cluster may help constraining the source process. The extreme similarity of waveforms points to a very small spatial distribution of hypocentres. In order to extract meaningful information about size and shape of the cluster, we minimize uncertainty by optimizing the cross-correlation measurements and relative-relocation process. With a synthetic test we determine the best parameters for differential-time measurements and estimate their uncertainties, specifically for each waveform. We design a relocation strategy to work without a predefined velocity model, by formulating and inverting the problem to seek for changes in both location and slowness. This approach allows to account for azimuth, take-off angles and velocity deviations from a 1D model. We solve the inversion explicitly in order to propagate data errors through the calculation. This approach allows to resolve a source volume few tens of meters wide on horizontal directions and around 100 meters in depth. There is no suggestion that the hypocentres lie on a fault plane and the depth distribution indicates that their source is unlikely to be related to glacial processes as the ice thickness is not expected to exceed few tens of meters in the area where the cluster is located.

Keywords: Katla volcano; Iceland; Relative relocation; slowness.

1. Introduction

Earthquake multiplets consist of very similar waveforms, often exceeding cross-correlation coefficients of 0.8 (Geller & Mueller 1980; Frémont & Malone 1987). They are common in tectonic and volcanic areas worldwide and they are likely to be caused by earthquakes occurring very close to each other and generated by similar, non-destructive, source processes (Geller & Mueller 1980). Because they consist of closely-spaced earthquakes, it is possible to determine relative relocation of the hypocentres with high accuracy (Poupinet *et al.* 1984; Fréchet 1985; Frémont & Malone 1987; Got *et al.* 1994; Slunga et al. 1995;

Waldhauser & Ellsworth 2000; Thelen *et al.* 2008). The relative relocation method is based on the idea that closely-spaced events recorded at a common station will share similar path effects and site effects. If the hypocentral separation between two events is small compared to the station-hypocentre distance and scale length of velocity heterogeneities, and if the latter is big compared to the dominant wavelength of the waveforms, then the ray paths to a common station are similar and the relative time lag between the two events will depend on their spatial offset in the direction of the station (Waldhauser & Ellsworth 2000; Wolfe 2002).

Moreover, the location precision is improved by using high-precision waveform cross-correlation methods to determine the relative time measurements. This can be done either in the frequency domain (Poupinet *et al.* 1984) or in the time domain (Deichmann & Garcia-Fernandez 1992). The accuracy of the arrival-time differences between pairs of similar events is reported to be on the order of 0.001 s for micro-earthquakes recorded by local networks (e.g. Frémont & Malone 1987). This makes it possible to calculate the relative location between hypocentres with uncertainty on the order of a few meters to tens of meters (Waldhauser & Ellsworth 2000).

This is particularly useful at volcanoes, where earthquakes are often characterized by unclear phase onsets and their arrival-time determination can be highly imprecise with manual phase-picking. The relative location of earthquake multiplets is, therefore, a common practice at volcanoes worldwide. Got *et al.* (1994) relocated 250 earthquakes beneath Kīlauea that defined a nearly horizontal plane of seismicity at 8-km depth. Rowe *et al.* (2004) relocated approximately 17,000 similar earthquakes on Soufrière Hills volcano, Montserrat. On Mount Pinatubo, Philippines, Thelen *et al.* (2008) relocated several multiplets associated with the 2004-2006 eruptive sequence at Mount St. Helens and suggested that they were related to pressurization of the conduit system.

Two techniques are commonly used for relative relocation of earthquakes. One is the master-event approach, where all other events are relocated with respect to one, the master event (Ito 1985; Scherbaum & Wendler 1986; Frémont & Malone 1987; Van Decar & Crosson 1990; Deichmann & Garcia-Fernandez 1992; Lees 1998). Alternatively, cross-correlation time delays can be computed for all possible event pairs and combined in a system of linear equations to determine hypocentroid separations (Got *et al.* 1994; Waldhauser & Ellsworth 2000). In addition to adding more constraints to the model parameters, this strategy makes it possible to increase the spatial extent of the cluster that can be relocated, as there is no need for all events to correlate with the master.

The ability of the relative-relocation technique to recover the relative locations well depends on i) the geometry of the network, ii) the accuracy of differential-time measurements,

iii) the deviations from the assumption that the ray paths do not change within the cluster of events, iv) the direction of the rays leaving the source, depending on 3D velocity variations (Slunga *et al.* 1995; Michielini & Lomax 2004). The relative relocation problem is usually solved in a 1D velocity model (e.g. Waldhauser & Ellsworth 2000) or with a constant slowness vector for each station to the cluster (Got *et al.* 1994). However, in these approaches the source of error represented by the uncertainties in the ray directions in the source volume is not taken into account. Michielini & Lomax (2004) showed how the initial 1D velocity model used, determining the take-off angles, influences the resulting shape of the relocated cluster. Moreover, in highly heterogeneous media, such as in volcanic areas, strong lateral heterogeneities can cause considerable deviations in the direction of the seismic rays from the straight path assumed in a 1D velocity model. This, in turn, can affect the spatial direction in which the earthquake location is re-adjusted as constrained by each station's differential time.

We propose a relative relocation strategy that does not rely on a 1D velocity model, but rather seeks changes in slowness vectors together with changes in relative relocation of hypocenters. We apply the relative-relocation technique to a cluster of LP (Long Period, Chouet 2003) seismic events located on the south flank of the subglacial volcano Katla, in south Iceland. This seismicity started in July 2011, in association with an unrest event which culminated in a glacial flood. Seismic events in this part of Katla volcano had never been recorded before. Since they occurred in a glaciated area, they can be generated by either glacial or volcanic processes. Sgattoni *et al.* (2015) suggested that they are associated with hydrothermal processes. A closer insight into the relative relocation of the hypocentres can give a useful contribution to the source interpretation.

The extreme similarity of the waveforms indicates a very small spatial distribution of the hypocenters. Moreover, indications of strong path effects, together with the poorly known velocity model for the site, motivated the development of a specific strategy to optimize both the differential-time measurements and the relative relocation technique. We conduct both cross-correlation measurements and relative-relocation inversion so that the uncertainty is carefully estimated and the sources of error minimized in each step. We perform a statistical test to evaluate the best cross-correlation parameters and uncertainties of differential-time measurements specifically for each station and each seismic phase used. This alleviates the need to use generalized statistical assumptions about errors. We then relocate the events with a master-event relocation strategy, inverting for both changes in location and in slowness, in order to account for azimuth, take-off angles and velocity deviations from a 1D model. We solve the inversion explicitly in order to propagate data errors through the calculation. We

also perform synthetic tests to evaluate the ability of this approach to recover relative locations and slowness-vector components.

2. Seismic data

2.1 Seismic network

Following the eruptions of the neighbouring Eyjafjallajökull volcano in 2010, the IMO augmented the seismic monitoring network around Katla from 5 to 9 stations. Moreover, 9 temporary stations were deployed by Uppsala University between July 2011 and August 2013.

Most of the stations were equipped with broadband sensors, 5 Guralp ESPA , 4 Guralp CMG3-ESPC and 1 Geotech KS-2000(LLC), all with flat response from 60 s to the Nyquist frequency (50 Hz). 5-second Lennartz populated the remaining 8 stations. Data were recorded and digitized with Guralp and Reftek systems at 100 sps. Stations were powered with batteries, wind generators and solar panels. All the instruments recorded in continuous mode, but some technical problems (e.g. power failure) mainly due to harsh weather conditions (especially in winter time), prevented some stations from working continuously during the whole operation time.

Because the seismic events we analyse are very small (magnitude lower than 1.2; Sgattoni *et al.* 2015), the signal to noise ratio (snr) is low at distant stations. Therefore, we used data from 13 out of 19 stations (Fig. 1).

2.2 LP seismic events, Katla south flank

The LP events recorded near Gvendarfell on Katla's south flank have been described in detail by Sgattoni *et al.* (2015). We report here the main features. The seismicity is shallow and located on the southern side of Mýrdalsjökull glacier. It is characterized by small magnitude (~ -0.5-1.2 M_L), long-period earthquakes with an emergent P wave and an unclear S wave (Fig. 2). The frequency content is narrow banded around 3 Hz at most stations (Fig. 2). All events have remarkably similar, nearly identical waveforms with correlation coefficient ≥ 0.9 at the nearest stations, throughout the whole time period investigated (March 2011 – August 2014). The size distribution is non-monotonic, with small events below magnitude M_L = 0.2 and bigger events up to M_L = 1.2.

The signals are characterized by a number of distinct seismic phases, whose nature is difficult to understand, as the waveforms are heavily contaminated by secondary phases generated by strong path effects. It is in general possible to recognise a P phase and a

secondary wave package whose interpretation is not clear, probably containing both S waves and surface waves. Although unclear, we will refer to it as S wave (Fig. 2).

Around 1800 events have been detected with cross-correlation of a sample waveform with continuous data between July 2011 and August 2013. The temporal evolution shows striking features: a regular time pattern with 6 events per day at 4 hour intervals began a few hours before the tremor burst of the 2011 unrest episode, which occurred on July 8th-9th. A seasonal variation in the event rate is also observed, with maximal activity in late summer 2011, 2012 and 2013.

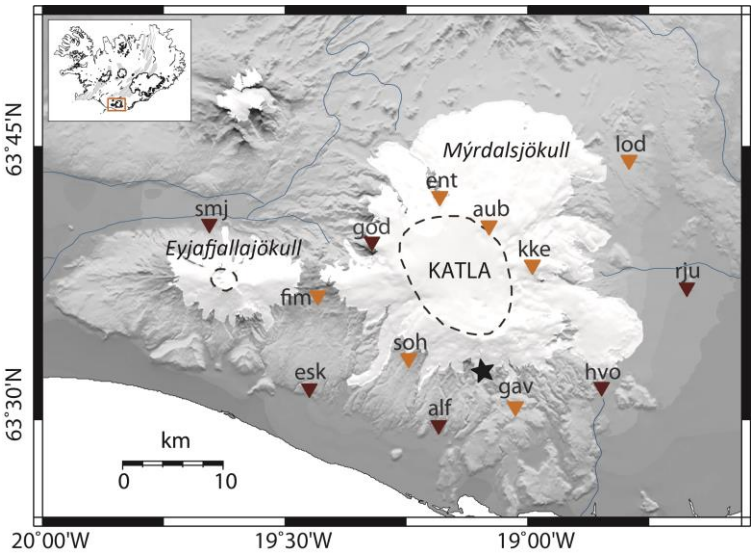

Fig. 1. Map of Mýrdalsjökull and Eyjafjallajökull showing the seismic network used in this study. Dark brown triangles: permanent IMO seismic stations. Orange triangles: temporary Uppsala University seismic stations operating between July 2011-August 2013. The star marks the new Gvendarfell cluster on the south flank. The Katla and Eyjafjallajökull caldera rims are outlined by dashed lines. White areas are glaciers.

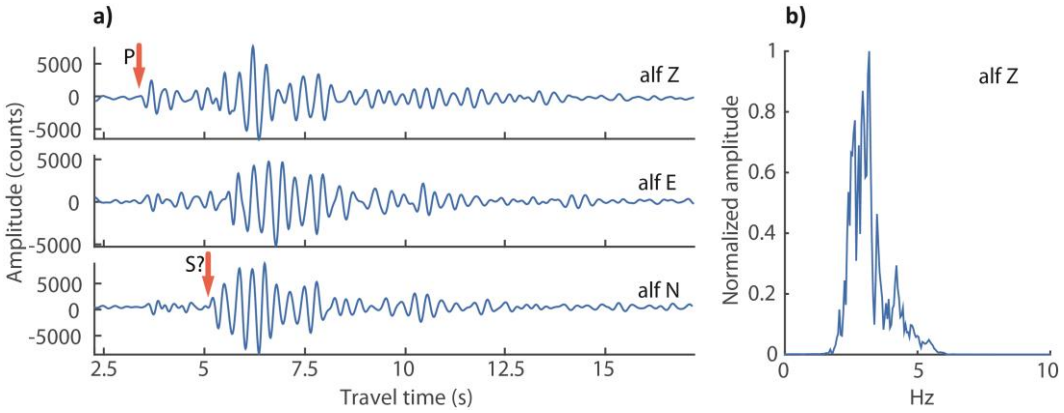

Fig. 2. a) Example seismograms of a Gvendarfell event at stations ALF. The amplitude unit is digital counts, proportional to velocity. b) Normalised amplitude spectra of the Z component of the same event at stations ALF.

3. Differential time measurements

As all the waveforms are extremely well correlated, with cross-correlation coefficients higher than 0.9 (mostly ≥ 0.95; Fig. 4), at the nearest stations, we expect a very small spatial distribution of the hypocentres. We can crudely estimate the maximum size of the source distribution requiring a phase difference of less than a fraction of a period in order to achieve such high levels of correlation. Taking this fraction to be a quarter and assuming an average velocity of 3.5 km/s and a dominant frequency of 3.5 Hz, we constrain the source region to be smaller than 250 m in size. Therefore, in all steps leading to the relative relocation results, we attempt to minimize the uncertainty and also carefully estimate it, from the differential-time measurements to the resulting relative locations. In order to measure the relative times as accurately as possible, we set up a synthetic test to identify the best parameters to use for the cross-correlation. We then use the synthetic test to evaluate their uncertainty, later used as weights for the relative relocation inversion.

3.1. Statistical test for cross-correlation

We perform a synthetic test that measures the time shifts between a clean waveform (the template waveform) and the same waveform with different levels of random noise added. The random noise is generated as white noise and then filtered with the same filter as the template and adjusted in amplitude to constitute the specific snr, which is defined as the ratio between the rms signal amplitude in the correlation time-window and rms noise amplitude in a window of equal length before the P arrival.

At each station and for each component of the signal:

- P and S phases are identified and extracted from the template waveform, previously band-pass filtered between 2-4, 1-5 or 2-5 Hz depending on the station (the S phase is identified only at stations ALF, GAV, SOH, HVO, ESK, FIM and RJU).
- The extracted P/S window is tapered with a 10% cosine taper.
- A template P/S window is correlated in the time domain with the same window with noise added (without applying any time shift so that the differential time is known to be exactly zero). A parabolic interpolation around the peak of the correlation function is done to estimate the time shift with sub-sample precision.

The test is repeated for different snr (signal to noise ratios), varying from 1 to 10, and different widths of the P and S windows, from 0.5 s to a few seconds.

The whole process is performed at least 100 times, each time generating a new random noise vector (Fig.3). The std (standard deviation) of the calculated time shifts is then computed

and its behaviour is analysed to determine, for each station, i) the best window width to use for each type of wave and component at each station, ii) the expected std as a function of the correlation coefficient. The first is done as follows:

- The correlation coefficients obtained for different snr and window widths are plotted against the window width used, always starting at the P arrival time at a given station.
- Two peaks are identified in this plot. One peak occurs before the S arrival and represents the best window length for the P wave. The other peak occurs after the S arrival and corresponds to the sum of P and S windows that have best correlation. The best window width for the S wave, therefore, corresponds to the time of the second peak minus the S-P time at a given station.

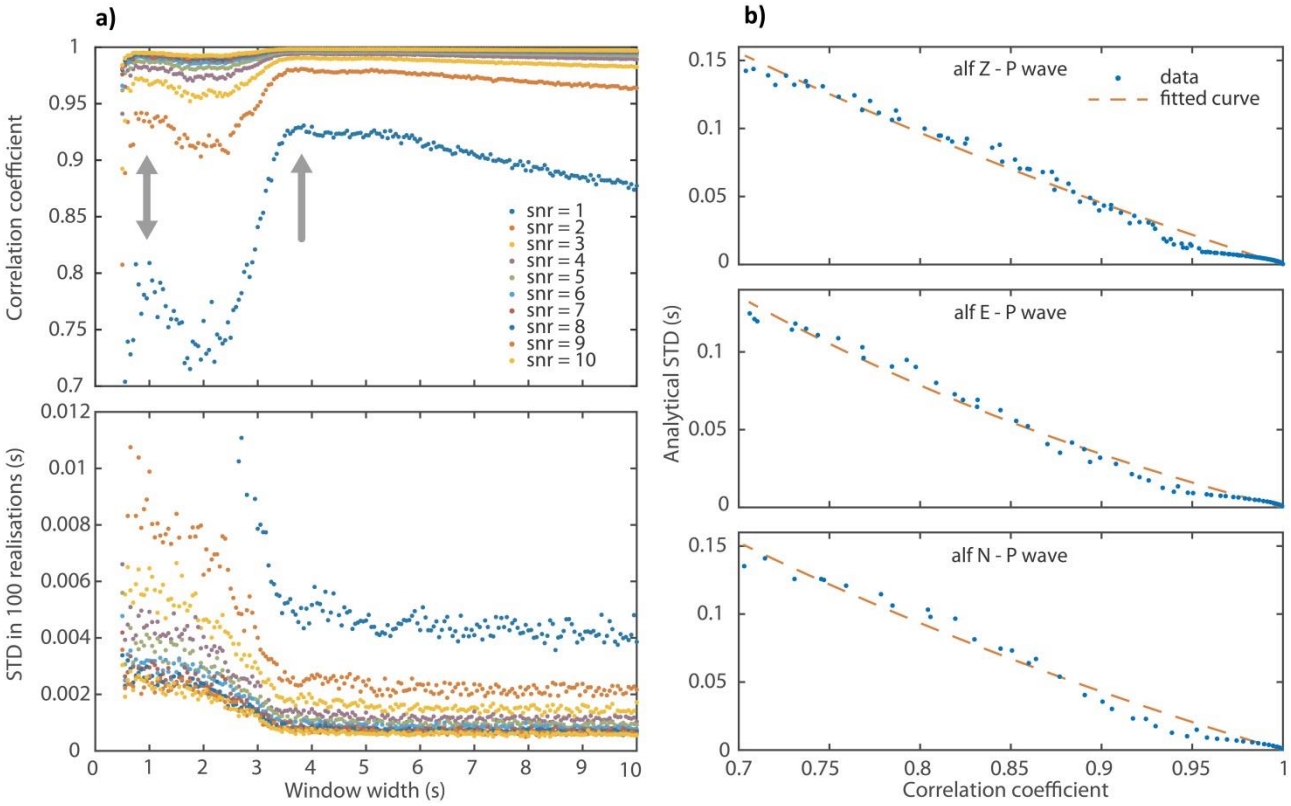

Fig. 3. Statistical simulation to determine uncertainty of cross-correlation measurements. Data from station ALF. a) correlation coefficient and std obtained for different widths of the window used for correlation and different values of snr. Window widths are measured starting from P arrival time. A first peak is observed at around 1 sec (double arrow): this is the width chosen for P wave. At station ALF the S-P time is 1.6 s and this determined increase in correlation after this time and reaching a new peak at ~4 seconds (single arrow). The window width chosen for S wave is therefore 2.4 s (corresponding to 4 s minus 1.6 s). As expected, uncertainty decreases with increasing snr. b) analytical standard deviation as a function of correlation coefficient, measured for chosen window width (1 sec) and varying snr. Results for 3 components of P wave at ALF. An empirical fitted curve is then used to estimate uncertainty of differential-time measurements between the template event and all the others.

Fig. 3 shows an example for station ALF: a first peak of correlation is observed at 1 sec and this is, therefore, the width chosen for the P wave. At this station the S phase arrives 1.6 seconds after the P phase and this is reflected by an increase in correlation coefficient starting after this time and reaching a new peak around 4 seconds. Therefore, the window width chosen for the S wave is 2.4 seconds.

The analytical std as a function of the correlation coefficient is then estimated for the chosen window length (Fig.3):

- The standard deviation obtained for different snr and window lengths is plotted as a function of correlation coefficient.
- An empirical curve is fitted to the data and later used to estimate the uncertainty of the differential-time measurements of the real data, based on the correlation coefficient.

The same procedure is repeated for P and S phases and all components. The uncertainty of the differential time estimates is in most cases lower than the sampling interval (0.01 s) and as low as 1 ms (Fig.4).

This synthetic test allows for optimization of the differential-time measurements in order to minimize uncertainty. It also allows us to estimate uncertainty specifically for each waveform, thus avoiding further generalized statistical assumptions about errors.

3.2. Cross-correlation measurements

Once the best parameters for the time-difference estimation are determined, a cross-correlation scheme is built to correlate a reference event (later used as master event for the relative relocation) with all other events (P and S phases separately), at all stations, for all components. Sub-sample estimates of time lags are achieved in the time domain through polynomial interpolation of the cross-correlation coefficient peak. Since not all stations have been working at the same time for the entire period of study, it is not possible to identify one unique reference event. An event which occurred on Oct. 10th 2011 is chosen for stations ALF, GAV, KKE, HVO, AUB, ENT, RJU, ESK, FIM, SLY, SMJ. An event on Feb 18th 2013 is chosen for SOH and on Oct 1st 2011 for LOD.

For each station, the differential-arrival times and the corresponding uncertainties are estimated for P and S waves for all 3 components. Moreover, for each phase (P and S) the weighted average of the time shifts for the different components by their uncertainty is computed. Ultimately, the best estimates (in terms of low error) are selected between the 4 values obtained (3 components and weighted average) and the uncertainty used to weight the data in the relative-relocation inversion.

The cross-correlation times are selected by setting a lower threshold for the cross-correlation coefficient as high as 0.9 for the closest stations and 0.8 for more distant stations and only event pairs with at least 6 time measurements are used (Fig. 4). We also discard some outlying data, with uncertainty greater than 0.03 s. This reduces the number of relocated events to 1140. This is mainly due to the small magnitude of the events, in particular the smaller-magnitude group, which is only observed at a few nearby stations. From around August 2012 a decrease in average magnitude from ~1 M_L to ~0.5 M_L is also observed for the larger-magnitude group of events (Sgattoni *et al.* 2015). There is a greater loss of data in the second part of the dataset, after January 2012, when a slight decrease of correlation coefficient occurs and some data are lost due to technical problems at some seismic stations (Fig. 4). The decreased correlation coefficient causes increased uncertainty of differential-time measurements (Fig. 4), which starts in January 2012, increases until August 2012 and remains fairly stable after that. This pattern does not clearly correlate with changes in the seismic network configuration.

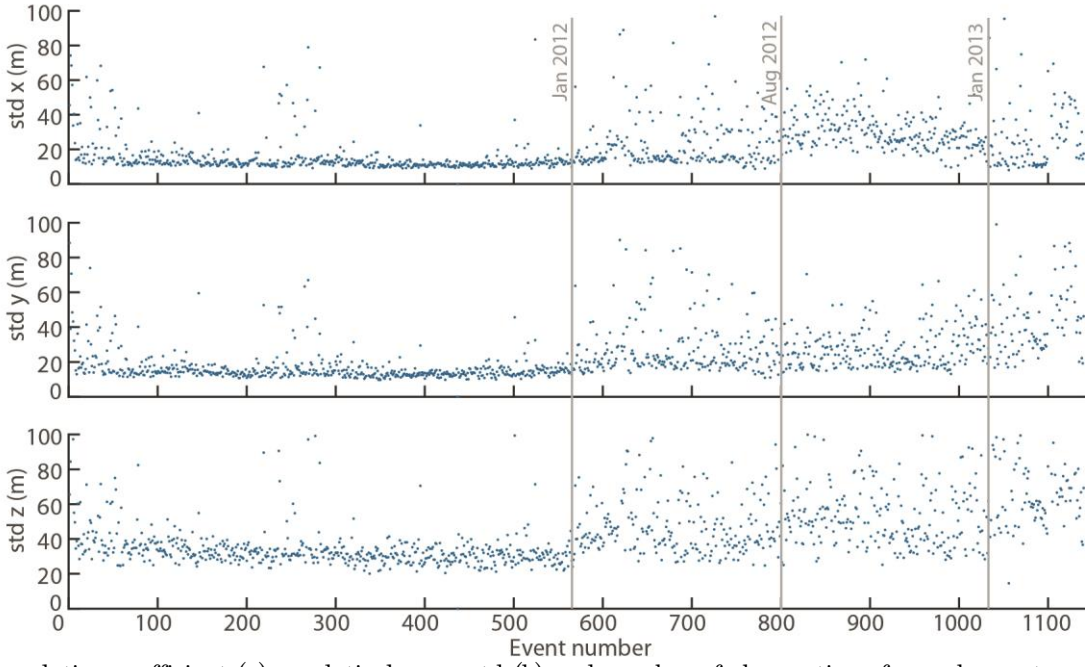

Fig. 4. Correlation coefficient (a), analytical error std (b) and number of observations for each event used in the relative relocation (c).

4. Relative-relocation method

As no catalogue locations exist for all 1200 events, a master event strategy is used to relocate the events starting from the same initial location and relocating them with respect to the fixed location of a master event (Ito 1985; Scherbaum & Wendler 1986; Frémont & Malone 1987; Van Decar & Crosson 1990; Deichmann & Garcia-Fernandez 1992; Lees 1998). An

event which occurred on October 10th 2011, used as reference for cross-correlation time measurements at most of the stations, is chosen as a master event. As location coordinates, we use the highest-probability hypocentral coordinates from the combined probability density of non-linear absolute locations obtained by Sgattoni *et al.* (2015), at N63º32.772' and W19º05.988' and depth is referred to the average elevation in the source region (at 800 m.a.s.l.). Since a different reference event was used for cross-correlation measurements at stations SOH and LOD, we made sure that the three reference events used had at least 8 differential time information linking them.

In the first instance, the routine is built to relocate the events in a 1D velocity model, similar to most relative-relocation strategies (e.g. Slunga *et al.* 1995; Waldhauser & Ellsworth 2000). However, the data misfit achieved is not satisfactory, as the data are not explained by the model locations close enough to their level of uncertainty (known from the synthetic test explained above). The misfit, normalized by the data covariance, exceeds the expectation of the chi-squared distribution by a factor of 5.

We think this is partially due to effects of lateral heterogeneities that are expected to be strong in the crust in the area and may cause considerable deviations in the direction of the seismic rays from the straight path assumed in a 1D velocity model. Since this direction can vary considerably because of the local heterogeneities, this introduces inconsistencies that cannot be explained by the model. In addition, the correlation-time measurements are integrated measurements of wave packages extending over 0.5 to several seconds. They are likely to contain waves of varying type and geometry due to scattering. This is confirmed by their complex particle motion. Therefore, the effective slowness of these waves as they leave their source may differ from that predicted by a simple 1D model, in terms of azimuth, incidence angle and effective local velocity. Thus, the strategy is adjusted to account for this and the slowness vectors (3 spatial components per station per wave type) are included as model parameters in the inversion. Azimuths, incident angles and P/S velocity are allowed to be modified by the inversion, in order to account for velocity heterogeneities.

4.1. Formulation of the problem

At a given station, the arrival time, *t,* for an earthquake, *i*, corresponds to the sum of the origin time, τ, and the travel time, *T,* as a function of the event spatial coordinates, $\boldsymbol{x}_i$:

$$t_i = \tau_i + T(\boldsymbol{x}_i) \quad (1)$$

We assume the locations are around a point, $\boldsymbol{x}_0$, with only small changes, $\delta\boldsymbol{x}_i$, much smaller than the propagation distance:

$$\boldsymbol{x}_i = \boldsymbol{x}_0 + \delta\boldsymbol{x}_i \qquad |\delta\boldsymbol{x}_i| \ll propagation\ distance \tag{2}$$

If the distances between the events are much smaller than the propagation distance from source to receiver, then the differences in path from the events to the same station can be described as planar. In our example, the distances between source and receiver are in the range of 6-30 km and the events are likely to be generated at distances from the centre of the cloud on the order of ≤ 100-150 meters, as apparent from the non-linear absolute locations presented by Sgattoni *et al.* (2015) and from the extremely similar waveforms. The events are so close to each other that a first order, linear or planar approximation of the travel-time function is justified. Therefore, we can apply a linear approximation:

$$T(\boldsymbol{x}_i) = T(\boldsymbol{x}_0 + \delta\boldsymbol{x}_i) \approx T(\boldsymbol{x}_0) + \boldsymbol{u}\cdot\delta\boldsymbol{x}_i \tag{3}$$

where $\boldsymbol{u}$ are linear coefficients with the unit of slowness (sec/km). Consequently, the differential arrival-time, δt, between events i and j at a given station, can be expressed as:

$$\delta t_{ij} = t_i - t_j = \tau_i - \tau_j + \boldsymbol{u}(\delta\boldsymbol{x}_i - \delta\boldsymbol{x}_j) \tag{4}$$

This is similar to the formulation by Got *et al.* (1994) who used a constant slowness vector for each station to the cluster. Instead, we allow the slowness vector to each station to vary in the inversion. Equation (4) is non-linear in the last term when both $\boldsymbol{u}$ and $\delta\boldsymbol{x}_i$ are unknown and the model parameters are coupled, as they appear as a product. So, we linearize again by differentiating with respect to slowness and location parameters, to seek changes in both slowness and location:

$$\delta t_{ij} \approx \tau_i|_0 - \tau_j\big|_0 + d\tau_i - d\tau_j + \boldsymbol{u}_0(\delta\boldsymbol{x}_i - \delta\boldsymbol{x}_j) + \boldsymbol{u}_0(d\delta\boldsymbol{x}_i - d\delta\boldsymbol{x}_j) + d\boldsymbol{u}(\delta\boldsymbol{x}_i - \delta\boldsymbol{x}_j)\big|_0 \tag{5}$$

where the 0 subscript indicates the initial guess (or estimate at previous iteration) and d indicates the change of the model parameter. In each iteration we solve for perturbation of location parameters (spatial and origin time) and perturbation of the slowness vector, thus obtaining an update of location and slowness. We also apply constraints to the slowness vector within reasonable bounds in order to avoid absurd geometry configurations such as rays leaving the source in opposite direction with respect to the station location.

The initial slowness vector $\mathbf{u}$ is determined from azimuth angles, α, and incidence angles, φ, for each station j, (estimated in a 1D velocity model) and constant initial velocities, v, for P/ S waves:

$$\boldsymbol{u_j} = \left(-sin\alpha_j\, sin\varphi_j \frac{1}{v};\ -cos\alpha_j\, sin\varphi_j \frac{1}{v};\ -cos\varphi_j \frac{1}{v}\right) \tag{6}$$

The initial P velocity is set as the P velocity at the master event hypocentral depth, corresponding to 3.5 km/s. The S velocity is set as the P velocity scaled by a factor of $1/\sqrt{3}$. In total, the slowness parameters are six per station (3 for P and 3 for S). We do not constrain the

angles to be the same for P and S, as there can be different scattering phenomena with different influence on P and S azimuth and incidence angles.

4.2. Inversion

As we do not have catalogue locations for all events, before inverting for relative relocations, we need an estimate of origin times. So, we first formulate the problem in order to invert for origin time. This is a linear problem in which the differential arrival times correspond to the sum of the differential origin times and differential travel times:

$$\delta t_{ij} = \tau_i - \tau_j + T(\boldsymbol{x}_i)|_0 - T(\boldsymbol{x}_j)\big|_0 \quad (7)$$

We solve the problem by assuming that all events are located at the master event location (i.e. all relative locations equal to zero). Therefore, the travel times for all events are the same and equation (7) simplifies to a difference of origin times.

We combine all data in a system of linear equations of the form:

We combine all data in a system of linear equations of the form:

$$\boldsymbol{WGm} = \boldsymbol{Wd} \quad (8)$$

where $\boldsymbol{G}$ is a matrix of size N x Nev (N is the number of differential-time measurements; Nev is the number of events), $\mathbf{m}$ is the model vector of length Nev, containing origin times, $\mathbf{d}$ is the data vector of length N, and $\boldsymbol{W}$ is a diagonal matrix containing weights.

We then add hard constraints in the form of Lagrange multipliers in order to fix the master event origin time to a reference time (that we set to 0). The problem is overdetermined and can be solved in a weighted least-squares sense, where the weights are set as the inverse of the data covariances:

$$\boldsymbol{m} = \left[\boldsymbol{G}^T \boldsymbol{C}_d^{-1} \boldsymbol{G}\right]^{-1} \boldsymbol{G}^T \boldsymbol{C}_d^{-1} \boldsymbol{d} \quad (9)$$

where $\boldsymbol{C}_d$ is the data covariance matrix, a diagonal matrix containing data variances determined by the synthetic tests described in the previous section. In order to determine the inverse of the product matrix $[\boldsymbol{G}^T \boldsymbol{C}_d^{-1} \boldsymbol{G}]$, we use the singular-value decomposition (SVD) method. The system is well-conditioned and there is no need to regularize.

After solving for the origin time, an iterative process is set up to invert equation (5) alternatively for relative changes in location, $(d\delta \boldsymbol{x}_i - d\delta \boldsymbol{x}_j)$, and changes in slowness, $d\boldsymbol{u}$. The inversion strategy is the same as before, but the size of the matrices and the hard constraints change. In the inversion for location parameters, the model vector $\mathbf{m}$ has length 4Nev ($d\delta x_1$, $d\delta x_2, d\delta x_3, d\tau$) and the size of $\boldsymbol{G}$ is N x 4Nev. The Lagrange multipliers consist in this case of four additional equations to constrain all changes of hypocentral parameters of the master event to be zero. Also in this case, the system is well-conditioned as we pre-filtered the data so

that all event pairs have at least 6 observations. This way all events are well linked to each other.

When inverting for slowness perturbations, the size of the matrices decreases significantly as the number of model parameters reduces to the size of the slowness vector, i.e. 6 times the number of stations (Nst), and $\boldsymbol{G}$ is therefore N x 6Nst. Again, the inversion strategy is the same and the matrix is inverted with SVD. In this case, some regularization is needed to exclude the zero eigenvalues originating from stations that have no information for some slowness components, depending on which phases have been used for the cross-correlation. Also, some small eigenvalues can occur if only little information is used for some stations and if, due to the geometry of the problem, some directions are poorly constrained. A threshold value for eigenvalues is found by trial and error.

After the inversion is performed, the resulting perturbations of slowness are checked in order to apply constraints to incidence angle, azimuth and velocity variations, so that they do not exceed specified values. P and S wave velocities are allowed to vary within ± 1 km/s from the initial values. The azimuth angles can change within ± 30 degrees from the initial direction and the incidence angles within ± 20 degrees.

The inversion scheme is therefore the following:

- Iteration 0: inversion for origin time and inversion for location parameters (using the initial slowness vector)
- Iteration 1…n: inversion for slowness and inversion for location parameters (using updated slowness vector).

The process is iterated until the misfit reduction is negligible, for a total of 7 iterations.

4.3. Model covariance estimation

The uncertainty of the location model parameters is then determined by propagating the estimated data covariances to the model parameters. However, this is sufficient only if the data are appropriately explained (within their uncertainty). In our case study this does not happen, as the final misfit achieved is bigger than the value expected statistically. If data are appropriately explained, the data misfit scaled by data covariance, Q, is expected to equal the number of degrees of freedom of the model, if the model errors are Gaussian:

$$\mathrm{E}\{Q\} = \boldsymbol{e}^T \boldsymbol{C}_d^{-1} \boldsymbol{e} = n - r \tag{10}$$

where $\mathrm{E}\{Q\}$ is the expectation of Q, $\boldsymbol{e}$ is the prediction error, n is the number of observations and r is the number of eigenvalues used in the inversion (the degrees of freedom in the model). In our case the misfit is bigger than $(n - r)$. This means that errors in the problem are not fully described by measurement errors. Additional errors occur, possibly due to simplification

of the theory or limited knowledge about the velocity model. We account for this by adding a uniform diagonal covariance to our estimated data covariance matrix, so that the expected misfit indicates that data are appropriately explained. We do this by calculating Q as a function of data variance, σ_d^2, with a constant, c, added to the diagonal elements:

$$\hat{Q} = \boldsymbol{e}^T(\boldsymbol{C}_d^{-1} + c\boldsymbol{I})^{-1}\boldsymbol{e} \tag{11}$$

where $\boldsymbol{I}$ is the identity matrix. We solve $\hat{Q} = n - r$ for c. We therefore obtain a new data-covariance matrix, which includes both measurement errors and errors due to simplifications of the way the forward problem is described and solved. We use this as a new estimate of the total data covariance and propagate it through the calculation, to estimate the model covariance, i.e. the uncertainty of relative relocation.

This strategy of adding a random component to the data variance estimates of measurement errors assumes that the errors in the data are independent of errors due to the simplification of the forward problem. Another possible strategy would be to scale the errors up according to the residual misfit, but we have no reason to expect that the unaccounted for errors are correlated with and proportional to the analytical measurement errors.

The resulting uncertainty of spatial location parameters is on the order of 15-20 meters for the horizontal components and 30-40 meters for the vertical. A general increase in uncertainty is observed from January 2012, correlating with bigger data uncertainties (see Section 3.1) and associated with less phases available per event-pair, as explained in Section 3.2.

5. Synthetic tests

In order to test the behaviour of the inversion and the ability of the program to recover both hypocentre locations and slowness components, we performed several synthetic tests with the station configuration and geometry of the problem of our case study on the south flank of Katla. Using equation (4), we generate differential times for all event pairs of a set of 50 events with random hypocentral locations within a 300x300x300 m volume. The data are generated using an initial slowness vector for the same 1D model that was used to construct the slowness for the inversion of real data (Section 4.1).

We generate perfect data and a slowness vector perturbed with random Gaussian errors. We track, iteration by iteration, the slowness vector std with respect to the true slowness and the spatial and temporal mislocations of the hypocentres. We repeat the test at least 100 times and compute an ensamble average of the results for all realizations. We repeat the same process for different size initial slowness perturbations. We set the bounds of the

constraints imposed during the inversion (Section 4.2) as the maximum perturbation allowed, corresponding to two std of the Gaussian distribution used to generate the random errors. We then perform several tests with decreasing percentages of this maximum perturbation, from 100% to 0.1%. In all tests data are fitted perfectly, while hypocentre locations and slowness components are recovered to some extent, depending on the initial slowness perturbation. The average results for 100 repetitions of this test show that:

- the smaller the perturbation of the initial slowness vector the better hypocentre locations are recovered (with perfect recovery for an unperturbed initial slowness vector). For small perturbations, most of the relocations occur at the initial, 0^{th} iteration. This is expected since in this case the non-linearity is weak;
- the slowness vector (in terms of azimuths, incidence angles and P and S velocity) is adjusted, iteration by iteration, towards the truth, with a reduction of the std (compared to the true slowness) of 50 to 70% achieved (greater proportional reduction when starting with less perturbed slowness;
- when the slowness perturbation applied is small (up to 20% of the maximum perturbation allowed) the hypocentral locations do not change significantly after the initial 0^{th} iteration, although the slowness vector changes and moves towards the truth;
- for larger slowness perturbations (up to the maximum), the hypocentral mislocations reduce with iteration, but the mean mislocation reduction (in terms of distance between true and calculated locations) only reaches a maximum on the order of 30-40% for the maximum initial slowness perturbation.

These tests demonstrate effects of the non-linearity of the problem and that trade-offs occur between location parameters and the slowness vector. The function we try to minimize has multiple minima that may prevent the inversion from reaching the global minimum. This, in turn, means that the final relative locations obtained may depend on the initial slowness vector. However, the true slowness vector is successfully recovered by at least 50% in all of our tests and, even for the larger initial slowness perturbations, the hypocentre mislocations are significantly reduced also, after the 0^{th} iteration, when introducing the inversion for slowness.

6. Relative relocation results

Since the synthetic tests demonstrate a trade-off between relative relocations and slowness vector, we compute the inversion with different starting slowness vectors and compare the results. We perturb the initial guess of the slowness vector (obtained as described in Section 4.1) with 25%, 50% and 100% of the maximum allowable random perturbation, for a

total of 8 inversions. All inversions converge to similar results both in terms of relative relocations and slowness vectors. The initial misfit (after inversion for origin time), normalized by the data covariance and scaled by the number of degrees of freedom, is 9.2. At the 0th iteration, it ranges for the 8 inversions between 4.9 and 5.5, with larger values for larger slowness perturbations. After 7 iterations, the misfit is reduced to values between 2.8- 3.1.

All inversions converge to a similar size and shape of the cloud of hypocentres and the slowness vector components move in the same direction. However, they do not converge to the same values, as observed in Fig.5 where the resulting azimuth angles are reported as average over the 8 inversions and corresponding std. The results indicate that the variation increases with distance between station and seismic cluster. This is expected, as scattering effects are likely to increase for longer travel-distance, together with the width of the Fresnel zone. In some cases, the P and S azimuth angles move to opposite directions compared to the initial value. Also, for P waves the azimuths deviate more from straight paths, compared to S waves.

The resulting relative relocations are shown in Figs. 6-7. Fig. 6 shows a comparison of the absolute IMO catalogue locations, absolute non-linear locations obtained by Sgattoni *et al.* (2015) and the relative relocations obtained in this study. The spatial distribution of 870 catalogue locations spans an area several km wide, with a formal uncertainty on the order of 1 km. The non-linear locations of 32 events, obtained with the addition of 2 temporary stations within 2 km from the cluster, are concentrated in a smaller area, less than 1 km wide, with uncertainty estimates around 400 m. Our relative locations of 1140 events cover an even smaller area, few hundred meters wide, with horizontal relative uncertainty on the order of 15-40 m (Figs. 7-8).

The std estimates for the 3 spatial components (Fig. 8) indicate that the uncertainty in depth is about twice that in the horizontal directions. There are also changes with time: starting from January 2012 the std and its variability increase in all directions.

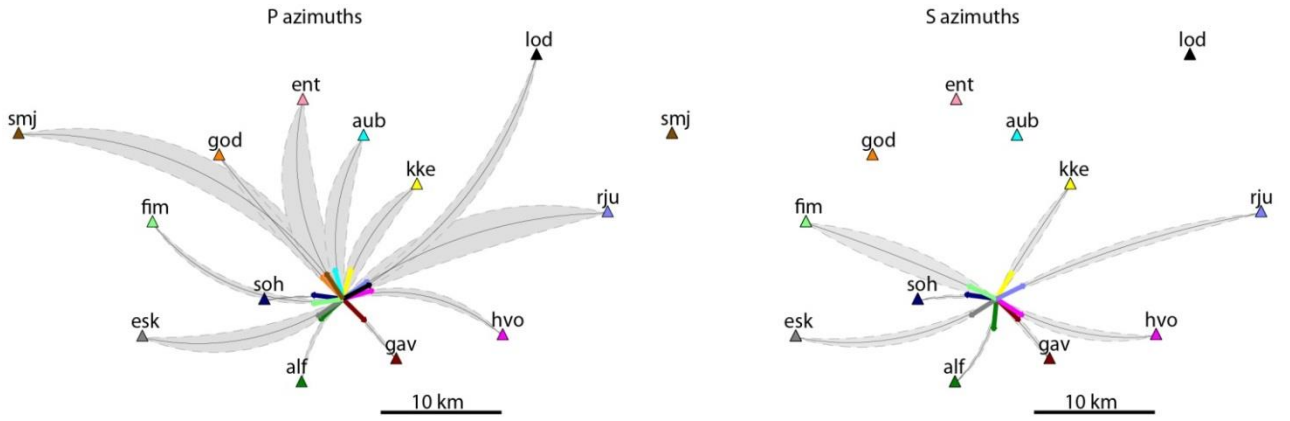

Fig. 5. Average azimuth vectors and their std for all 8 inversions performed, with different starting slowness vectors. P and S azimuths are drawn separately, as the inversion is performed separately.

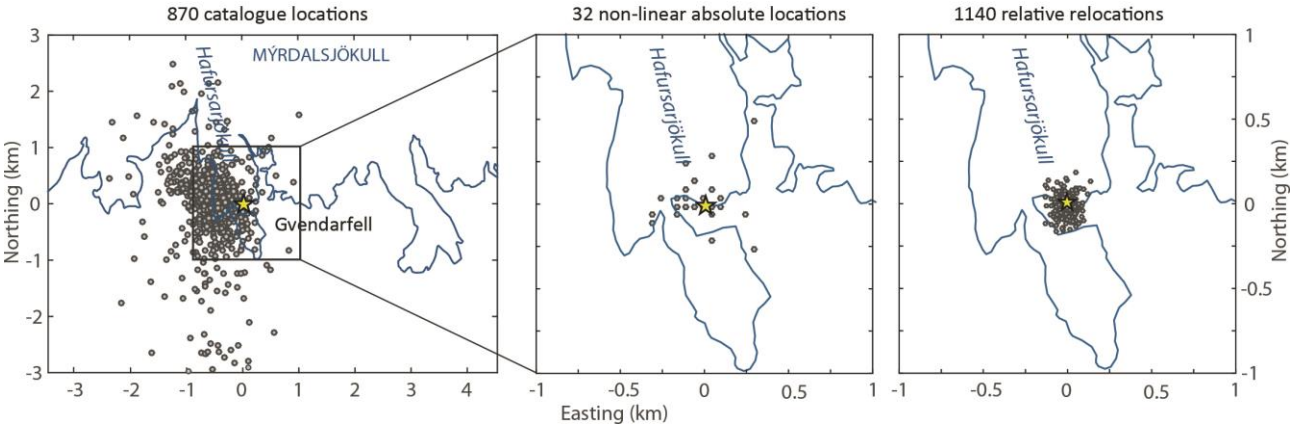

Fig. 6. Map view of 870 events from the IMO catalogue, 32 non-linear absolute locations (Sgattoni *et al.* 2015) and 1140 relative relocations. The yellow star is the master event location, corresponding to the centre of the non-linear absolute locations (at N63º32.772', W19º05.988' and depth corresponding to the local surface elevation) and is the origin of the axes scale. The blue line is the glacier outline derived from LiDAR DEM obtained in 2010 (Jóhannesson *et al.* 2013). The spatial distribution of the hypocentres is reduced with the relative relocation from several km to tens of m.

This correlates with changes in correlation coefficient and related data uncertainty estimates and the decrease in the number of observations per event (Fig. 4). In Fig. 7 we report the locations and error bars for all events (950) with a smaller std than 60 m on all three directions. The average std on the horizontal components corresponds to 14 m before January 2012 and 33 m after that. The average std in depth increases from 32 m to 45 m. In order to estimate the size of the cluster, we derive the combined probability density distribution of the whole cluster by summing the distribution of all individual events (based on their location uncertainties). Although visually the size of the cluster appears to increase in the second time period (after January 2012, Fig. 7), there is in fact no significant change, since the uncertainty increases as well. The resolved size of the cluster is estimated to be on the order of 25x50x100 m (easting, northing, depth). There is indication of a shift in location between the two time periods on the order of 30 m towards south, but this is not resolved as it is below the level of uncertainty.

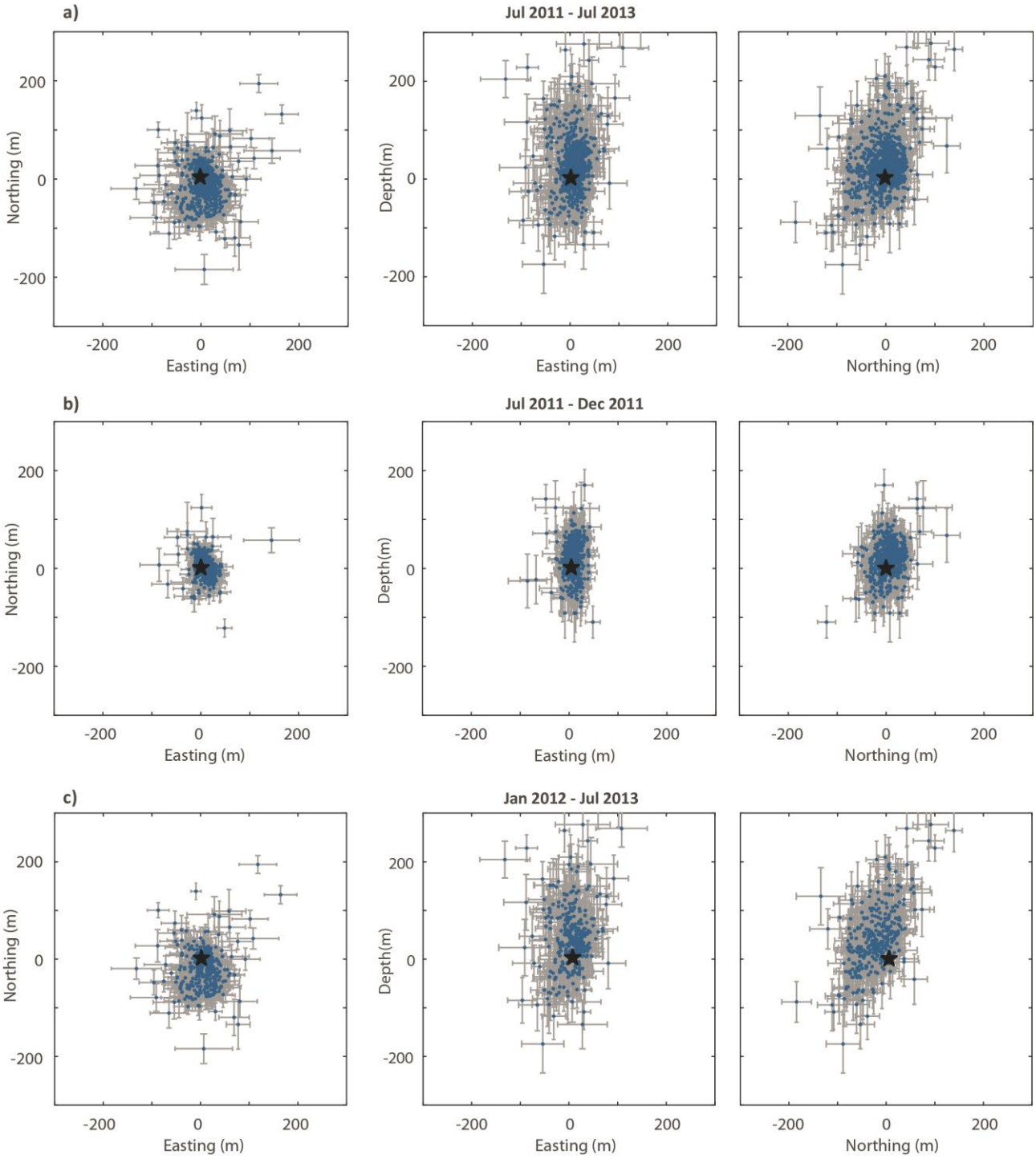

Fig. 7. Relative relocation results for all events with a smaller std than 60 m in all directions. Blue points are the locations and grey lines represent uncertainty (± std). The star is the master event location, corresponding to the origin point of the axes. a) 950 events for the entire time period (July 2011 and July 2013). b) 550 events, until December 2011 c) 400 events, from January 2012.

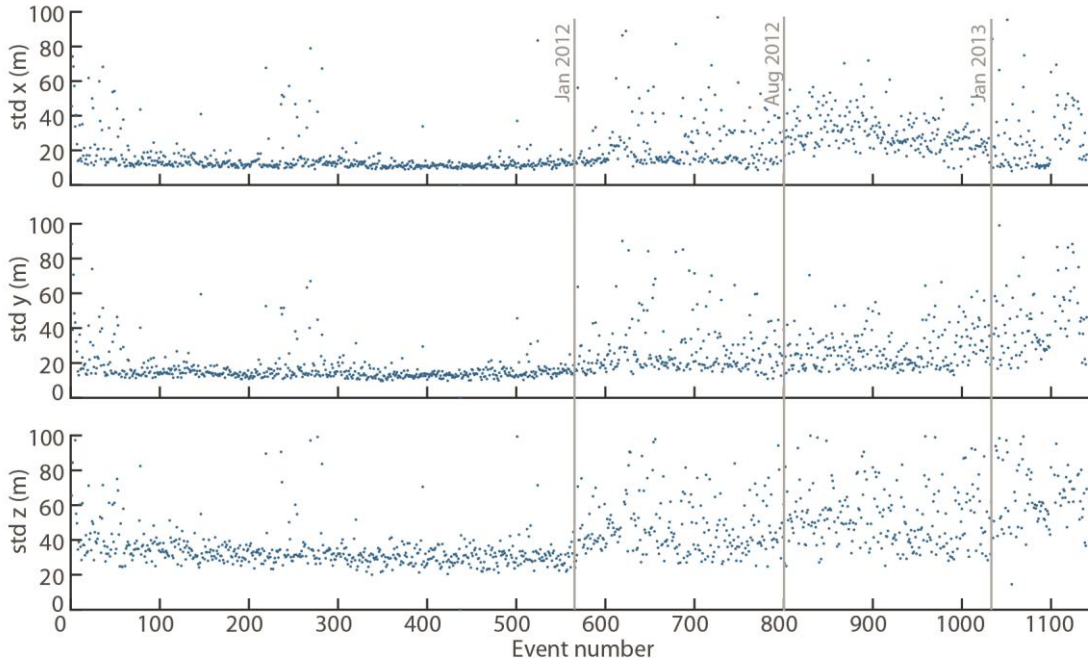

Fig. 8. Estimated std of the relative relocation spatial coordinates x (easting), y (northing), z (depth). A clear increase starts in January 2012 and peaks in August 2012.

7. Discussion and conclusions

We have located with a relative relocation strategy around 1100 shallow, repeating LP seismic events located on Katla volcano's south flank, at Gvendarfell. This seismicity started in 2011, in coincidence with an unrest episode that culminated in a glacial flood and is characterized by a strikingly regular temporal pattern, with regular intervals between repeating seismic events, modulated by a seasonal variation. Sgattoni *et al.* (2015) suggested that this seismic activity may be related to hydrothermal processes, although no evidence for hydrothermal activity was found in the area. As they occur at the rim of the glacier, both volcanic and glacial processes must be taken into account as possible sources. Information on the size and shape of the seismic cluster may help constraining the source process. This motivated our detailed study in order to extract information on the hypocentre distribution.

The extreme similarity of all waveforms indicates a very small spatial distribution of hypocentres. In order to extract meaningful information about size and shape of the cluster, we have optimized the cross-correlation measurements and relative-relocation process in order to minimize uncertainty. With a synthetic test we determined the best parameters for differential-time measurements and estimated their uncertainties, specifically for each waveform. This allowed avoiding further generalized statistical assumptions about errors.

We have then relocated the events with a master-event approach, which is justified by the small size of the problem: the waveforms are so similar that the master event is well

correlated with all others. The 1D velocity model assumption that is usually made in most location strategies is not likely to describe reality in volcanic areas where strong heterogeneities are expected. Therefore, we have designed the relocation strategy to work without a predefined velocity model, by formulating and inverting the problem to seek changes in both location and slowness. This strategy accounts for azimuth, take-off angles and velocity deviations from a 1D model and allowed to considerably improve the data fit. When allowing the slowness vectors to be changed during the inversion, the misfit is reduced by almost 50% and approaches its expected value. In order to propagate data errors through the calculation, we have solved the inversion explicitly and estimated a location covariance matrix.

We have tested the program synthetically and observed a trade-off between relocations and slowness that lies in the nature of the problem, which is non-linear and in which the model parameters are coupled as factors in the same term (Eq. 4). For this reason, we have performed the inversion with several initial slowness vectors. All inversions resulted in similar hypocentre distributions and slowness values and angles.

The Gvendarfell seismic cluster appears to be distributed over a volume with depth distribution on the order of 100 m and horizontal distribution on the order of 25x50 m. This allows some considerations about the interpretation of the source:

- there is no suggestion that the shape of the cluster has a single plane-like geometry. Therefore, there is no evidence that the seismic events are generated by fault movement, despite the fact that a recent fault was identified in the area (Chapter 6).
- the depth distribution of the hypocentres suggests that these events are unlikely to be generated by glacial processes, as the ice thickness is not expected to exceed few tens of meters in the area where the cluster is located. Therefore, volcano-related processes, magmatic or hydrothermal, are more likely, as suggested also by Sgattoni *et al.* (2015).
- the size and shape of the cluster do not exclude or point to a specific volcano-related source. In the case of a hydrothermal source, the size may be consistent with e.g. a crack or a crack volume filled with hydrothermal fluid. Alternatively, a small batch of magma rising at shallow depth may act as a source. The size of the cluster is consistent with the size of silicic magma bodies identified in the Gvendarfell area (Chapter 6).

Some indications of minor temporal changes are suggested by decreased cross-correlation coefficient and increased location uncertainty after January 2012. While the location uncertainty may be influenced by e.g. network configuration changes, a systematic decrease in correlation coefficient may be associated with a decrease in the size of the events or with changes in either source process or hypocentre locations. There is no clear correlation between

magnitude and correlation coefficient variations or between the systematic increase in location uncertainty and the changes in the network configuration. We suggest, therefore, that time changes in either the source process or hypocentre location may have occurred starting from January 2012. There is an indication of a shift of the hypocentres towards south, but this is below the uncertainty level. It is not straightforward to infer what this time change would imply for the source interpretation.

Aknowledgements

The authors would like to thank the Icelandic Met Office for access to waveform of the Gvendarfell events. The temporary deployments producing data for this study were supported by CNDS (Centre for Natural Disaster Science, www.cnds.se) at Uppsala University and the Volcano Anatomy project, financed by the Icelandic Science Foundation. This work was funded by the University of Bologna, University of Iceland and Uppsala University, as a part of a joint PhD project.

References

Chouet, B.A., 2003. Volcano Seismology, *Pure appl. geophys.*, **160**, 739-788.

Deichmann, N. & Garcia-Fernandez, M., 1992. Rupture geometry from high-precision relative hypocenter locations of microearthquake clusters, *Geophys. J. Int.* **110,** 501–517.

Fréchet, J., 1985. *Sismogenèse et doublets sismiques*, MS thesis, Université Scientifique et Médicale de Grenoble, Grenoble, France.

Frémont, M.J. & Malone, S.D., 1987. High precision relative locations of earthquakes at Mount St. Helens, Washington, *J. Geophys. Res.*, **92**(B10), 10223–10236.

Geller, R.J. & Mueller, C.S., 1980. Four similar earthquakes in central California, *Geophys. Res. Lett.*, **7**, 821–824.

Got, J.-L., Fréchet, J. & Klein, F.W., 1994. Deep fault plane geometry inferred from multiplet relative relocation beneath the south flank of Kilauea, *J. Geophys. Res.*, **99**(B8), 15375–15386.

Ito, A., 1985. High resolution relative hypocenters of similar earthquakes by cross-spectral analysis method, *J. Phys. Earth.,* **33,** 279–294.

Jóhannesson, T., Björnsson, H., Magnússon, E., Guðmundsson, S., Pálsson, F., Sigurðsson, O., Thorsteinsson, T. & Berthier, E., 2013. Ice-volume changes, bias estimation of mass-

balance measurements and changes in subglacial lakes derived by lidar mapping of the surface Icelandic glaciers, *Ann. Glaciol.*, **54**(63), 63–74. doi:10.3189/2013AoG63A422

Lees, J. M., 1998. Multiplet analysis at Coso geothermal, *Bull. Seism. Soc. Am.,* **88,** 1127–1143.

Michelini, A. & Lomax, A., 2004. The effect of velocity structure errors on double-difference earthquake location, *Geophys. Res. Lett.*, **31**, L09602, doi:10.1029/2004GL019682.

Poupinet, G., Ellsworth, W.L. & Fréchet, J., 1984. Monitoring velocity variations in the crust using earthquake doublets; an application to the Calaveras Fault, California, *J. Geophys. Res.*, **89**, 5719–5731.

Rowe, C.A., Thurber, C.H., and White, R.A., 2004, Dome growth behavior at Soufriere Hills Volcano, Montserrat, revealed by relocation of volcanic event swarms, 1995–1996. *J. Volcanol. Geotherm. Res.*, **134**(3), 199–221.

Scherbaum, F. & Wendler, J., 1986. Cross spectral analysis of Swabian Jura (SW Germany) three-component microearthquake recordings, *J. Geophys.,* **60,** 157–166.

Sgattoni G., Jeddi, Z., Guðmundsson, Ó., Einarsson, P., Tryggvason, A., Lund, B. & Lucchi, F. Long-period events with strikingly regular temporal patterns on Katla volcano's south flank (Iceland), *arXiv:1511.05852 http://arxiv.org/ftp/arxiv/papers/ .*

Slunga, R., Rögnvaldsson, T. & Bödvarsson, R., 1995. Absolute and relative location of similar events with application to microearthquakes in southern Iceland, *Geophys. J. Int.,* **123**, 409–419.

Thelen, W.A., Crosson, R.S. & Creager, K.C., 2008. Absolute and relative locations of earthquakes at Mount St. Helens, Washington, using continuous data; implications for magmatic processes, in *A volcano rekindled; the renewed eruption of Mount St. Helens, 2004–2006, pp. 71-89,* ed. Sherrod, D.R., Scott, W.E. & Stauffer, P.H., U.S. Geological Survey Professional Paper

Van Decar, J.C. & Crosson, R.S., 1990. Determination of teleseismic relative phase arrival times using multi-channel cross-correlation and least-squares, *Bull. Seism. Soc. Am.,* **80,** 150–169.

Waldhauser, F. & Ellsworth, W.L., 2000. A double-difference earthquake location algorithm; method and application to the northern Hayward Fault, California, *Bull. Seism. Soc. Am.*, **90**, 1353–1368.

Wolfe, C.J., 2002. On the mathematics of using difference operators to relocate earthquakes, *Bull. Seism. Soc. Am.*, **92**, 2879–2892.

5. PAPER 3

The 2011 unrest at Katla volcano: location and interpretation of the tremor sources

Giulia Sgattoni[1,2,3], Ólafur Guðmundsson[3], Páll Einarsson[2], Federico Lucchi[1], Ka Lok Li[3], Hamzeh Sadeghisorkhani[3], Roland Roberts[3], Ari Tryggvason[3]

[1] *Department of Biological, Geological and Environmental Sciences, University of Bologna, Bologna, Italy*

[2] *Institute of Earth Sciences, Science Institute, University of Iceland, Reykjavik, Iceland*

[3] *Department of Earth Sciences, Uppsala University, Uppsala, Sweden*

To be submitted to *Journal of Volcanology and Geothermal Research*

Abstract

A 23 hour tremor burst was recorded on July 8-9th 2011 at the Katla subglacial volcano, one of the most active and hazardous volcanoes in Iceland. This was associated with deepening of cauldrons on the ice cap and a glacial flood that caused damage to infrastructure. Increased earthquake activity started a few days before inside the caldera and lasted for months afterwards and a new seismic activity started on the south flank. No visible eruption broke the ice and the question arose as to whether this episode relates to a minor subglacial eruption and the tremor was generated by volcanic processes or by the flood. The tremor signal consisted of bursts with varying amplitude and duration. We have identified and described three different tremor components, based on amplitude and frequency features. A tremor phase associated with the flood was recorded only at stations closest to the river that flooded, correlating in time with rising water level observed at gauging stations. Two other phases have been located near the active ice cauldrons with back-projection of single and double cross-correlation envelopes and interpreted to be caused by volcanic or hydrothermal processes. The highly increased seismicity and evidence of rapid melting of the glacier may be explained by a minor sub-glacial eruption. It is also plausible that the tremor was generated by hydrothermal boiling and/or explosions with no magma involved. This may have been induced by pressure drop triggered by the release of water when the glacial flood started. All interpretations require an increase of heat released by the volcano.

Keywords: Iceland, Katla volcano, volcanic tremor, flood tremor, sub-glacial eruption, hydrothermal boiling

1. Introduction

A wide range of seismic signals are recorded at volcanoes, generated by several processes, including magmatic, geothermal or tectonic processes. Volcanic tremor and long-period (LP, Chouet, 1996) events are thought to be generated by fluid movements in association with volcanic eruptions or hydrothermal activity (Chouet, 2003; McNutt, 2005). Since they often precede or accompany eruptions, understanding these phenomena is of major interest for volcano monitoring. The precise mechanisms responsible for generating those signals are, however, still debated, particularly for tremor, which is a more complex signal compared to earthquakes and is difficult to locate as picking first arrivals is usually not possible (Konstantinou and Schlindwein, 2002).

Volcanic tremor is a persistent seismic signal, observed only at active volcanoes, that lasts several minutes to several days and is observed prior to or during most volcanic eruptions (Fehler, 1983; Julian, 1994; Ripepe, 1996; Métaxian et al., 1997). Because of the absence of clear onsets of waves, volcanic tremor cannot be located with conventional arrival time methods. Therefore, other techniques have been developed, based for example on phase coherency of signals among stations, either with seismic arrays (e.g. Furumoto et al., 1990; Goldstein and Chouet, 1994; Métaxian et al., 1997) or with sparse seismic networks (Guðmundsson and Brandsdóttir, 2010; Ballmer et al., 2013; Droznin et al., 2015). Alternatively, the signal amplitude distribution at different stations can be used to infer the source location (e.g. Battaglia and Aki, 2003; Di Grazia et al., 2006), when the amplitude decay with distance has a simple pattern.

A variety of source models have been proposed for the generation of volcanic tremor, including excitation and resonance of fluid-filled cracks (Chouet, 1992; Benoit and McNutt, 1997), fluid-flow-induced oscillations of conduits transporting magmatic fluids (Julian, 1994), magma column wagging (Jellinek and Bercovici, 2011) and frictional flow (Dmitrieva et al., 2013). There are also observations of tremor composed by interfering, closely-spaced LP events, e.g. at Montserrat (Baptie et al., 2002). Tremor resembling volcanic tremor has been recorded in association with hydrothermal activity, defined as 'non-eruption tremor' by Leet (1988). This is generated by bubble growth or collapse due to hydrothermal boiling. A similar source has been suggested for geothermal noise at Ölkelduháls, SW Iceland (Guðmundsson and Brandsdóttir, 2010). Tremor has been recorded also in association with hydrothermal explosions occurring as a consequence of pressure drop on the hydrothermal system, triggered for example by landslides (Jolly et al., 2014).

At subglacial volcanoes, a number of other processes related to glacier dynamics can be responsible for producing seismic signals. In addition to glacial earthquakes, due to e.g. glacier sliding, crevassing, ice falls (e.g. Métaxian et al., 2003; Jónsdóttir et al., 2009), seismic tremor can be generated in association with glacial floods, which in turn can be caused by subglacial volcanic eruptions or by drainage of subglacial lakes formed by geothermal activity (Guðmundsson et al., 2008). Seismic tremor generated by jökulhlaups (glacial floods) has been recorded several times in Iceland, e.g. from the Skaftá cauldrons on Vatnajökull ice cap (Zóphóníasson and Pálsson, 1996) during the Gjálp eruption in 1996 (Einarsson et al., 1997), but no detailed description is available in the literature.

Sometimes, glacial and volcanic processes are acting together and it is difficult to discern whether or not an eruption has started, or even occurred at all, under a glacier. It is very important for volcano monitoring to be able to discern between these different signals

and processes, particularly in Iceland, where a number of large volcanoes are covered by ice. One of these is Katla, located under Mýrdalsjökull glacier in south Iceland, just east of Eyjafjallajökull. After the eruption of Eyjafjallajökull in 2010, attention was attracted to the neighbouring Katla, as some previous eruptions of Eyjafjallajökull had been followed by more powerful eruptions of Katla (Einarsson and Hjartardóttir, 2015). The two volcanoes are tectonically connected (Einarsson and Brandsdóttir, 2000) and are both covered by glaciers. Therefore, their volcanic activity is dominated by explosive eruptions due to magma - ice interaction. The erupted volumes from Katla have been at least one order of magnitude bigger than its neighbour's (Sturkell et al., 2010).

Katla's last eruption to break the ice surface occurred in 1918 and the present repose time is the longest known in historical times (Larsen, 2000). However, two minor sub-glacial eruptions with no tephra emission into the atmosphere possibly occurred in 1955 and 1999. Both were accompanied by formation of new ice depressions (cauldrons) on the ice surface and jökulhlaups, but no visible eruption through the ice. During the 1999 unrest, a tremor signal was recorded (e.g. Thorarinsson, 1975; Sigurðsson et al., 2000). A similar episode occurred recently in July 2011, when increased seismicity was recorded, together with a tremor burst and a jökulhlaup (glacial flood) that drained from south-east Mýrdalsjökull and destroyed a bridge on the main road. One important question is whether this unrest is due to a minor subglacial eruption and the tremor associated to volcanic processes (magmatic or hydrothermal) or to the flood.

In this article we analyse the 2011 tremor signal and associated seismicity. We use cross-correlation methods to extract information about the source location. We study the time evolution of tremor attributes, such as amplitude and frequency, and compare them with direct hydrological observations and the evolution of the earthquake activity, to constrain possible sources.

2. The Katla volcanic system

The Katla volcanic system consists of a central volcano with a 110 km2 summit caldera (up to 14-km wide; Fig. 1) filled with the 600 to 750 m thick ice of Mýrdalsjökull glacier (Björnsson et al., 2000) and the Eldgjá fissure system which extends 75 km to the northeast (Larsen, 2000; Thordarson et al., 2001; Fig. 1). It is located south of the intersection between the Eastern Volcanic Zone and the transform boundary of the South Iceland Seismic Zone (Sturkell et al., 2008) and forms a part of the Eastern Volcanic Zone.

The caldera wall is breached in three places, to the south-east, north-west and south-west. These gaps provide outflow paths for ice in the caldera to feed the main outflow glaciers, Kötlujökull, Entujökull and Sólheimajökull and are the potential pathways for melt water from the glacier in jökulhlaups (Sturkell et al., 2010). Several ice cauldrons (at least 16) are located within and at the caldera rim, representing the surface expression of subglacial geothermal activity. Changes in their geometry are monitored to detect variations of geothermal heat release (Guðmundsson et al., 2007).

A velocity anomaly at shallow depth, revealed by seismic undershooting, was interpreted as evidence of a magma chamber (Guðmundsson et al., 1994) and a non-magnetic body was identified within the same region with an aeromagnetic survey (Jónsson and Kristjánsson, 2000). The presence of a magma chamber is supported by geobarometry analyses on historical tephra samples, conducted by Budd et al. (2014), but is questioned by tephra stratigraphy studies by Óladóttir et al. (2008).

2.1. Recent activity and seismicity

Apart for the large Eldgjá lava eruption in AD 934-940 (Thordarson et al., 2001), all historical eruptions of the Katla volcanic system, at least 20, occurred within the caldera (Larsen, 2000) and consisted mainly of basaltic phreatomagmatic eruptions, capable of producing destructive glacial floods. The last eruption to break the ice-surface was an explosive basaltic eruption in 1918. It lasted for about three weeks and was accompanied by a massive jökulhlaup (Sveinsson, 1919). The eruption site was located near the south rim of the caldera, beneath about 400 m of ice. The height of the eruptive plume was estimated as 14 km a.s.l. (Eggertsson, 1919), the volume of tephra fall-out around 0.7 km^3 and the volume of water-transported material is estimated to be between 0.7 and 1.6 km3 (Larsen, 2000).

Persistent seismic activity has been observed at Katla since the first sensitive seismographs were installed (in the 1960s). When reasonably accurate locations became available, the activity was shown to occur in two distinct main areas: within the caldera and at Goðabunga on the western flank (Einarsson and Brandsdóttir, 2000). The seismicity inside the caldera consists of high frequency and hybrid events, probably associated with the subglacial geothermal activity (Sturkell et al., 2010) and volcano-tectonic processes. The Goðabunga cluster consists mainly of long-period shallow events and has a controversial interpretation, as a response to a slowly-rising viscous crypto-dome (Soosalu et al., 2006) or in association with ice fall events (Jónsdóttir et al., 2009). Periods of high seismicity were observed in 1967 and 1976-77 (Einarsson, 1991). In the 1976-77 episode, both epicentral areas were active, i.e. both within the caldera and at Goðabunga.

The two possible minor sub-glacial eruptions in 1955 and 1999 both occurred at the caldera rim. The 1955 event took place at the eastern rim of the caldera. Two shallow ice-cauldrons formed and a small jökulhlaup drained from Kötlujökull, i.e. south-east Mýrdalsjökull (Thorarinsson, 1975). The 1999 event took place in July at the south-western rim. Seismic stations around the glacier recorded earthquakes and bursts of tremor that culminated in the release of a jökulhlaup from Sólheimajökull, i.e. south-west Mýrdalsjökull (Sigurðsson et al., 2000; Roberts et al., 2003). A new cauldron also formed on the surface of the glacier (Guðmundsson et al., 2007).

From 1999 to 2004, uplift of the volcano was revealed by GPS measurements on the caldera rim, interpreted to result from 0.01 km^3 magma accumulation (Sturkell et al., 2006; 2008). This interpretation was supported by the evidence of increased geothermal heat output observed in 2001-2003, based on the evolution of ice cauldrons (Guðmundsson et al. (2007). A recent study by Spaans et al. (2015), suggested, instead, that the 1999-2004 uplift may be due to glacial isostatic adjustment as a consequence of mass loss of Iceland's ice caps.

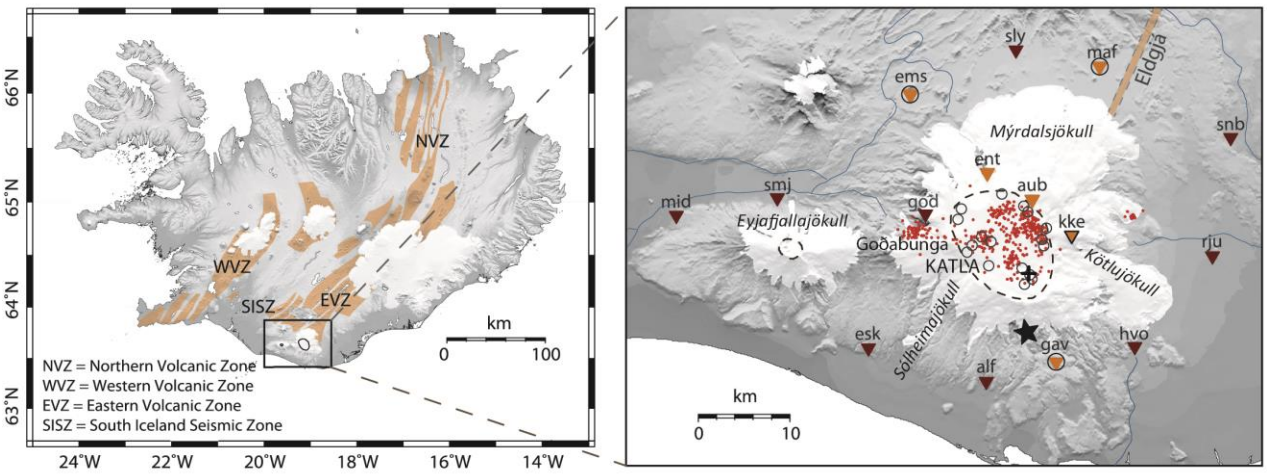

Fig. 1. Map of Iceland showing the different volcanic systems (in orange; from Einarsson and Sæmundsson, 1987). In the inset, the seismic network operating during the tremor and the main seismic and geological features of Katla are shown. Dark brown triangles: permanent Icelandic Meteorological Office (IMO) seismic stations. Orange triangles: temporary Uppsala University seismic stations operating during 29 May 2011 - August 2013 (no outline), during 6 July 2011 - August 2014 (black outline) and during 10 July 2011 – August 2013 (black circle). Red dots: epicentres at Katla before July 2011. These are mostly localized in two distinct source areas, within the caldera and on the west flank at Goðabunga. The star marks the new cluster on the south flank, started in July 2011 (Sgattoni et al., 2015). The Katla and Eyjafjallajökull caldera rims are outlined by dashed lines. Open circles correspond to ice cauldrons in the Mýrdalsjökull glacier (Guðmundsson et al., 2007). White areas are glaciers. To the NE, the location of Eldgjá fissure is shown. The black cross in the south-eastern caldera marks the site of the 1918 eruption.

3. July 2011 unrest: Course of events

Between August 2010 and July 2011, most of the ice cauldrons on the Mýrdalsjökull glacier uplifted by 6 to 8 m, as interpreted by Guðmundsson et al. (2013) due to water accumulation under the glacier. The greatest rise, 11-12 m was observed at cauldron 16 (Fig. 2; Guðmundsson et al., 2013).

Since the beginning of July 2011, the seismicity intensified, especially inside the caldera, and culminated on July 8-9th, when continuous tremor was recorded, starting at ~19:00 GMT on July 8th. No signs of eruption breaking the ice were seen, but a jökulhlaup drained from Kötlujökull and deepening of some ice cauldrons was observed on the surface of Mýrdalsjökull in the southern and eastern parts of the caldera (Fig. 2). The jökulhlaup (~18 million m3) swept away the bridge on the main road 1 over Múlakvísl river around 05:00 GMT on July 9th, one hour after rising water level was detected at the gauging station Léreftshöfuð, located a few km south of Kötlujökull (IMO, 2011) and ~6 km upstream from the bridge.

Another gauging station, located on the bridge over Múlakvísl river, began to show slightly increased conductivity, reaching values close to 200 $\mu S/cm$, around midnight on July 7th. This doesn't coincide with increased water level. The conductivity later rose again above 200 $\mu S/cm$ at around midnight on July 8th and a dramatic increase occurred after midnight on July 9th, around the time of maximum of the tremor (IMO, 2011), coinciding with dramatic water level increase (Fig. 2).

Galeczka et al., (2014) conducted a study of the chemical composition of the flood water and did not find evidence that the water had come into contact with magma. They suggested, therefore, that the heat source for glacier melting was geothermal rather than magmatic.
In association with the tremor, a new source of seismic events was activated on the south flank of Katla, at the southern edge of Mýrdalsjökull glacier (Fig. 2). This seismicity has been interpreted as related to a new hydrothermal system that may have activated on Katla's south flank during this unrest episode, although no new hydrothermal area was found (Sgattoni et al., 2015; Sgattoni et al., subm). The course of events occurred in association with the 2011 unrest is reported in Table 1.

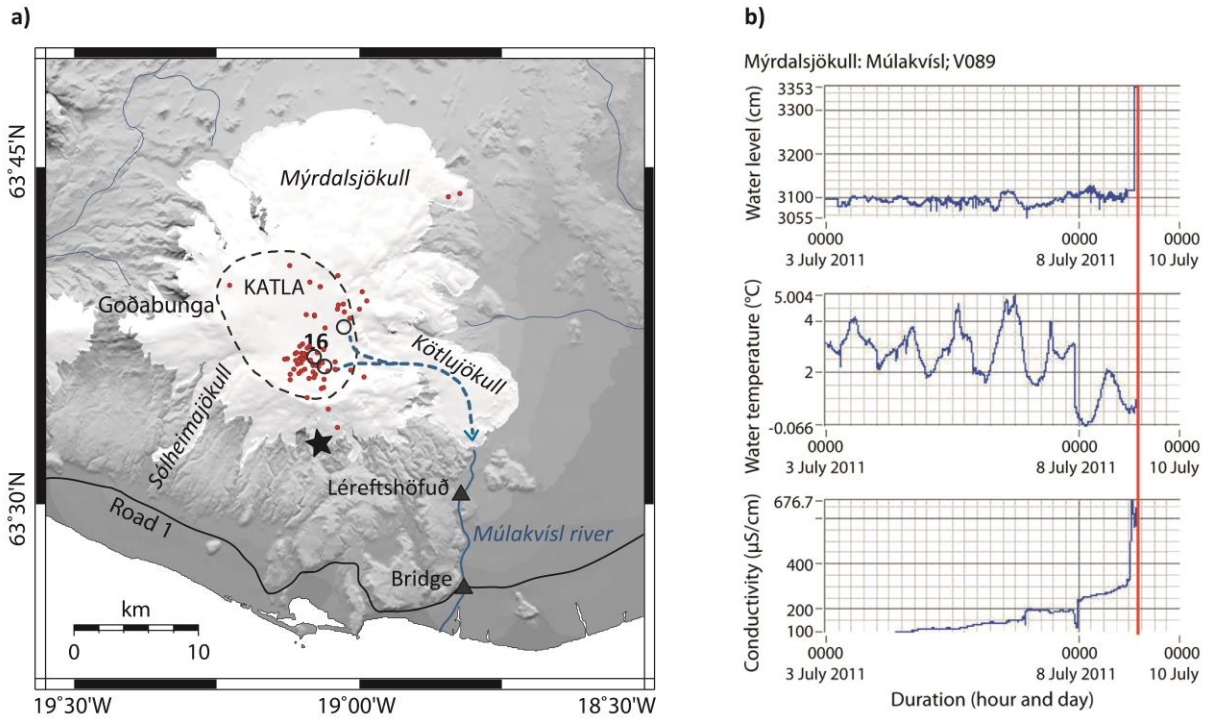

Fig. 2. a) Map of Katla showing the features related to the July 2011 unrest. Black open circles are the ice cauldrons that deepened during the unrest, number 16 is the one that showed the biggest change before and during the unrest. The dashed blue arrow shows the presumed flood path. Red dots are the earthquakes that occurred on July 8th and 9th. The 2 gauging stations are marked with black triangles, the southern one corresponding to the bridge over Múlakvísl river. The star marks the new seismic cluster on the south flank (Sgattoni et al., 2015). b) IMO continuous monitoring of water level, temperature and conductivity of Múlakvísl river. Data from the gauging station located at the bridge over the river. The red line marks the time when the station stopped working due to the flood that destroyed the bridge (IMO, 2015).

Before tremor
- from August 2010: ice cauldrons uplifting
- from beginning of July: increased seismicity inside caldera and new seismicity on south flank
8th – 9th July 2011
- July 8th, 00:00: conductivity above 200 µS/cm in Múlakvísl river
- July 8th, ~19:15: tremor starts
- July 9th, 00:00: dramatic increase in conductivity in Múlakvísl river
- July 9th, 04:00: rising water level detected at gauging station Léreftshöfuð
- July 9th, 05:00: jökulhlaup destroys a bridge on road n.1
- July 9th, 18:00: tremor ends

Table 1. Course of events that occurred in association with the July 2011 unrest at Katla.

4. Seismic network

Following the eruption of Eyjafjallajökull volcano in 2010, the IMO augmented the seismic monitoring network around Katla from 5 to 9 stations. Moreover, Uppsala University deployed additional 9 temporary stations between May-October 2011 and August 2013 (Fig 1). Three of these stations, located along the caldera rim, were deployed before the tremor episode occurred. The rest were deployed later and therefore could not be used to analyse the tremor. However, 3 of them were deployed immediately after the tremor episode, and could therefore be used to locate the earthquakes after July 9th.

Of the total 15 seismic stations used in this study, 8 stations were equipped with broadband Guralp ESPA and Guralp CMG3-ESPC sensors with a flat response from 60 s to the Nyquist frequency (50 Hz). The remaining 7 stations had 5-second Lennartz sensors. Data were recorded and digitized with Guralp and Reftek systems at 100 Hz. Stations were powered with batteries, wind generators and solar panels. All the instruments recorded in continuous mode, but some technical problems (e.g. power failure) mainly due to harsh weather condition (especially in winter time), prevented some stations from working continuously during the whole operation time. Data from a total of 10 seismic stations near the caldera and around the glacier were used to locate and analyse the tremor signal (Fig 1).

5. Earthquake activity

The seismic events inside the caldera and at Goðabunga that occurred prior to, during and after the tremor, between June 20th and July 20th have been automatically detected and located with the SIL analysis software by using manually picked P- and S- phases (Böðvarsson et al., 1998). The software uses a single event location technique, performed by minimizing the square sum of both P- and S- wave residual arrival times in a 1D velocity model. The velocity model was obtained from tomographic studies of the area (Jeddi et al., 2015). Data for the seismic events located on the south flank, instead, were obtained with cross-correlation methods, described in Sgattoni et al. (2015). The number of seismic stations changed during the time period analysed from 11 to 12 stations on July 6th (when station KKE was installed) and from 12 to 15 stations immediately after the tremor.

The cumulative number of events detected is shown in Fig. 3, separately for the three main clusters identified at Katla: Inside the caldera, at Goðabunga and on the southern flank. A sharp increase of seismicity inside the caldera occurred on July 7-8th, together with the onset of the seismicity on the south flank. The Goðabunga cluster, instead, appears to have

become less active. The increased seismicity cannot be explained only by the additional station deployed on July 6th, as can be seen in Fig. 4, where the seismicity clearly increased already on July 6th and maintained a high rate also after the tremor. A small swarm also occurred around 02:00 on July 6th (Fig. 4). After the tremor event, the seismicity remained high, but decreased slowly (Fig. 3).

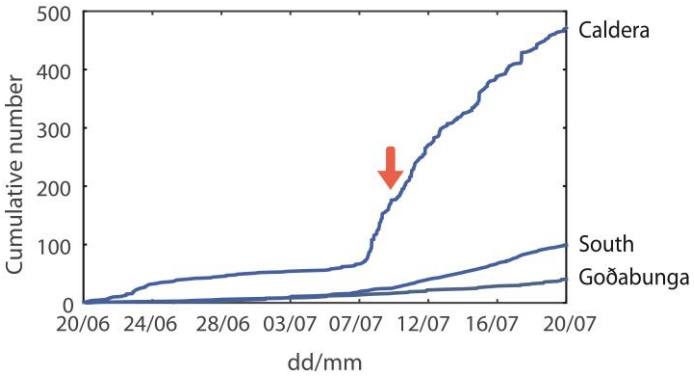

Fig. 3 Cumulative number of seismic events that occurred between June 20th and Jul 20th in the 3 main clusters at Katla. The arrow indicates the time of tremor. Data for the southern cluster are from Sgattoni et al. (2015).

We have located only events with at least 5 identified phases (P and S), for a total of 480 events between June 20th and July 20th, of which 56 occurred during the tremor (Fig. 5). However, many more earthquakes can be visually identified in the seismograms (more than 80 events during the tremor) but could not be located and are therefore not counted in the cumulative plot of Fig.3 because they were only recorded at the closest stations. This is clear when comparing the seismograms of Fig. 4: The intense seismicity at the caldera station AUB is not observed on the seismogram at station ALF, located several km south of the caldera (Fig. 4). At ALF station, however, the south-flank seismicity appears clearly, with LP events with a peculiar regular temporal pattern commencing on July 7th (Fig. 4). Only few similar, much smaller, events were observed in the months before, with no regular temporal pattern (Sgattoni et al., 2015).

The hypocentral locations of the 480 events are shown in Fig. 5. Most events are small in magnitude, with only ~100 events with magnitude M>1 (magnitudes from IMO catalogue). Based on the temporal changes of the seismicity, we defined three different time intervals: 1) 20 June – 6 July, before the increased seismicity started; 2) 6-9 July, from the increased seismicity to the end of the tremor; 3) 10-20 July, after the tremor. During the first time period, the seismicity was distributed evenly inside the caldera and at Goðabunga (Fig. 5). Some seismic events were also located near the northern active cauldron (Fig. 5). After the seismicity increased (second time interval) most of the hypocentres were clustered in the south-eastern part of the caldera (Fig. 5). More than 30 events with magnitude M>1 occurred

between July 6-9th. The largest event had magnitude equal to 2.3. After the tremor, the seismicity was mainly concentrated in the northern sector of the caldera (Fig. 5). The formal uncertainty of the locations is of the order of 1 km in the horizontal components and several km in the vertical. The distribution in depth is therefore not well resolved, as most of the stations used for the location were located at some distance from the hypocentres.

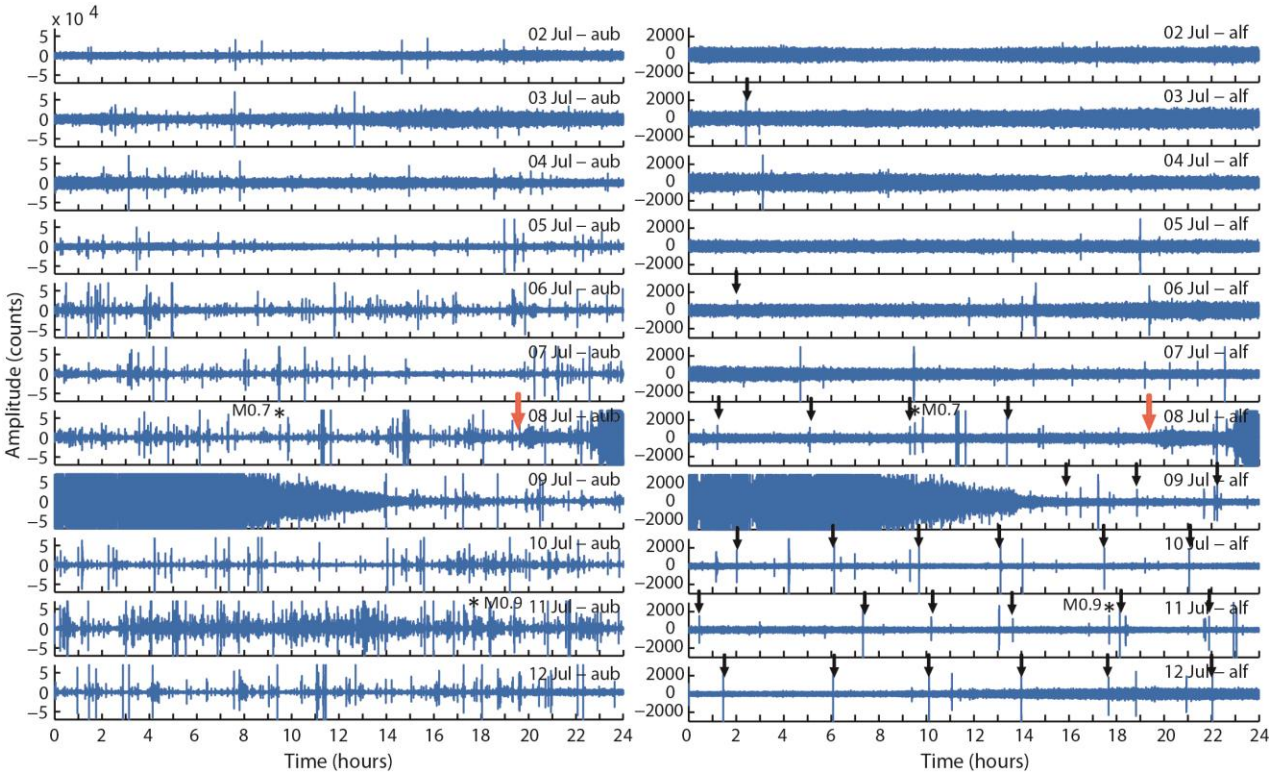

Fig. 4. Daily Z-component seismograms at stations AUB (left) and ALF (right) (see Fig. 1 for location) for the time period between July 2nd and July 12th. The orange arrow marks the onset of the tremor. The black arrows in the right panel mark the regular seismicity that started on the south flank of Katla (Sgattoni et al., 2015). The amplitude is in digital counts, proportional to velocity and the instrument response removed, so that amplitudes at the two stations are comparable. However the seismograms are clipped, for plotting reasons. The magnitudes of two events located in the south-eastern caldera are given as reference.

We will describe in more detail the waveforms of some events recorded after the seismicity picked up on 6-7th July. Most of the seismicity consisted of shallow events with varying frequency content. Most of the located events fall into two frequency ranges, 0.5-3 Hz and 0.5-10 Hz (same frequency as the tremor; see the next chapter). Before the tremor, the biggest events (high amplitude peaks in Fig. 4) fall in the second frequency range, while during the tremor there is a more even distribution of the two frequency ranges. In addition, several smaller high-frequency events, with frequency content up to 20 Hz, were recorded

mainly at the closest stations (AUB and KKE). Many of the earthquakes during the intense seismicity period observed at AUB in Fig. 4 fall into this category.

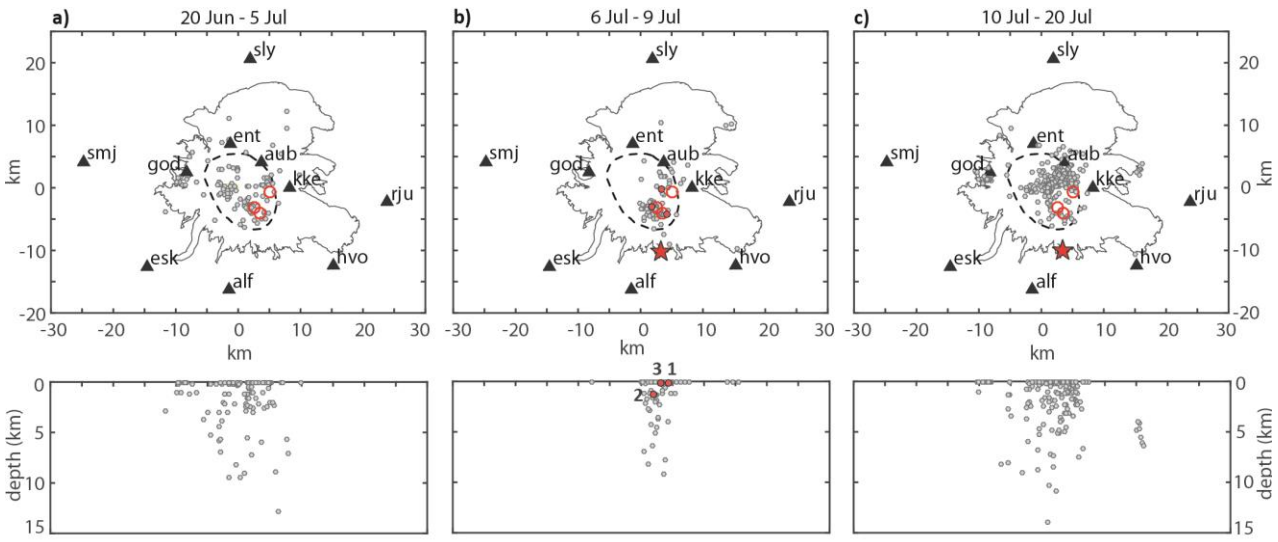

Fig. 5. Map location and depth distribution of events in three different time intervals: a) before the increased seismicity, b) after the increased seismicity until the end of the tremor, c) after the tremor. Red open circles: active cauldrons. Red star: new seismic cluster on the south flank. Red dots in panel b, labelled with 1,2,3: earthquakes shown in Figs. 6-8.

Three events, among the biggest recorded during the tremor, are shown as examples in Figs. 6-8. Two of them were located in the south-eastern caldera, close to the southern cauldron that deepened during the unrest (Fig. 5). Of these, the first is characterised by low-frequency content with a main peak between 2-3 Hz, an emergent P wave and unclear S (Fig. 6). The second is composed of a wider spectrum of frequencies, up to 10 Hz, and can be classified as hybrid, with a high frequency beginning of the seismogram and lower frequency coda (Fig. 7). Noticeably, the higher frequencies appear to be strongly attenuated at the stations located on the other side of the caldera with respect to the source, particularly at the caldera stations KKE, AUB and ENT, the last being the most attenuated. The P wave is clear at ALF and GOD, emergent at KKE and AUB, unclear at ENT. The third event (Fig. 8), located near the northern active cauldron, contains frequencies mainly between 1-4 Hz, and has an emergent P wave and unclear S.

A conspicuous number of events was detected at station HVO after the river flooded, mainly consisting of small events with frequency content between 1 and 7 Hz. Further details about this seismicity are not reported as that is beyond the scope of this article.

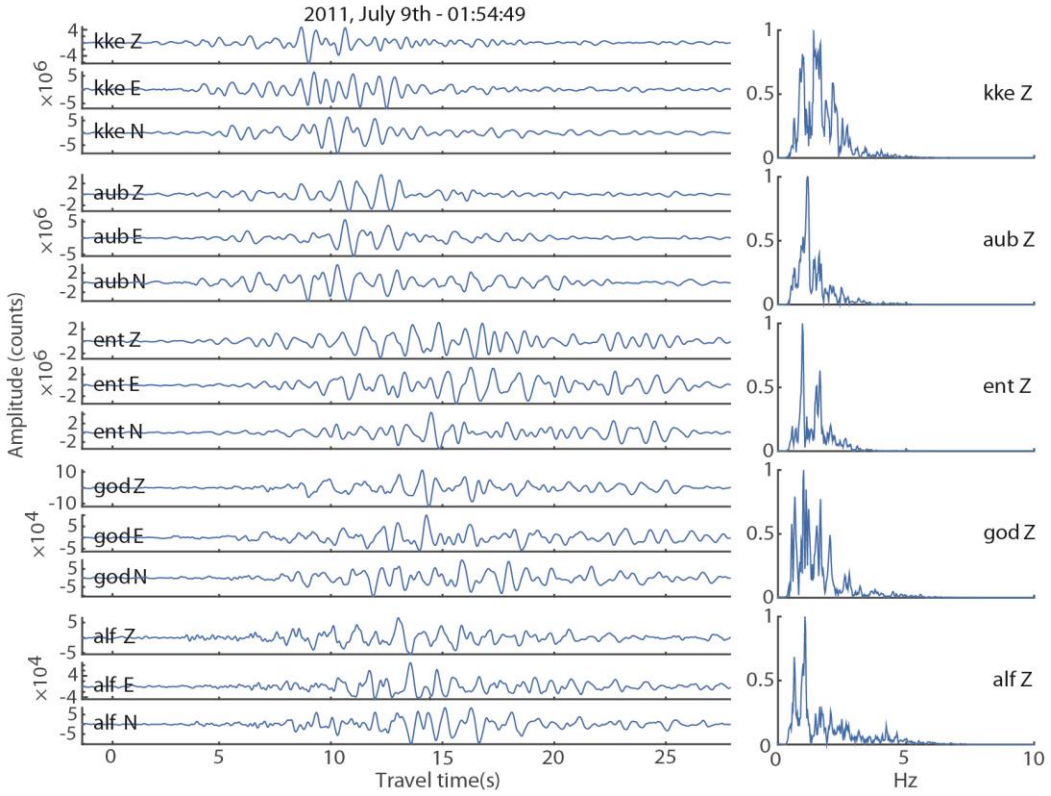

Fig. 6. Three component waveforms and Z component spectra of seismic event labelled '1' in Fig. 5. The amplitude is in digital counts, proportional to velocity. The magnitude is 1.56.

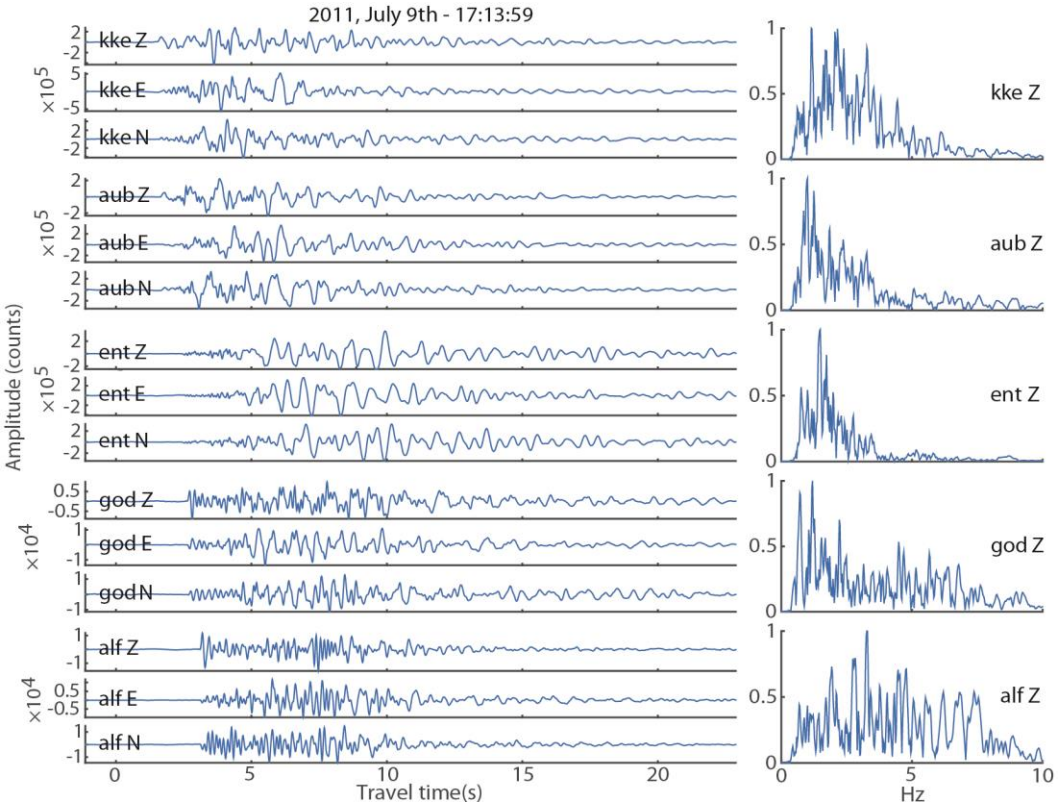

Fig. 7. Three component waveforms and Z component spectra of seismic event labelled '2' in Fig. 5. The amplitude is in digital counts, proportional to velocity. The magnitude is 1.61.

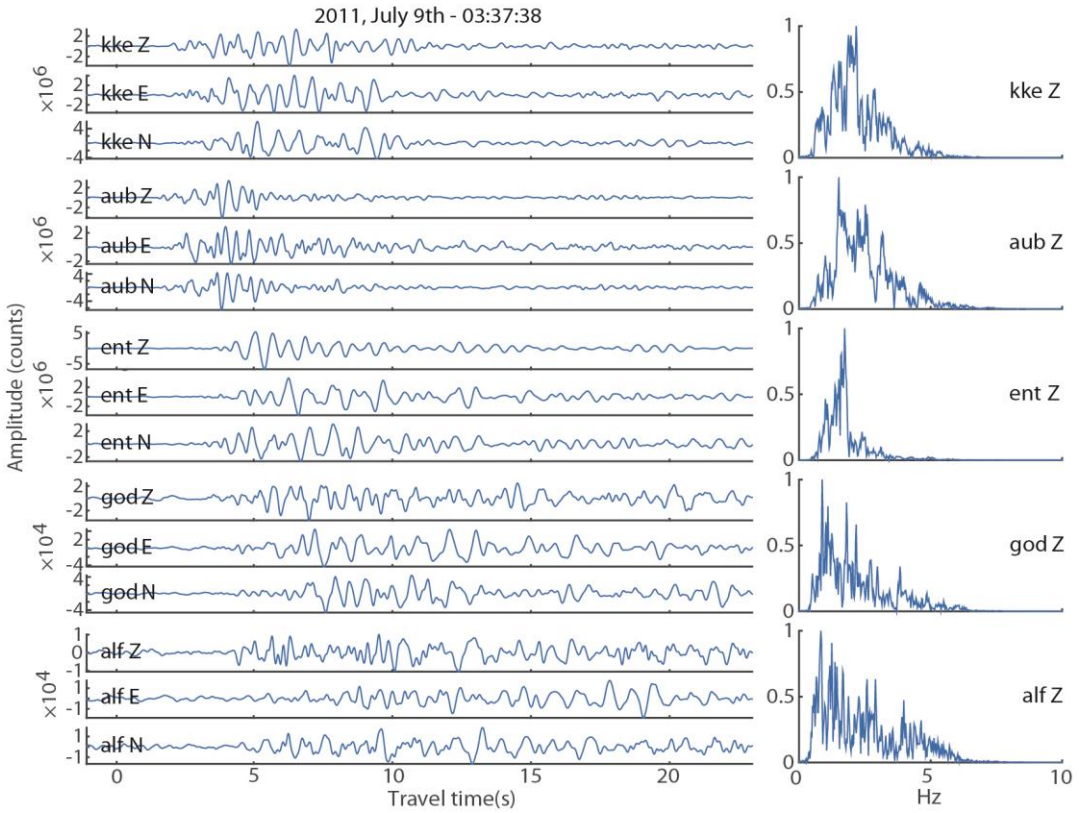

Fig. 8. Three component waveforms and Z component spectra of seismic event labelled '3' in Fig. 5. The amplitude is in digital counts, proportional to velocity. The magnitude is 1.65.

6. Frequency and amplitude characteristics of the tremor signal

6.1 Tremor pre-processing

The tremor signal is complex, with energy and frequency content varying with time. In order to study the tremor amplitude and frequency features, we first had to clean the signal from transients. As is evident from Fig. 4, persistent seismicity occurred during the days of the unrest, also during the tremor. Since many events have frequency content similar to the tremor, filtering is not effective. In addition, the amplitude time-features of the tremor change over time scales sometimes shorter than minutes, making the use of clipping strategies problematic. Therefore, in order to clean the signal from earthquakes, we used a combination of manual removal of earthquakes and clipping.

The signal has been examined in detail in order to identify local events, based on the time behaviour and on the frequency content. Seismic events usually manifest themselves in the signal as short transients with abrupt amplitude change compared to the 'background tremor'. They are also evident in the spectrograms, where they appear as peaks creating vertical lines with high amplitude compared to the adjacent time windows. By looking at both

the raw seismograms and the spectrograms, we iteratively removed signals that resembled earthquakes. The time windows containing events were cut out of the signal and tapering was applied to the sides of the window. This was then accounted for when computing amplitude spectra, by normalizing the spectral amplitude based on the length of the windows that were cut out. Furthermore, we clipped the tremorgrams in order to suppress any leftover events. This process considerably reduced the number of sharp peaks in the spectrograms and in the amplitude time-history of the tremor.

6.2 Frequency content

The main features of the tremor signal can be seen in the spectrograms of Fig. 9, The tremor started around 19:00 GMT on July 8th and lasted for about 23 hours. The energy is distributed between 0.8-10 Hz, but mainly concentrated between 0.8-4 Hz, at most stations. The tremor was strongest between 23:00 GMT (July 8th) and 05:00 GMT (July 9th), when a number of short bursts occurred, ranging between 6 and 50 minutes in duration. Moreover, a distinct tremor phase with a broader frequency content is clear on the spectrogram at station HVO on July 9th. The time of this phase correlates with the surface water flooding and this station is located very close to the river that flooded.

We computed amplitude spectra of the tremor signal over one-hour intervals. The spectra are characterised by a wide range of frequencies between 0.8 and 10 Hz. A number of peaks can be identified in the spectra, not representing overtones of a fundamental frequency, as is characteristic of harmonic tremor. We selected three frequency bands (Fig. 10) for further analysis of tremor location and amplitude:

- 0.8-1.5 Hz: This frequency range dominates the amplitude spectra in the beginning and ending hours of the tremor;
- 1.5-4 Hz: Dominant when the tremor is strongest and short bursts of tremor are recorded;
- 4-9 Hz: Lower in amplitude and not seen at some stations (e.g. ENT, ESK, SLY).

Although the overall pattern is similar at all stations, there are some exceptions. Station ENT has significantly less high-frequency content (4-9 Hz) proportionately compared to most other stations. Station ALF has a relatively even distribution of amplitude over all frequencies (0.8-10 Hz) with peaks in the amplitude spectra that can be recognized as horizontal bands in the spectrogram of Fig. 9. These features are in general similar to what is observed for the seismic events: Higher frequencies appear to be attenuated at the caldera stations, in particular at ENT, compared to station ALF.

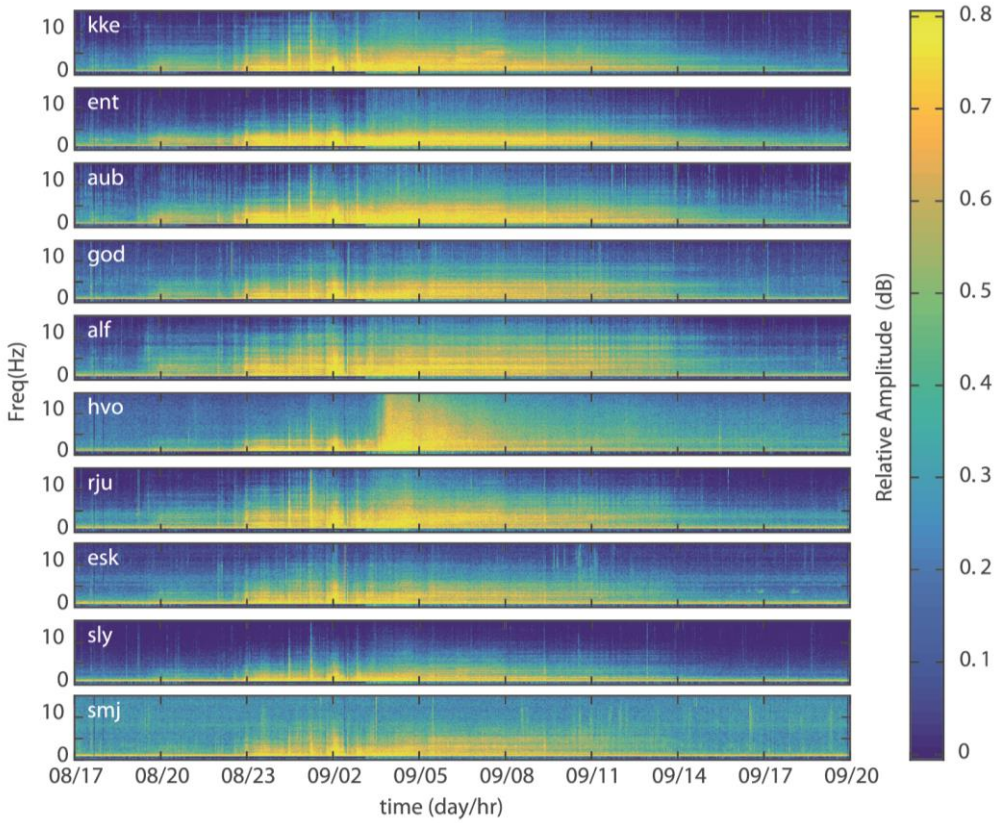

Fig. 9. Spectrograms of the Z component of motion at all stations. The signal was pre-filtered between 0.5-15 Hz. The colour scale shows the logarithmic relative amplitude (dB) individually normalised by maximum at each station. The stations are ordered from top to bottom by decreasing values of total rms amplitude in the frequency range 0.5-9 Hz. The amplitude spectra used to compose the spectrograms have been computed over consecutive, 8192 samples long, windows (sampling rate is 100 Hz), with 80% overlap. Vertical lines that appear locally at some stations may be earthquakes that were not identified when removing transients from the signal.

The globally normalised spectra in Fig. 10 show clearly the hours when the tremor was strongest. This occurred in general between 23:00 on July 8th and 05:00 on July 9th, with the hours of tremor between 02:00 and 03:00 on July 9th dominating at all stations except for HVO. At this station, the tremor was strongest at 04:00 on July 9th, coinciding with the time of the glacial flood. Compared to the rest of the tremor, the amplitude spectrum of this different tremor phase at HVO is flatter, with power distributed more evenly over the frequency range 2 - >15 Hz. Less energy is present below 2 Hz. The width of the frequency range is greatest at the onset of this tremor phase (0.8 - >10 Hz) and then reduces gradually towards the end, around 4 hours later (Fig. 9). This coincides with decreasing amplitude as well.

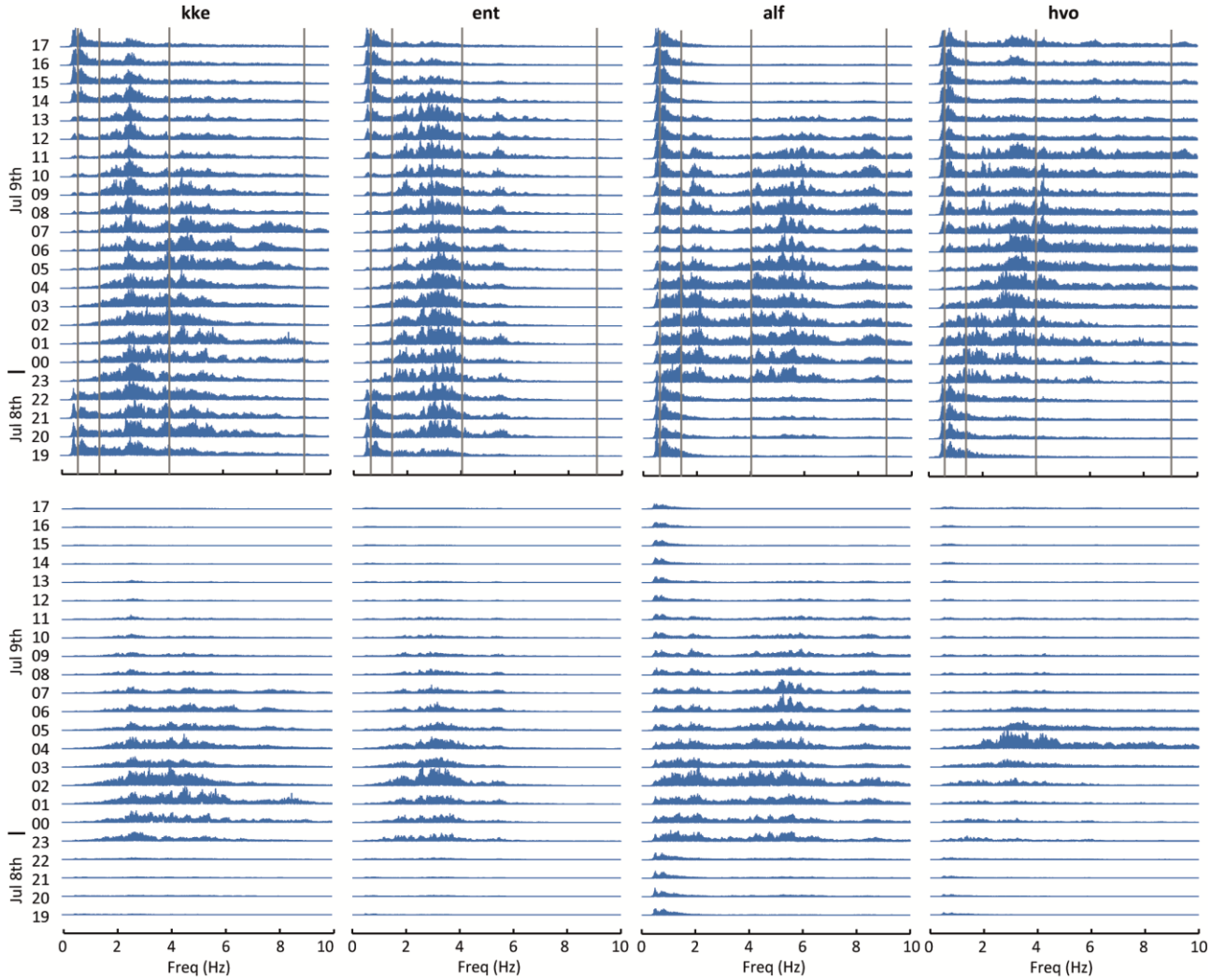

Fig. 10 Hourly amplitude spectra at some stations. Top: hourly traces individually normalised. Grey lines separate the three frequency bands. Bottom: hourly traces globally normalised for each station (all 23 hours).

6.3 Power time-history

In order to obtain better insight into the amplitude history of the signal at different stations, we performed a LSQ (least-squares) fit of the power time-function at each station. We aimed at identifying different components of the signal, possibly reflecting different phenomena (for example different sources).

We first computed, for each station, the integral power of the signal over 8 minute windows, sliding with 1 minute steps, between 05:00 GMT on July 8th (around 2 hours before the onset of the tremor) and 20:00 GMT on July 9th (around 2 hours after the end). We used the 2 hours before and after the tremor to evaluate the background power, which was then subtracted from the tremor power as a linear trend interpolated between the beginning and end (Fig. 11). As this led occasionally to negative power at the low amplitude stations at the

beginning and end of the signal, we chose to use only 18 central hours of tremor for further analysis, as indicated in Fig. 11. As is evident from Fig. 11, the time history of the tremor has very similar features at all the stations, while the overall amplitude is quite varied. We have fitted a simple model to the tremor in order to enhance any variations.

At each station, the 3 spatial components of the 18 extracted hours have been combined into a total power (vector amplitude squared). Then a simple model was fitted to the data, parameterized as:

$$F_{ij} = a_i \cdot f_j \qquad [1]$$

where F_{ij} is the power time-function at station i, with j indexing time, the function f_j represents an average pattern at all stations, scaled by a station coefficient, a_i. This is solved through a LSQ fit which is performed in 10 minute intervals throughout the 18 hours. This fitting involves an ambiguity where an arbitrary scaling factor can scale f_j relative to all the a_i. Thus, the method extracts relative amplitude information between stations. It is clear from Fig. 11 that most of the relative variation in amplitude occurs at station KKE. So we used this station as reference and normalised all stations' coefficients by the KKE coefficients (Fig. 12b). KKE coefficients were instead normalised by the mean of the other stations' coefficients, in each time interval (Fig. 12a). We repeated this process for each of the three different frequency bands mentioned above: 0.8-1.5 Hz, 1.5-4 Hz and 4-9 Hz.

All results, for all stations and all frequency bands, are reported in the Supplementary Material (Appendix A) and Figs. 11-12 show some examples. Some general features are:

- The onset of the tremor is clear at about 19:15 on July 8th and the end is gradual, with the tremor disappearing into background noise at 18:00 the following day (Fig. 11).
- Overall, the amplitude time-history is similar at all stations, except for a scaling factor (Fig 11), and the coefficient plots are stable for most of the duration of the tremor, except for occasional peaks (Fig. 12).
- 3 main strong tremor bursts, lasting 6 to 10 minutes, occurred at around 00:30, 01.20 and 03:00 and are observed at all stations. They are dominated in terms of power at station KKE in all frequency bands, as shown clearly by the KKE coefficients (Fig. 12a).
- Another longer (40 min) burst occurred at around 01:55, recorded by all stations. This is not dominated by a particular station, as there is no corresponding peak in any of the relative coefficients plots (Fig. 12 and Supplementary Material).
- Station ENT has much less power than the other stations in the highest frequency band compared to the lower two bands (Supplementary Material).

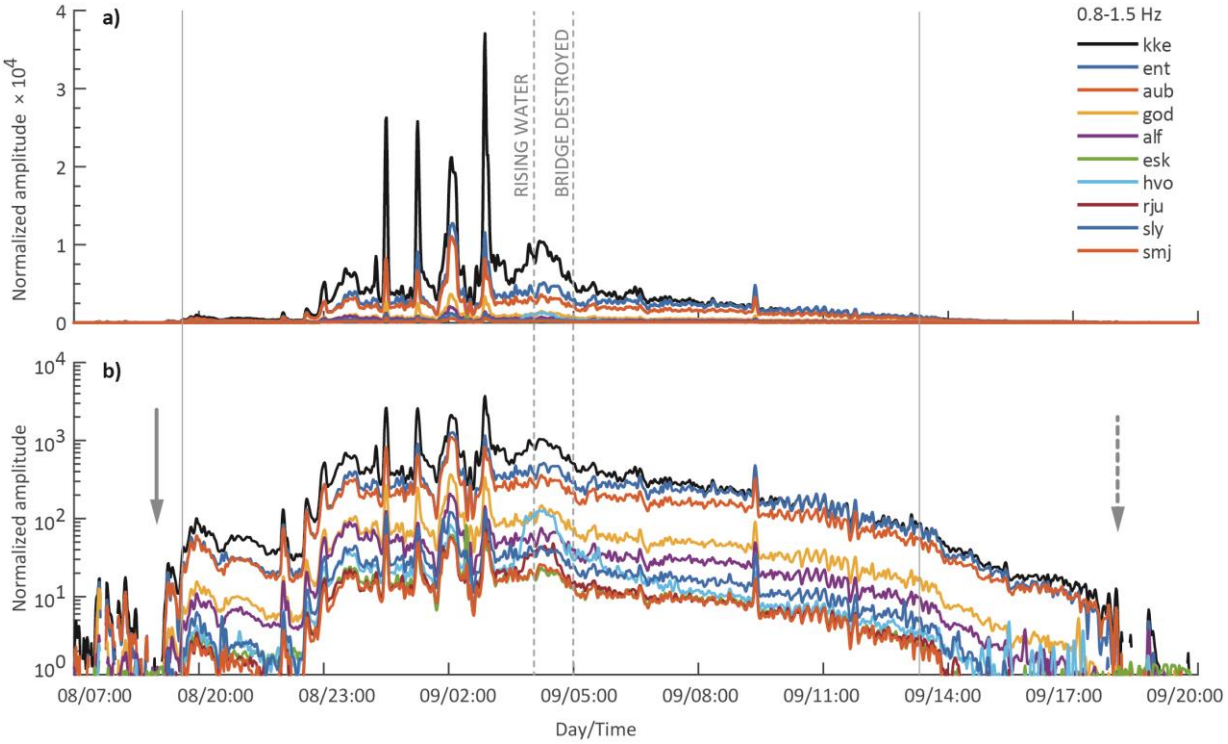

Fig. 11. a) Integral amplitude spectral density over the low-frequency band (0.8-1.5 Hz) at all stations as a function of time. b) The same plotted on a logarithmic scale. In both cases the background power has been subtracted and the amplitude normalised by the average background at station KKE. The solid arrow indicates the onset of the tremor. The dashed arrow indicates approximately the time when tremor disappears into noise. The vertical dashed lines indicate the time when rising water was observed at Léreftshöfuð gauging station (04:00) and the time when the bridge over Múlakvísl river was destroyed (05:00). Around 03:30 an anomalous tremor phase appears at station HVO. The solid lines indicate the time interval used for the LSQ fit (same as Fig. 12).

- At 03.30, a different tremor phase dominates clearly at HVO (Fig. 12b) in all frequency bands (especially the highest) and is vaguely seen at RJU in the lowest frequency range (Supplementary Material). The shape of the burst is different compared to the other short bursts described before, with a sharp increase in amplitude at the beginning, and gradual decrease in the following hours, as opposed to a sharp onset and a sharp end of the others (Figs. 11 and 12). In the medium and high frequency range, the coefficient curve at HVO appears to have a sharp peak starting at 03:30, decaying for about 3 hours and then rising up again reaching a new peak around 12:00. This second increase in amplitude is due to the seismicity that occurred locally near HVO, mentioned above in Section 5.

In addition, there are some other minor features, e.g. some other bursts with varying amplitude ratios between stations. Most of them are related to small local earthquakes which we have not managed to remove from the data.

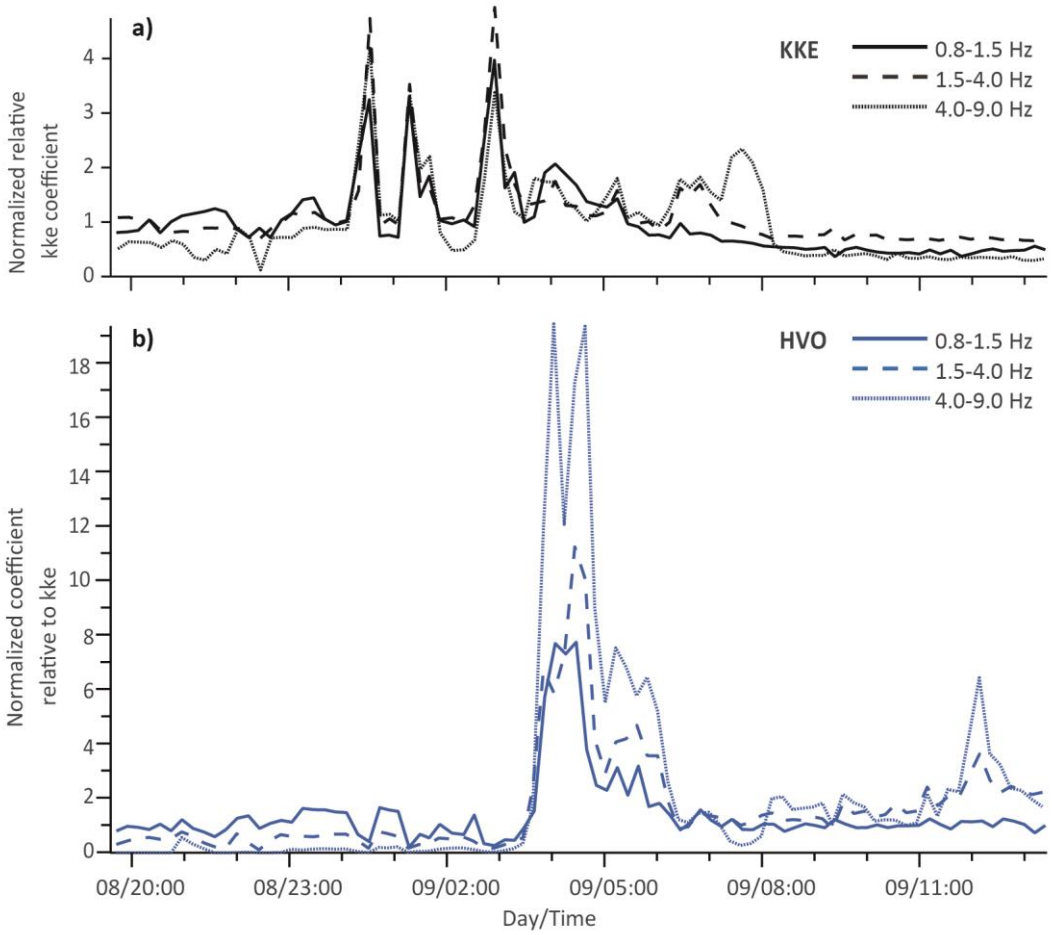

Fig. 12. Station coefficients obtained with LSQ fit of the power time-history over 10 minute intervals. a) KKE coefficients, normalised by the mean of all other stations' coefficients, in each time interval. b) HVO coefficients, normalised by KKE coefficients. Results are shown for all three frequency bands analysed.

6.4 Amplitude-distance decay

The amplitude decay with distance was analysed in the 3 main frequency bands identified above and by assuming a source location consistent with the southern cauldrons, most of the earthquake activity, and the main tremor source location obtained from cross-correlation, shown in the next section. The tremor amplitude was estimated as rms value of the amplitude time-history shown in Fig. 11, over the 23 hours of tremor. The small differences of station elevation are not taken into account in the distance calculation. The amplitude pattern with distance is not simple, especially at the caldera stations, and varies with frequency (blue lines in Fig. 13). In the two lower frequency bands, the relative amplitudes at stations AUB and ENT increase with distance. At higher frequency, instead, the signal amplitude at ENT drops significantly compared to all other stations and the

amplitude decay with distance has a simpler pattern. This non-monotonic pattern is not consistent with both a confined location and simple distance decay.

The overall pattern is, however, stable with time and for this reason we only show the rms amplitude – distance function for the whole tremor signal (23 hours) in Fig. 13. In order to evaluate whether this pattern may be influenced by site effects, we computed the horizontal to vertical spectral ratio (H/V) at each seismic station. We did not find any clear correlation between the H/V functions and the amplitude pattern, which appears similar for all three spatial component of motion. Therefore, we present the three components combined together. Similar complexities to those of the tremor are observed also in the amplitude-distance decay of the two example events shown above in Figs. 6-7 (grey lines in Fig. 13). The peak amplitude is used as a measure of signal amplitude for these events.

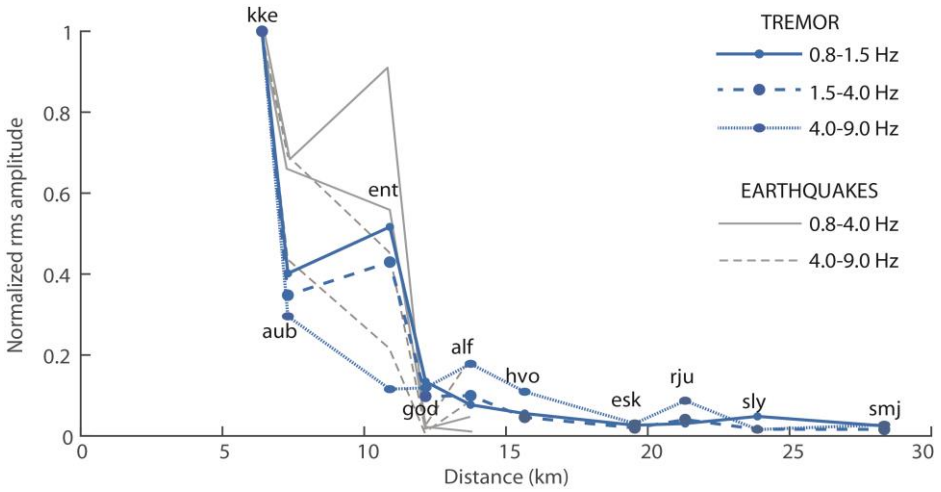

Fig.13 In blue amplitude decay with distance of the tremor for all stations in the three frequency bands, assuming the source is located at the point of highest energy in Fig. 15. Rms amplitude over 23 hours, combined for the 3 components of motion. In grey the amplitude decay with distance of the two seismic events of Figs. 6-7 for the 5 closest stations, for two frequency bands, computed as maximum amplitude combining the 3 components of motion.

7. Tremor source(s) localization

As the amplitude pattern is not simple, especially at the caldera stations, we only used the phase information of the signals in order to locate the tremor source. We used two cross-correlation methods, using a grid-search for locating the source that best predicts the energy of correlograms. These are 2-dimensional methods that assume the source is located at the surface and that the tremor has a strong surface wave component, propagating at constant velocity. In many cases the tremor wavefield has been shown to consist of Rayleigh and Love

waves, e.g. at Kilauea (Ferrazzini et al, 1991) and at Mt. Etna (Ereditato and Luongo, 1994; Wegler and Seidl, 1997). Li et al. (2015) have shown with synthetic tests that it is not necessary that the tremor be dominated by surface waves for this approach to work. Body waves of the same order of magnitude in amplitude as surface waves disturb the measure but do not correlate in a 2D geometry with surface wave velocities. They represent noise that is suppressed because it doesn't correlate. It is therefore sufficient that a significant part of the wavefield consists of surface waves.

In order to reduce the effect of transients in the signal, we processed the tremor using a 1 bit normalization (Bensen et al., 2007). This proved to work better than clipping or manually removing earthquakes from the tremorgrams, more effectively focusing the energy of the source, reducing the influence of the nearby stations, which otherwise dominate in terms of amplitude with respect to all other stations.

We applied both methods to the lowest frequency band (0.8-1.5) because at higher frequency it is more difficult to obtain stable results and the low frequencies are less likely to be affected by scattering effects.

7.1 Single-correlation method

This method is based on the back-projection of the cross-correlation envelopes, computed for all 45 station pairs (Shapiro et al., 2006; Guðmundsson & Brandsdóttir, 2010; Ballmer et al., 2013; Droznin et al., 2015). A grid of hypothetical source points in the surface is defined and an average velocity is chosen. For each point, the expected time lag for a given station pair is calculated. The value corresponding to this time difference is then fetched from the envelope of the cross-correlation function. The results from all station pairs are then stacked for each point of the grid, resulting in a map of the stacked, back projected correlation envelopes. This can be taken as a proxy for the energy distribution of the source, but is of course affected by the frequency and its band width, the velocity and its variation, other signals in the tremor than those that propagate horizontally, including noise, and an unknown or arbitrary amplitude scaling with distance. Li et al. (2015) addressed these issues by synthetic testing. Several different velocities have been tested and the one that best focuses the energy was chosen. This velocity (1.2 km/s) is slightly lower than Rayleigh-wave group velocities measured at 0.5-1 Hz at Hekla (Haney et al., 2011) and at Katla and nearby Eyjafjallajökull (Z. Jeddi and Á. Benediktsdóttir, personal communication).

7.2 Double-correlation method

In this case, station triplets are used instead of pairs. One of the stations in each triplet is chosen as reference. The other two are correlated with the reference and the resulting two correlograms are correlated with each other. The resulting function is then back-projected in the same way as in the single-correlation method, but in this case for 360 station triplets. This method increases the amount of independent correlation information from 45 to 360. In this case, the result has the unit of energy squared, therefore, the square root of the stack is taken in order to map energy. This method is similar to the one proposed by Li et al. (2015), except that they use higher-order stacks of envelopes rather than higher order correlation. The details of the method are explained in the Supplementary Material (Appendix B).

7.3 Cross-correlation functions

The cross-correlation functions for all station pairs have been computed over one hour records (Fig. 14). The pattern of correlation is complex. If the source was truly diffuse, and the wavefield dominated by surface waves, we would expect two symmetric wave packets at opposite time shifts, corresponding to intra-station surface waves. This is not the case. If the source area was geographically small and there was no multipathing, we would expect to see an isolated wave packet at a time corresponding to the difference in distance of the two stations from the source divided by an average wave velocity. Instead, several wave packages can be identified in the cross-correlation functions, distributed over a wide range of time shifts, not symmetric. The correlation functions are also not stable with time, in particular between 11:00 on July 8th and 04:00 on July 9th, when the tremor is strongest. During this period, a number of wave packages can be identified in all cross-correlation functions distributed over time shifts of several tens of seconds. After this unstable period, the functions become much more stable until the end of the tremor, with few wave packages dispersed over 10-15 seconds. Auto-correlations of tremor at individual stations do not suggest significant source correlation on these time scales. The wide time dispersal cannot be explained by direct propagating waves from a single point source only. Higher-order scattering effects must be invoked. Multiple wave packages at smaller time shift may be caused by a distributed source or multiple sources.

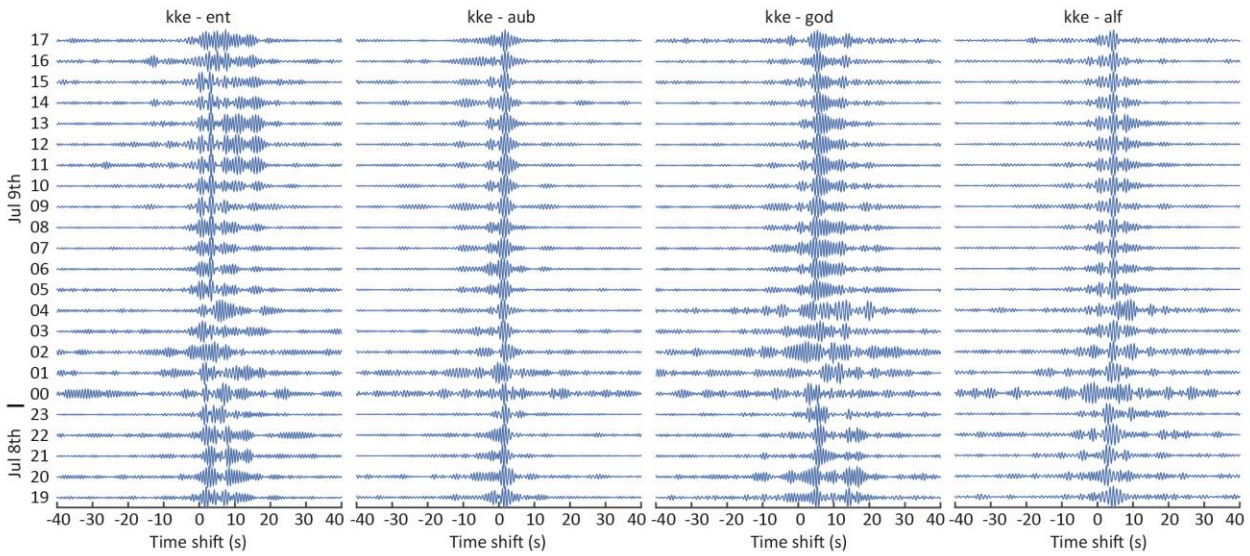

Fig.14 Examples of hourly cross-correlation functions for four station pairs. Several wave packages can be identified, dispersed over wide ranges of time shift. Temporal variations of the tremor can also be noticed. An unstable period between 00:00 and 05:00 is followed by a more stable period until the end of the tremor.

7.4 Tremor location results

The source distribution of energy obtained with the single- and double-correlation methods for the whole tremor signal is shown in Fig. 15. We tested a range of velocities between 1 and 2.5 km/s and chose 1.2 km/s as the velocity that best focused the energy.

Both methods result in a similar source location in the south-eastern caldera. This is consistent with the location of the earthquakes that occurred during the tremor and with the locations of active ice cauldrons. A part of the energy is noticeably distributed along the hyperbolae corresponding to constant time shifts for the 3 caldera stations' (KKE, ENT and AUB) pairs. This is expected, as they are the three closest stations to the source and dominate not only in terms of signal amplitude, but also in terms of coherency. The one-bit normalization equalizes the amplitudes of the individual correlograms, which vary considerably in this case as distances vary from a few km to about 25 km. This focuses the back-projected energy map and reduces streaking amplitude bands on the periphery of the map in our case. However, we cannot claim this amplitude scaling, or effectively weighting, of the data is optimal, because we do not know the signal-to-noise ratio of the data. Therefore, this pre-processing step may not be beneficial in all cases. In addition, the double-correlation technique significantly focuses the energy on the source with respect to the single correlation. This reflects the ability of higher-order correlations to better suppress the noise.

The width of the maximum energy peak is affected by several factors: The finite width of the frequency band used, the uncertainty of velocity, the size of the source.

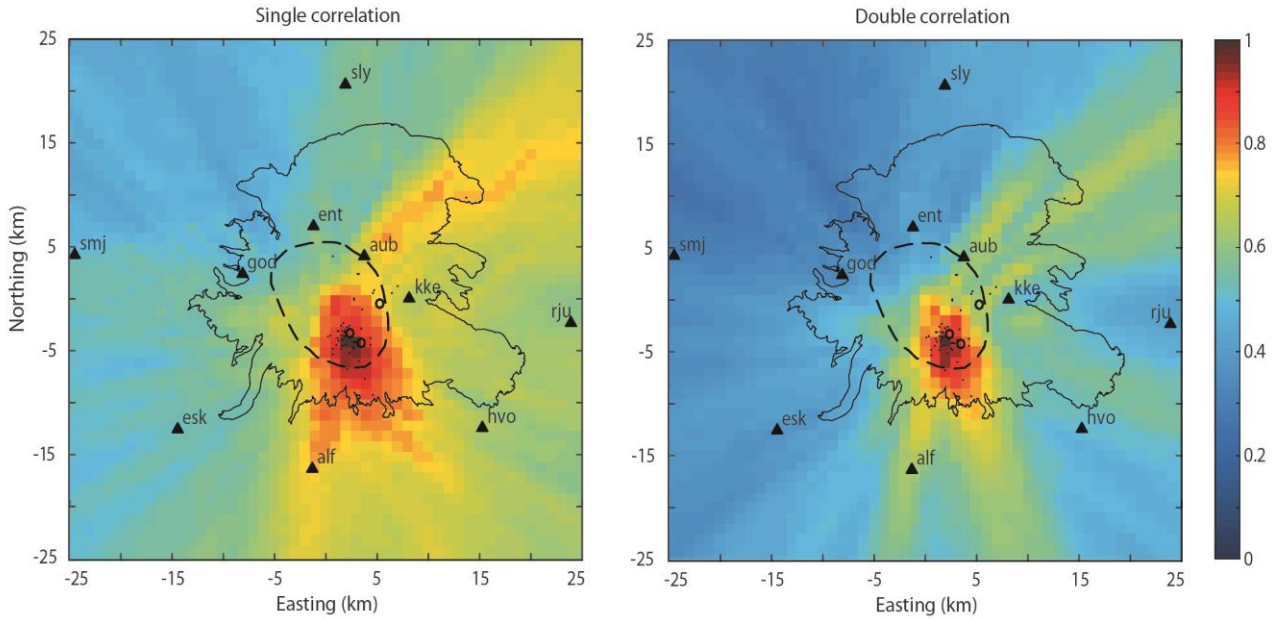

Fig. 15. Location results from single- and double-correlation methods, obtained for the whole tremor signal, with velocity 1.2 km/s. The colours define normalised energy, dark red for maximum energy. Black dots: earthquakes recorded during the tremor. Black solid line: glacier. Black dashed line: caldera outline. Black triangles: seismic stations. Black circles: active cauldrons.

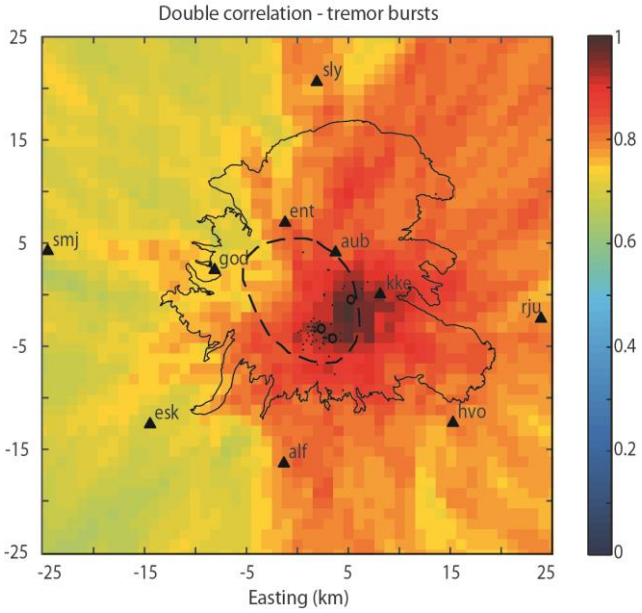

Fig. 16. Location results with double-correlation method, obtained for only the short tremor bursts, stacked. Otherwise, same as for Fig.15

As there are three clear short tremor bursts that showed a distinct behaviour in the relative amplitude, we isolated them and located them separately from the rest of the tremor. For this we used the double-correlation method, applied to each 6-min burst. We then stacked

the three energy-maps to better suppress noise. By doing this, we assume that the three bursts were generated at the same location. This is justified by the relative amplitude behaviour, where all three peaks have the same pattern, different from the average pattern at other times, suggesting a similar source location. The result is shown in Fig. 16: although the energy is not as focused as in the case of the whole 23 hour signal, a peak of energy is located to the north-east of the main tremor source located in the south-eastern caldera. This correlates with the north-eastern active cauldron and with the evidence described in the previous section that the power related to these peaks is dominated by station KKE, which is located very close to this cauldron.

It was not possible to locate the tremor component generated by the flood, for several reasons: i) its presumed location is peripheral to the network, ii) it is observed mainly at one station and weakly at a few other stations, while at most stations it is hidden in the main tremor , iii) the source may not be stable in space.

8. Discussion

8.1 Volcanic/hydrothermal tremor and flood tremor components

Most of the tremor signal appears to be generated at a stable source located in the south-eastern part of the caldera, consistent with the two southern active cauldrons and with the earthquake activity. This component of the tremor likely corresponds to the stable portion of the relative amplitudes at various stations (Fig. 13 and Supplementary Material). This suggests that there is a main source of tremor which was stable in space and time, although varying in frequency content and power, probably in association with changes in the source mechanism. This source might have been spatially distributed, based on the width of the peak of energy obtained from back-projection of the cross-correlation functions (Fig.15). However, part of this width is due to uncertainty and a part due to the finite width of the frequency band used. We are not able to estimate the uncertainty rigorously, but the average half width of the distribution in Fig. 15b is about 3 km.

In addition to this main source, another component of the tremor was identified with the LSQ fit of the tremor power, corresponding to the three short tremor bursts, dominated in amplitude by station KKE (Fig. 13a). This component has a similar amplitude pattern in all frequency bands analysed. The location results obtained with back-projection of the double-correlation envelopes highlighted a peak of energy correlating in space with the northern active ice cauldron, located close to station KKE (Fig. 16). We therefore suggest that another

source of tremor, located closer to KKE, was either intermittently activated, or intermittently exceeded the main source's power.

A third distinct tremor phase is primarily seen at station HVO (Fig. 13b), the station closest to Múlakvísl river. This phase correlates in time and space with the water flood and therefore appears to be directly related to the water draining from Kötlujökull glacier.

The evidence of a stable tremor phase, both in time and space, located near active cauldrons and clearly separated from a tremor phase associated with the flood, suggests that most of the tremor was generated by volcanic or hydrothermal processes occurring at the location of the active cauldrons. This is also supported by the increased earthquake activity in the same location and by the water accumulation under the glacier that started months before the tremor, which is explained by increased geothermal activity (Guðmundsson et al., 2013). In addition, the power of volcanic tremor is often concentrated in the band between 0.5-7 Hz (Konstantinou and Schlindwein, 2002), which is consistent with our observations. The same applies to the source located in the eastern sector of the caldera, corresponding to the short tremor bursts. Here the source appears less stable in terms of amplitude history, but stable in space, allowing us to crudely estimate a location that corresponds to the eastern active cauldron.

The two different types of tremor source suggested (flood-related and volcano-related) may be reflected also in different amplitude and frequency features of the signal, summarised here:

- the flood tremor spans a wider frequency range, with energy up to >15 Hz, while the volcanic tremor has energy up to 9-10 Hz;
- the frequency content of the flood tremor is flatter, with most of the energy evenly distributed over a wide range (2-10 Hz), while the hydrothermal/volcanic tremor is mainly concentrated between 0.8 and 4 Hz;
- the flood tremor has the widest frequency range in the beginning and gradually loses high frequencies as the signal decays in amplitude, while the volcanic tremor has a more stable frequency distribution through time, which does not correlate with changing signal amplitude;
- the flood tremor begins with large amplitude which monotonically decays with time over a few hours, while the volcanic tremor has a more complex amplitude history.

8.2 Interpretation of the volcanic/hydrothermal source

Possible interpretations of the source generating the tremor located at the active ice cauldrons are either a subglacial magmatic eruption or a hydrothermal process, such as

hydrothermal boiling, eventually involving explosive events. We have insufficient evidence to distinguish whether or not a minor subglacial eruption occurred. Certainly, an increase in geothermal heat release has occurred, starting about one year before the tremor episode (when water accumulation started under the glacier) and a subglacial eruption is not an unlikely scenario, considering that the event was also accompanied by greatly increased seismicity inside the caldera.

The 2011 unrest was similar to the event that occurred in 1999, that some authors interpreted as a subglacial eruption (e.g. Guðmundsson et al., 2007). For the 1999 event, the arguments to support the hypothesis of an eruption are that the heat exchange that led to the formation of the melt water occurred very rapidly (few hours or days) and that there was no appreciable geothermal heating at the same site in the following years (Guðmundsson et al., 2007). This is different from what happened in July 2011, as in this case geothermal activity was observed for years before 2011 and still persists. However, this does not exclude that, if in 1999 a subglacial eruption took place, a similar episode occurred in 2011. Although in both cases increased seismicity was observed, neither of the two unrest episodes showed clear seismic indications of magma rising. In addition, geochemical studies of the flood water from the 2011 jökulhlaup did not find evidence for floodwater having come into contact with magma (Galeczka et al., 2014).

Another possible scenario is that the tremor was generated by hydrothermal processes. For example, hydrothermal boiling generating tremor may have been induced by the pressure drop that occurred when the water level in the subglacial lakes dropped as a consequence of water release from the cauldrons. The tremor started at 19:00 on July 8th and the flood waters reached the gauging station at Léreftshöfuð 9 hours later, at 04:00 on July 9th. It is difficult to evaluate how long it may have taken for the water to flow from the cauldrons to the gauging station, as this strongly depends on the unknown subglacial water drainage system and topography. As a reference, we used two known jökulhlaups which occurred at Eyjafjallajökull in 2010 and Gjálp in 1996. The first occurred during the 2010 Eyjafjallajökull eruption and took about 5 hours to reach a proglacial lake around 5 km away from the crater, down a steep slope (Magnússon et al., 2012). During the Gjálp eruption, instead, the flood took approximately 10 hours to travel about 50 km on a more gentle slope (Einarsson et al., 1997). The difference between these two cases may depend on the time of the year when the eruption occurred, influencing the subglacial drainage system. While the Eyjafjallajökull eruption occurred at the end of the winter, when the drainage system is inefficient, the Gjálp eruption occurred at the end of the summer when the system is fully developed (Magnússon et al., 2012). The unrest at Katla occurred in early summer and the distance between the cauldrons

and the Léreftshöfuð gauging station is around 20 km. The steepness of the slope is intermediate between the two reference cases. Using the two examples as extremes, the Katla flood might have taken between 4 to 20 hours to reach the gauging station at Léreftshöfuð. This suggests that it is plausible that hydrothermal boiling, generating tremor, was initiated when water was released from the active cauldrons, reaching the first gauging station 9 hours later. This interpretation, however, does not clearly explain the increased earthquake activity that started some days before, on July 6th, inside the caldera and the new seismic cluster on the south flank (Sgattoni et al., 2015).

The tremor signal is highly variable in amplitude. Tremor amplitude variations at other volcanoes have in many cases coincided with visual observations of varying strength of volcanic/hydrothermal activity (e.g. lava fountaining or dome building), as for example at Kilauea (Dvorak and Okamura, 1985) and Hekla (Brandsdóttir and Einarsson, 1992). However, this is not always the case and sometimes no relationship between surficial activity and amplitude has been identified. This has been interpreted as a consequence of variation of magma flow rate at depths in the crust, e.g. at Kilauea (Ferrazzini and Aki, 1992). In the case of Katla's tremor, the short tremor bursts, which seem to be located at a different site compared to the main tremor source, appear to be the strongest in terms of power and occur with a sharp onset and sharp end. If the source was hydrothermal, this might be explained with local, more powerful hydrothermal explosions or flash-boiling. The possibility to generate hydrothermal explosions depends on local conditions such as permeability. A local low-permeability layer, for example, could induce a build-up of pressure, suddenly released into steam flashing (Morgan et al., 2009). The conditions for this to happen may have occurred only at the site of the northern tremor source, explaining the higher amplitude bursts generated there. If the tremor source was an eruption, the amplitude variations may be explained with eruption phases of varying strength.

8.3. Considerations about path effects and location method

The frequency-dependent, complex pattern of amplitude decay with distance, not following any clear amplitude-distance decay law, suggests that source radiation and/or propagation effects are anisotropic. A similar pattern is seen also for the earthquakes. Site effects may play an additional role, but no clear correlation was identified between H/V spectral ratios and the amplitude distribution at the different stations. Also, the amplitude pattern is similar for all components of motion, which may indicate that site effects do not play the main role. However, the H/V spectral ratio method is motivated to detect amplification due to resonance in a stratified structure. The caldera stations were all deployed

on nunataks in the ice, on sharp bedrock peaks protruding the ice sheet. The elastic properties of ice are rock-like, but its density is much less than that of rock. The potential amplification effects of such topographic features are poorly understood. We, nevertheless, suggest that path effects and/or an anisotropic radiation pattern are the main responsible factors for the complex amplitude patterns observed. In addition, there is clear indication of strong propagation effects, within the caldera, suggested by the strong attenuation of high frequencies at stations receiving seismic ways travelling through the caldera region, for both tremor and earthquakes. The complexity of the cross-correlation functions is also indicative of strong scattering effects, generating several, broad wave packages in the correlation functions. The interaction of seismic waves with the subglacial topography and the ice, together with the crustal heterogeneities, may be responsible for strong path effects.

The complex amplitude pattern made the use of amplitude-based tremor location methods impossible. However, by using the signal phase through cross-correlation methods, we were able to confidently locate two tremor sources (for the lowest frequency component of the tremor), in locations that are consistent with other seismic and hydrological observations. The double-correlation method allowed us to significantly focus the tremor source location compared to the single-correlation method. Higher order correlation methods therefore appear to be a promising tool to improve the resolution of volcanic tremor location.

9. Conclusions

We have analysed the 23 hour tremor signal and earthquake activity associated with an unrest episode that occurred at the subglacial volcano Katla in July 2011. During the unrest, three ice cauldrons deepened on the glacier and a glacial flood caused damage to infrastructure, but no visible eruption broke the ice surface. Three different tremor components were identified based on amplitude and frequency features. We have described them in detail and discussed their possible source process by using additional hydrological observations and comparison to other case studies. Back-projection of single and double cross-correlation envelopes was used to locate the two spatially stable components of the tremor.

The main conclusions of this work are:

- Increased earthquake activity, characterised by low-frequency, hybrid and high-frequency events, started inside the Katla caldera a few days before the tremor burst and lasted for months afterwards;
- The tremor signal can be separated into three main phases. Two of them were traced to the active ice cauldrons and are interpreted to be caused by hydrothermal or volcanic

processes. The third, mainly observed at the station closest to the river that flooded, is associated with the glacial flood;

- Because of the highly increased seismicity, evidence of rapid melting of the glacier and similarity to the 1999 event that was interpreted as a subglacial eruption, the 2011 tremor may have been caused by a minor subglacial eruption;
- It is also plausible that the tremor was generated by hydrothermal processes with no magma involved: boiling and/or explosions may have been triggered in the hydrothermal system when the flood started to flow out of the subglacial geothermal systems;
- All interpretations require an increase of heat released by the volcano that led to water accumulation before the tremor. This may be due to heat introduced into the shallow crust by a magmatic process or enhanced permeability in the geothermal areas due to tectonic activity;
- The double cross-correlation method used to locate the lowest-frequency tremor sources significantly improved the resolution of the source energy distribution, compared to the single correlation. Higher order correlation methods appear to be a promising tool to further improve the resolution of tremor-source location;
- The complex amplitude-decay with distance precluded the use of amplitude information to locate the tremor source and suggests the presence of strong path effects on waves travelling through the caldera region. This is corroborated by strong attenuation of high frequencies along trans-caldera paths.

References

Ballmer, S., Wolfe, C.J., Okubo, P.G., Haney, M.M., Thurber, C.H., 2013. Ambient seismic noise interferometry in Hawai'i reveals long-range observability of volcanic tremor. Geophys. J. Int. 194, 512–523. doi:10.1093/gji/ggt112

Baptie, B., Luckett, R., Neuberg, J., 2002. Observations of low-frequency earthquakes and volcanic tremor at Soufrière Hills Volcano, Montserrat. Geological Society, London, Memoirs. 21, 611-620. doi:10.1144/GSL.MEM.2002.021.01.30

Battaglia, J., Aki, K., 2003. Location of seismic events and eruptive fissures on the Piton de la Fournaise volcano using seismic amplitudes. J. Geophys. Res. 108 (B8).

Benoit, J.P., McNutt, S.R., 1997. New constraints on source processes of volcanic tremor at Arenal Volcano, Costa Rica, using broadband seismic data. Geophys. Res. Lett. 24, 449–452. doi:10.1029/97GL00179

Bensen, G.D., Ritzwoller, M.H., Barmin, M.P., Levshin, a. L., Lin, F., Moschetti, M.P., Shapiro, N.M., Yang, Y., 2007. Processing seismic ambient noise data to obtain reliable broad-band surface wave dispersion measurements. Geophys. J. Int. 169, 1239–1260. doi:10.1111/j.1365-246X.2007.03374.x

Björnsson, H., Pálsson, F., Guðmundsson, M.T., 2000. Surface and bedrock topography of the Mýrdalsjökull ice cap. Jökull 49, 29–46.

Brandsdóttir, B., Einarsson, P., 1992. Volcanic tremor and low-frequency earthquakes in Iceland. In: Gasparini, P., Scarpa, R., Aki, K. (Eds.), Volcanic Seismology. IAVCEI Proc. Volcanol. 3, 212-222.

Budd, D.A., Troll., V.R., Dahren, B., Burchardt, S., 2014. Persistent shallow magma storage beneath Katla Volcano. Paper presented at: Goldschmidt Annual Meeting, Sacramento, USA.

Böðvarsson, R., Rögnvaldsson,S. T., Slunga, R., Kjartansson, E, 1998. The SIL Data Acquisition System — At Present and Beyond Year 2000 (Report VI´-R98005-JA04,Icelandic Meteorological Office)

Chouet, B., 1992. A Seismic Model for the Source of Long-Period Events and Harmonic Tremor, in: Gasparini, P., Scarpa, R., Aki, K. (Eds.), Volcanic Seismology SE - 11, IAVCEI Proceedings in Volcanology. Springer Berlin Heidelberg, pp. 133–156. doi:10.1007/978-3-642-77008-1_11

Chouet, B.A., 1996. Long-period volcano seismicity: its source and use in eruption forecasting. Nature. doi:10.1038/380309a0

Chouet. B.A., 2003. Volcano Seismology. Pure appl. geophys. 160, 739-788.

Di Grazia, G., Falsaperla, S., Langer, H., 2006. Volcanic tremor location during the 2004 Mount Etna lava effusion. Geophys. Res. Lett. 33, L04304. doi:10.1029/2005GL025177

Dmitrieva, K., Hotovec-Ellis, A.J., Prejean, S., Dunham, E.M., 2013. Frictional-faulting model for harmonic tremor before Redoubt Volcano eruptions. Nat. Geosci 6, 652–656.

Droznin, D.V., Shapiro, N.M., Droznina, S.Y., Senyukov, S.L., Chebrov, V.N., Gordeev, E.I., 2015. Detecting and locating volcanic tremors on the Klyuchevskoy group of volcanoes (Kamchatka) based on correlations of continuous seismic records. Geophys. J. Int. 203 , 1001–1010. doi:10.1093/gji/ggv342

Dvorak, J.J., Okamura, A.T., 1985. Variations in tilt rate and harmonic tremor amplitude during the January-August 1983 East Rift eruptions of Kilauea volcano, Hawaii. J. Volcanol. Geotherm. Res. 25, 249-258.

Eggertsson S., 1919. Ymislegt smavegis vidvıkjandi Kotlugosinu 1918. Eimreidin 25, 212–222.

Einarsson, P., 1991. Earthquakes and present-day tectonism in Iceland. Tectonophysics 189, 261–279.

Einarsson, P., Brandsdóttir, B., 2000. Earthquakes in the Myrdalsjokull area , Iceland , 1978-1985: Seasonal correlation and connection with volcanoes 1978–1985.

Einarsson, P., Brandsdóttir, B., Guðmundsson, M.T., Björnsson, H., Grínvold, K., Sigmundsson, F., 1997. Center of the Iceland hotspot experiences volcanic unrest. Eos, Trans. Am. Geophys. Union 78, 369. doi:10.1029/97EO00237

Einarsson, P., Hjartardóttir, Á. R., 2015. Structure and tectonic position of the Eyjafjallajökull volcano, S-Iceland. Jökull 65, 1-15.

Einarsson, P., Sæmundsson, K., 1987. Earthquake epicenters 1982-1985 and volcanic systems in Iceland. In Þ.I.Sigfússon, ed. *Í hlutarins eðli*, Festschrift for Þorbjörn Sigurgeirsson. Menningarsjóður, Reykjavík (map).

Ereditato, D., Luongo, G., 1994. Volcanic tremor wavefield during quiescent and eruptive activity at Mt. Etna (Sicily). J. Volcanol. Geotherm. Res. 61, 239-251.

Fehler, M.C., 1983. Observations of volcanic tremor at Mt. St. Helens volcano. J. Geophys. Res. 88, 3476-3484.

Ferrazzini, V., Aki, K., 1992. Preliminary results from a field experiment on volcanic events at Kilauea using an array of digital seismographs. In: Gasparini, P., Scarpa, R., Aki, K. (Eds.), Volcanic Seismology. IAVCEI Proc. Volcanol. 3, 168-189.

Ferrazzini, V., Aki, K., Chouet, B., 1991. Characteristics of seismic waves composing Hawaiian volcanic tremor and gas-piston events observed by a near source array. J. Geophys. Res. 96, 6199-6209.

Furumoto, M., Kunimoto, T., Inoue, H., Yamada, I., Yamaoka, K., Ikami, A., Fukao, Y., 1990. Twin sources of high-frequency volcanic tremor of Izu-Oshima volcano, Japan. Geophys. Res. Lett. 17, 25– 27.

Galeczka, I., Oelkers, E.H., Gislason, S.R., 2014. The chemistry and element fluxes of the July 2011 Múlakvísl and Kaldakvísl glacial floods, Iceland. J. Volcanol. Geotherm. Res. 273, 41–57. doi:10.1016/j.jvolgeores.2013.12.004

Goldstein, P., Chouet, B., 1994. Array measurement and modelling of sources of shallow volcanic tremor at Kilauea volcano, Hawaii. J. Geophys. Res. 99, 2637– 2652.

Guðmundsson, M.T., Högnadóttir, P., Kristinsson, A.B., Guðbjörnsson, S., 2007. Geothermal activity in the subglacial Katla caldera, Iceland, 1999-2005, studied with radar altimetry. Ann. Glaciol. 45, 66–72. doi:10.3189/172756407782282444

Guðmundsson, M.T., Larsen, G., Hoskuldsson, A., Gylfason, A.G., 2008. Volcanic hazards in Iceland. Jökull 58, 251–268.

Guðmundsson, M.T., Larsen, G., Sigmarsson, O., 2013. In: Sólnes, J., Sigmundsson, F., Bessason, B. (Eds.), Náttúruvá á Íslándi. Eldgos og jarðskjálftar. Viðlagatrygging Íslands/Háskólaútgáfan, p. 2013.

Guðmundsson, Ó., Brandsdóttir, B., 2010. Geothermal noise at Ölkelduháls, SW Iceland. Jökull 60, 89-102.

Guðmundsson, Ó., Brandsdóttir, B., Menke, W., Sigvaldason, G., 1994. The Crustal Magma Chamber of the Katla Volcano in South Iceland Revealed By 2-D Seismic Undershooting. Geophys. J. Int. 119, 277–296. doi:10.1111/j.1365-246X.1994.tb00928.x

Haney, M.M., Nies, A., Masterlark, T., Needy, S., Pedersen, R., 2011. Interpretation of Rayleigh-wave ellipticity observed with multicomponent passive seismic interferometry at Hekla Volcano, Iceland. Lead. Edge 30, 526–531. doi:10.1190/1.3589111

IMO, Icelandic Meteorological Office, 2011. http://en.vedur.is/

IMO, Icelandic Meteorological Office, 2015. Delivery of data from the Hydrological database, no. 2015-09-23/01.

Jeddi, Z., Tryggvason, A., Guðmundsson, Ó., IMO-SIL monitoring group, 2015. 3D Velocity structure of the Katla volcano - Southern Iceland. Poster session presented at: 26th IUGG General Assembly 2015. Prague, Czech Republic.

Jellinek, A.M., Bercovici, D., 2011. Seismic tremors and magma wagging during explosive volcanism. Nature 470, 522–525.

Jolly, a. D., Jousset, P., Lyons, J.J., Carniel, R., Fournier, N., Fry, B., Miller, C., 2014. Seismo-acoustic evidence for an avalanche driven phreatic eruption through a beheaded hydrothermal system: An example from the 2012 Tongariro eruption. J. Volcanol. Geotherm. Res. 286, 331–347. doi:10.1016/j.jvolgeores.2014.04.007

Jónsdóttir, K., Roberts, R., Pohjola, V., Lund, B., Shomali, Z.H., Tryggvason, A., Bövarsson, R., 2009. Glacial long period seismic events at Katla volcano, Iceland. Geophys. Res. Lett. 36, 1–5. doi:10.1029/2009GL038234

Jónsson, G., Kristjánsson, L., 2000. Aeromagnetic measurements over Mýrdalsjökull and vicinity. Jökull 49, 47–58.

Julian, B.R., 1994. Volcanic tremor: Nonlinear excitation by fluid flow. J. Geophys. Res. 99, 11859. doi:10.1029/93JB03129

Konstantinou, K.I., Schlindwein, V., 2002. Nature, wavefield properties and source mechanism of volcanic tremor: A review. J. Volcanol. Geotherm. Res. 119, 161–187. doi:10.1016/S0377-0273(02)00311-6

Larsen, G., 2000. Holocene eruptions within the Katla volcanic system, south Iceland: Characteristics and environmental impact. Jökull 49, 1–28.

Leet, R.C., 1988. Saturated and subcooled hydrothermal boiling in groundwater flow channels as a source of harmonic tremor. J. Geophys. Res. 93, 4835. doi:10.1029/JB093iB05p04835

Li, K.L., Roberts R., Gudmundsson, Ó, Sadeghisorkhani, H., 2015. Extracting traveltime information using a multistation cross correlation technique. Poster session presented at: 26th IUGG General Assembly 2015. Prague, Czech Republic.

Magnússon, E., Guðmundsson, M.T., Roberts, M.J., Sigurðsson, G., Höskuldsson, F., Oddsson, B., 2012. Ice-volcano interactions during the 2010 Eyjafjallajökull eruption, as revealed by airborne imaging radar. J. Geophys. Res. Solid Earth 117, 1–17. doi:10.1029/2012JB009250

McNutt, S.R., 2005. Volcanic Seismology. Annu. Rev. Earth Planet. Sci. 33, 461–491. doi:10.1146/annurev.earth.33.092203.122459

Métaxian, J.-P., Araujo, S., Mora, M., Lesage P., 2003. Seismicity related to the glacier of Cotopaxi Volcano, Ecuador. Geophys. Res. Lett. 30(9), 1483. doi: 10.1029/2002GL016773

Métaxian, J.-P., Lesage, P., Dorel, J., 1997. Permanent tremor of Masaya volcano, Nicaragua: wave field analysis and source location. J. Geophys. Res. 102, 22529– 22545.

Morgan, L.A., Shanks III, W.C.P., Pierce, K.L., 2009. Hydrothermal processes above the Yellowstone magma chamber: Large hydrothermal systems and large hydrothermal explosions. Spec. Pap. Geol. Soc. Am. 1–95. doi:10.1130/2009.2459

Óladóttir, B.A., Sigmarsson, O., Larsen, G., Thordarson, T., 2008. Katla volcano, Iceland: Magma composition, dynamics and eruption frequency as recorded by Holocene tephra layers. Bull. Volcanol. 70, 475–493. doi:10.1007/s00445-007-0150-5

Ripepe, M., 1996. Evidence for gas influence on volcanic signals recorded at Stromboli. J. Volcanol. Geotherm. Res. 70, 221-233.

Roberts, M. J., Tweed, F. S., Russell, A. J., Knudsen, Ó., Harris, T. D., 2003. Hydrological and geomorphic effects of temporary ice-dammed lake formation during jökulhlaups. Earth Surf. Processes Landforms 28, 723– 737.

Shapiro, N.M., Ritzwoller, M.H., Bensen, G.D., 2006. Surce location of the 26 sec microseism from cross-correlations of ambient seismic noise. Geophys. Res. Lett. 33, 1–5. doi:10.1029/2006GL027010

Sgattoni, G., Guðmundsson, Ó., Einarsson, P., Lucchi, F. Relative relocation of earthquakes without a predefined velocity model: an example from a peculiar seismic cluster on Katla volcano's south-flank (Iceland). Submitted to J. Geophys. Int.

Sgattoni G., Jeddi, Z., Guðmundsson, Ó., Einarsson, P., Tryggvason, A., Lund, B., Lucchi, F., 2015. Long-period events with strikingly regular temporal patterns on Katla volcano's south flank (Iceland). arXiv:1511.05852 http://arxiv.org/ftp/arxiv/papers/ .

Sigurðsson, O., Zóphoníasson, S., Ísleifsson, E., 2000. Jökulhlaup úr Sölheimajökli 18. júlí 1999 (The jökulhlaup from Sólheimajökull July 18, 1999, in Icelandic with English summary), Jökull 49, 75–80.

Soosalu, H., Jónsdóttir, K., Einarsson, P., 2006. Seismicity crisis at the Katla volcano, Iceland-signs of a cryptodome? J. Volcanol. Geotherm. Res. 153, 177–186. doi:10.1016/j.jvolgeores.2005.10.013

Spaans, K., Hreinsdóttir, S., Hooper, A., Ófeigsson, B.G., 2015. Crustal movements due to Iceland's shrinking ice caps mimic magma inflow signal at Katla volcano. Sci. Rep. 5, 10285. doi: 10.1038/srep10285

Sturkell, E., Einarsson, P., Sigmundsson, F., Geirsson, H., Ólafsson, H., Pedersen, R., de Zeeuw-van Dalfsen, E., Linde, A.T., Sacks, S.I., Stefánsson, R., 2006. Volcano geodesy and magma dynamics in Iceland. J. Volcanol. Geotherm. Res. 150, 14–34. doi:10.1016/j.jvolgeores.2005.07.010

Sturkell, E., Einarsson, P., Roberts, M.J., Geirsson, H., Guðmundsson, M.T., Sigmundsson, F., Pinel, V., Guðmundsson, G.B., Olafsson, H., Stefansson, R., 2008. Seismic and geodetic insights into magma accumulation at Katla subglacial volcano, Iceland: 1999 to 2005. J. Geophys. Res. 113, B03212.

Sturkell, E., Einarsson, P., Sigmundsson, F., Hooper, A., Ófeigsson, B. G., Geirsson, H., Ólafsson, H., 2010. Katla and Eyjafjallajökull Volcanoes. In: Schomacker, A., Krüger, J., Kjær, K.H. (Eds). The Mýrdalsjökull icecap, Iceland. Glacial processes, sediments and landforms on an active volcano. Developments in Quaternary Science 13. Elsevier, Amsterdam. ISBN 1571-0866, pp. 5–21.

Sveinsson, G., 1919. Kotlugosid 1918 og afleidingar thess (The Katla eruption of 1918 and its consequences). Reykjavık, Prentsmidja Gutenbergs, 61p.

Thorarinsson, S., 1975. Katla og annall Kotlugosa. Arbok Ferdafelags Islands. Ferdafelag Íslands, Reykjavık, 125–149.

Thordarson, T., Miller, D.J., Larsen, G., Self, S., Sigurdsson, H., 2001. New estimates of sulfur degassing and atmospheric mass-loading by the 934 AD Eldgjá eruption, Iceland. J. Volcanol. Geotherm. Res. 108, 33–54. doi:10.1016/S0377-0273(00)00277-8

Wegler, U., Seidl, D., 1997. Kinematic parameters of the tremor wavefield at Mt. Etna (Sicily). Geophys. Res. Lett. 24, 759-762.

Zóphóníasson, S., Pálsson, S., 1996. Rennsli í Skaftárhlaupum og aur- og efnastyrkur í hlaupum 1994, 1995 og 1996. National Energy Authority, report OS- 96066/ VOD-07. [In Icelandic]

Supplementary material: Appendix A

Figs. A1, A2, A3. a) Integral amplitude spectral density at all stations as a function of time. b) The same plotted on a logarithmic scale. In both cases the background power has been subtracted and the amplitude normalised by the average background at station KKE. c) and d) station coefficients obtained with LSQ fit of the power time-history over 10 minute intervals. c) KKE coefficients, normalised by the mean of all other stations' coefficients, in each time interval. d) all other stations' coefficients, normalised by KKE coefficients. Results are shown for the three frequency bands: 0.8-1.5 Hz in Fig. A1, 1.5-4.0 Hz in Fig. A2, 4.0-9.0 Hz in Fig. A3.

Figure A1

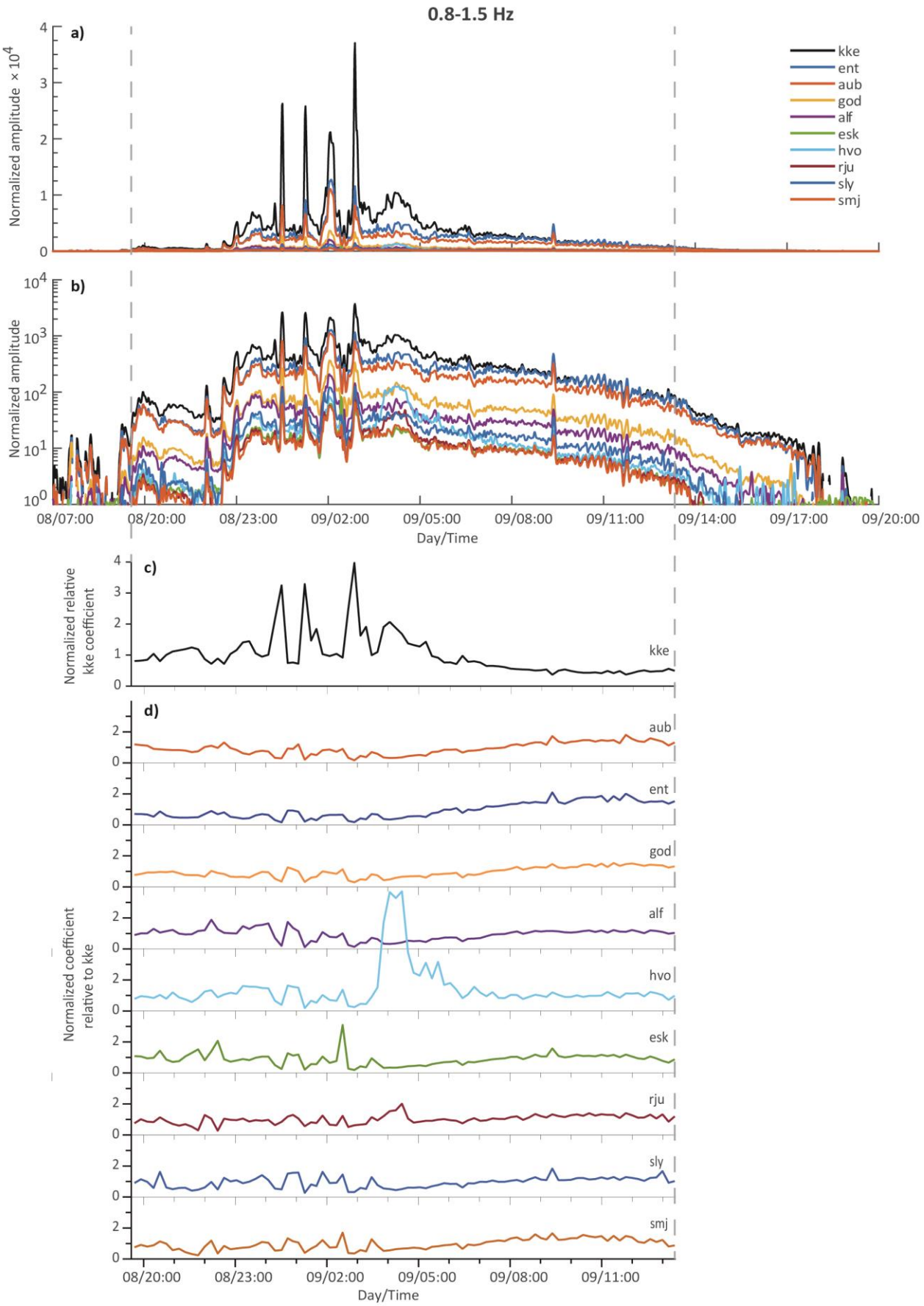
0.8-1.5 Hz
a)
b)
c)
d)
Normalized amplitude × 10^4
Normalized amplitude
Normalized relative kke coefficient
Normalized coefficient relative to kke
kke
ent
aub
god
alf
esk
hvo
rju
sly
smj
08/07:00
08/20:00
08/23:00
09/02:00
09/05:00
09/08:00
09/11:00
09/14:00
09/17:00
09/20:00
Day/Time

Figure A2

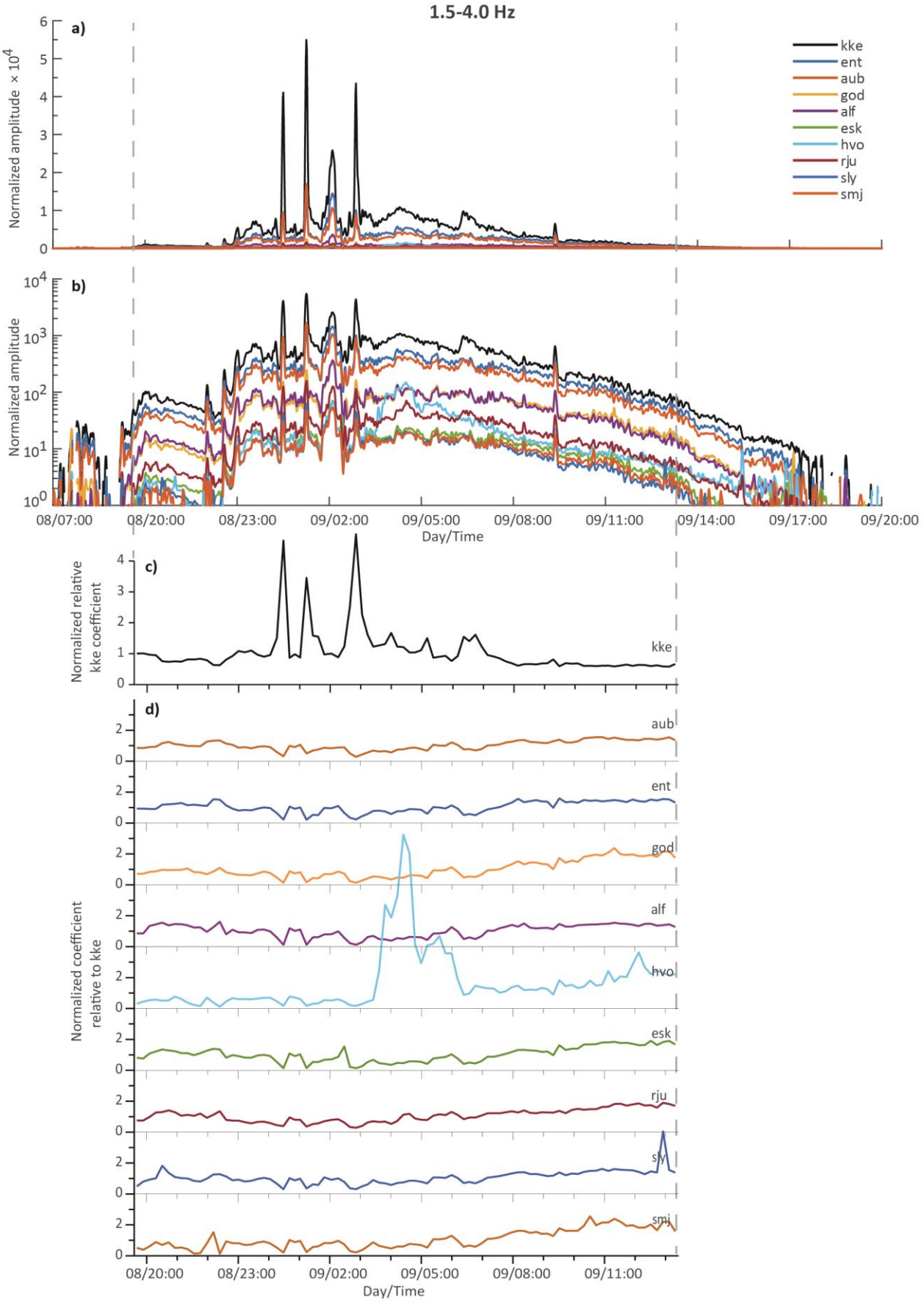
1.5-4.0 Hz
a)
Normalized amplitude × 10^4
kke
ent
aub
god
alf
esk
hvo
rju
sly
smj
b)
Normalized amplitude
08/07:00
08/20:00
08/23:00
09/02:00
09/05:00
09/08:00
09/11:00
09/14:00
09/17:00
09/20:00
Day/Time
c)
Normalized relative kke coefficient
d)
Normalized coefficient relative to kke
08/20:00
08/23:00
09/02:00
09/05:00
09/08:00
09/11:00
Day/Time

Figure A3

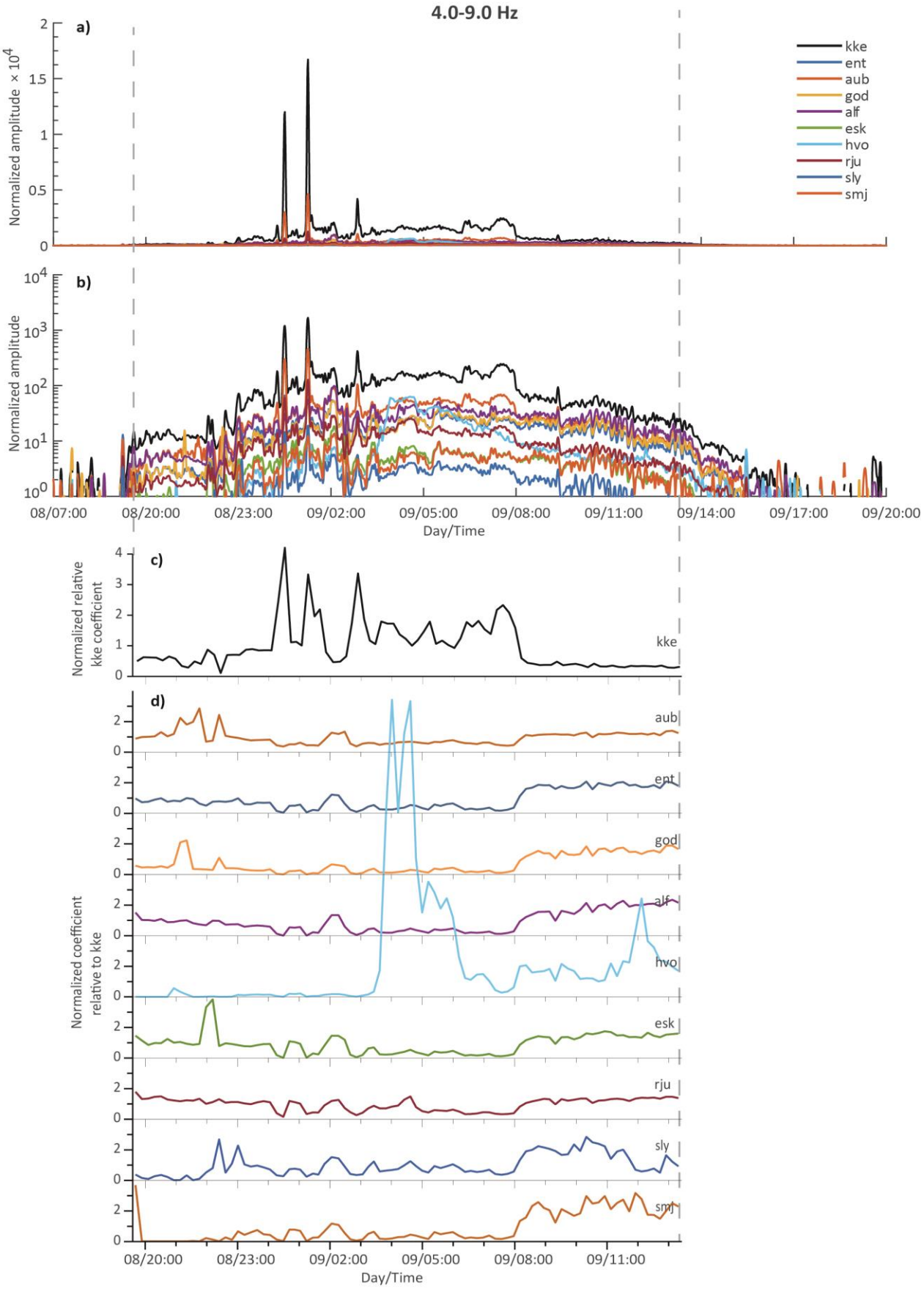
4.0-9.0 Hz
a)
b)
c)
d)
Normalized amplitude × 10^4
Normalized amplitude
Normalized relative kke coefficient
Normalized coefficient relative to kke
kke
ent
aub
god
alf
esk
hvo
rju
sly
smj
08/07:00
08/20:00
08/23:00
09/02:00
09/05:00
09/08:00
09/11:00
09/14:00
09/17:00
09/20:00
Day/Time

Supplementary material: Appendix B – A double-correlation location method

Introduction

Here we introduce a method to locate tremor sources based on stacks of back-projected, doubly-correlated tremor records at multiple triplets of seismographs to hypothetical source locations in an aerial grid. Peaks in the resulting stack are inferred source locations.

Many Earth processes, especially in volcanic areas, produce complex seismic signals lacking a clear onset, such as emergent events or continuous tremor. We cannot pick their onsets in order to locate their sources. Instead, amplitude decay with distance has, e.g., been used [Battaglia and Aki, 2003; Di Grazia et al., 2006]. This requires simplistic assumptions about geometrical spreading, site magnification and attenuation and does not work well for the tremor data presented here. Another strategy is to use array methods such as beam forming, FK analysis or semblance methods [Furumoto et al., 1990; Konstantinou and Schlindwein, 2002], requiring dense sampling of the wave field yielding direction and slowness or vectorial wave number. Combining such estimates at multiple dense arrays constrains the source location. Haney [2010] measured differential travel times extracted from cross-correlations of recordings of very-long-period (VLP) volcanic tremor at different stations and inverted those for the source location. Inter-station cross-correlation has become a common tool for analysis of seismic ambient noise over the past decade.

Numerous authors have used cross-correlation analysis in order to assess the spatial distribution of ambient noise sources. Shapiro et al., [2006] located a spurious peak near the primary microseismic peak at 26 s period in the Gulf of Guinea by back-projecting noise correlations two dimensionally. Gudmundsson and Brandsdóttir [2010], Zeng and Ni [2010], Ballmer et al. [2013] and Droznin [2015] used similar approaches to locate persistent sources of geothermal noise in Iceland, microseisms around Japan and volcanic tremor in Hawaii and Kamchatka, respectively. All such methods require detailed information about seismic velocity in the area. Because this information is often insufficiently precise, a number of the above studies stacked envelopes of cross correlations rather than the cross-correlations themselves.

If we think of a tremor or noise source as a point source which is incoherent in time and consider a simple medium between that source and all recording seismographs, then the recorded tremor (noise) will consist of a continuous interference pattern between the same source functions at random time intervals, but at a fixed delay for one station compared to any other corresponding to the differential travel time from the source to the two stations. Recordings of the tremor at two stations will, therefore, correlate at that time lag, cancelling

the random time of each source pulse by a relative measurement. This is the principle that all of the above methods make use of. In addition, correlation is an effective tool to suppress noise, or any signal that is incoherent at the particular time lags assumed.

Each differential travel-time extracted by correlation of tremor recorded at two stations does not constrain the source location to a point alone. Instead, it will constrain the location to lie anywhere on a hyperbolic surface corresponding to equal differential distance from the source (assuming a uniform velocity). If we restrict the propagation to two dimensions the solutions are constrained to lie on a hyperbolic curve. With information from two station pairs, we have two hyperbolic curves, which will usually intersect at one or two points. Further station pairs will provide redundant constraints on a single point solution. Thus, we need differential travel-time measurements from at least two station pairs to locate a source in two dimensions. Similarly, we need three pairs to locate a source in 3D.

If we back-project the corresponding correlation functions to hypothetical source locations, again using uniform velocity, the energy distribution for each of them will peak on the same hyperbolic surface. Stacking two of them will usually produce a peak at a point, while stacking more station pairs will enhance that peak.

The premise of this argument is simplistic. We need to know the velocity well, which we may not. The tremor signals may contain both body and surface waves, so, it becomes ambiguous which velocity to use or if we need to solve a two-dimensional or a three-dimensional problem. The Green's functions between the source and different receivers may be complex and differ by more than a time delay from one station to the other.

If the recorded signals at different stations are significantly different due to source or propagation complexity, then the correlograms may correlate poorly. However, variations in the tremor source activity level should still produce similar variations at each station in the more slowly-varying correlogram envelopes. Use of envelopes will stabilize the back-projection at a loss of spatial resolution. The other problems can only be evaluated by synthetic simulation, which we will discuss later.

Double-correlation

Our method of location extends the above methods by applying double correlation instead of a single correlation. The straightforward definition of the correlation of tremor series at a pair of stations, *a* and *b*, is:

$$C_{ab}(j) = \sum_{i=1}^{N-j} a(i)b(i+j) \qquad \text{B1}$$

Having computed a second such correlation for stations c and d:

$$C_{cd}(k) = \sum_{i=1}^{N-k} c(i)d(i+k) \qquad \text{B2}$$

we can then define a double correlation as:

$$C_{abcd}(m) = \sum_{j=-N-m}^{N-m} C_{ab}(j)C_{cd}(j+m) \qquad \text{B3}$$

This is useful for two purposes. First, the level of redundancy is somewhat increased over a single correlation, which suppresses random noise. Second, this double correlation will peak at the double differential travel-time between the two pairs and if we back-project this function to the source in two dimensions it will concentrate energy around a point as opposed to a hyperbola for the back-projection of a single correlation.

This is, however, not how we implement double correlation. First, we note that the sum in equation B3 will not have much of a contribution from time lags beyond a finite limit corresponding to the possible differential travel times of sources within the network. Second, if secondary, spurious correlation persists in the correlations C_{ab} and C_{dc}, then they will contribute higher-order correlation peaks in C_{abcd}. We define double correlation in the following manner. First, we select a triplet of stations, a, b and c. Then, we select one of those as a reference station, for example a, and correlate stations a and b on one hand and stations a and c on the other. Before doing this, we divide the time span of our observations, T, into K equal sub intervals of length $\Delta T = T/K$ and convert our time series to an analytical signal:

$$\hat{f}(t) = f(t) + i\mathcal{H}\{f(t)\} \qquad \text{B4}$$

We then compute the correlations:

$$_k\hat{C}_{ab}(j) = \sum_{i=k\Delta T}^{(k+1)\Delta T} \hat{a}(i)\hat{b}^{\#}(i+j) \qquad _k\hat{C}_{ac}(j) = \sum_{i=k\Delta T}^{(k+1)\Delta T} \hat{a}(i)\hat{c}^{\#}(i+j) \qquad \text{B5}$$

where the time series are all complex and # indicates the complex conjugate. Finally, we correlate those two:

$$\hat{C}_{abc}(m) = \sum_{k=0}^{K-1} {}_k\hat{C}_{ab}(j)\,{}_k\hat{C}^{\#}_{ac}(j+m) \qquad \text{B6}$$

For a population of n stations in a network there will be $\binom{n}{3}$ combinations of three stations and for each three possible choices of a reference station. The order of the remaining two stations in each triplet is arbitrary and the two choices completely redundant. There are therefore N independent triplets, where N is:

$$N = 3\binom{n}{3} \qquad \text{B7}$$

For a $n = 10$ station network the number of triplets is $N = 360$.

The amplitude of this complex double correlation C_{abc} is a measure of the double correlation at a given differential time-shift. It will peak at the double differential travel-time between the two station pairs. The phase of C_{abc} is a measure of the interpolation between the discrete samples of time shift to the true maximum correlation. This double correlation will suppress random noise beyond single correlation and suppress non-stationary correlated noise. Stacking the back-projected double correlations for all triplets will further suppress correlated peaks that are not common for all triplets, e.g. components of the Green's functions between source and stations that vary from one path to another. A further advantage of this double correlation is that each back-projection provides a localized estimate of the source location (in two dimensions). Therefore, when we back-project to a hypothetical source and stack different such double correlations we stack equivalent estimates of the source, while stacking single correlations involves stacking hyperbolic distributions that have very different localization properties.

The back-projection is done in the following straight-forward manner: For each hypothetical source location the travel time to any given station is computed using a velocity model. The time lag between stations a and b and stations a and c is thus estimated and their double difference computed. The value of back-projection is then the value of the corresponding double correlation at that differential lag. These are then stacked over all triplets.

Synthetic tests

We have tested this approach with various synthetic tests. When using perfect data in a uniform velocity structure, the source is perfectly recovered with a resolution limitation controlled by the frequency content of the data. With significant velocity heterogeneity (compared to the finite frequency limitation) we lose our ability to predict travel time

precisely. This results in erratic phase behavior. However, the modulus of the back-projected double correlation remains stable, but its finite width, controlled by the frequency band width of the data, translates into a broader spatial constraint on the location.

We have tested the method also with synthetic data generated by delaying a random sequence of impulse sources at a point inside the Katla caldera according to a two-dimensional velocity model for surface waves to elements of the Katla network of seismographs. We have added corresponding impulses delayed according to a simple body-wave model. We have added random noise to the synthetic time series and correlated them. Finally, we have added a set of random scatterers given a random strength, a random scattering width and a random orientation. The tests are done with seismograms filtered in the same frequency range as the lowest frequency interval in the Katla tremor data (0.8-1.5 Hz). The back-projection is done with a uniform velocity. The velocity is selected so that it focuses the resulting energy-stack maximally as judged graphically.

These tests reveal that, even with a strong velocity variation of ±15% (root-mean-square level of heterogeneity) with a correlation length of 7 km, we still recover the source location to within a few km. Noise suppression is very effective and the point-source location is well recovered even if the signal is buried in noise by a factor of 2 (signal-to-noise ratio is 0.5). The body-wave component of the synthetic tremorgrams is coherent at time delays corresponding to distance and velocities that are very different from those for the surface waves and does not significantly affect the recovery of the point source even if given a relative amplitude three times as big as the surface-wave component. The most limiting synthetic component is the addition of scatterers. With 50 scatterers randomly distributed within the caldera given a random orientation and a Gaussian width of ±40° (one standard deviation) and a random scattering strength between 0 and 1, we simulate the appearance of the stacked, back-projected energy distribution obtained with the real data.

Two examples of simulations are shown in Figure B1. In Fig B1a we show the back-projected energy with synthetic data containing velocity heterogeneity (±20% velocity variation, 7 km correlation length), added white noise (signal to noise ratio of 1) and a body-wave component equal to the surface-wave component in amplitude. The source, which is located at coordinates (2, -4) is clearly resolved. In Fig B1b we have added 100 random scatterers with the same geometrical characteristics as described before. In this case the source is considerably spread and the energy distribution decays more slowly away from the sources, similar to the real data. Note the common structure in the peripheral distribution which is controlled by the station geometry.

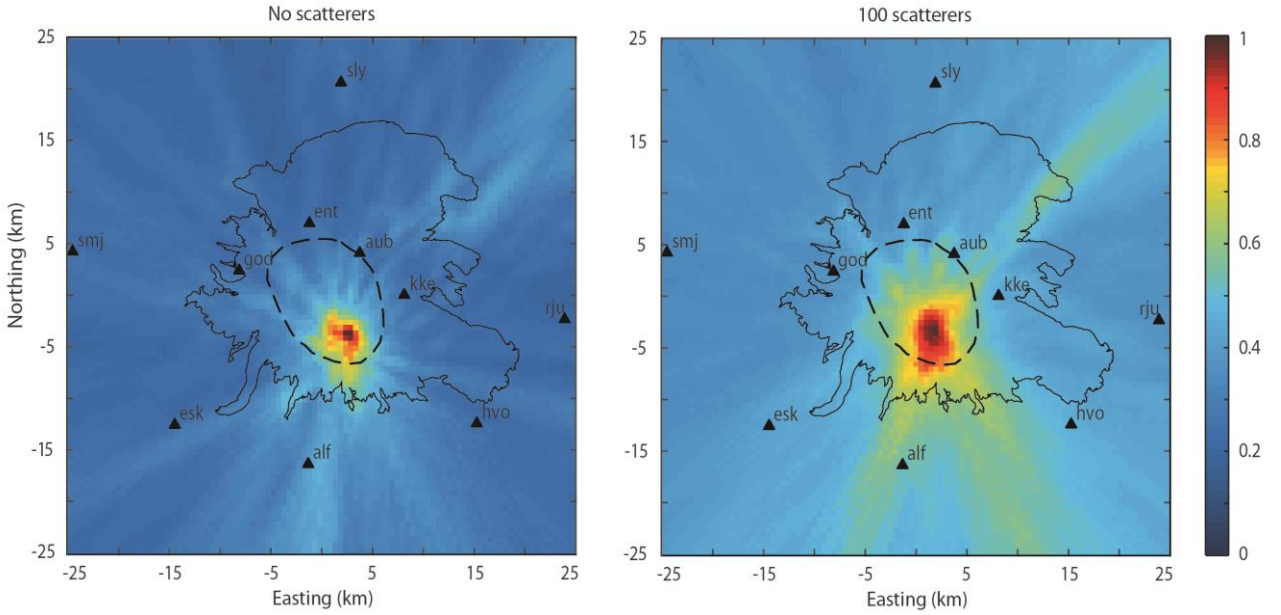

Fig. B1: Results from simulations with (a) and without (b) scatterers. The colours define normalised energy, dark red for maximum energy. Black solid line: glacier. Black dashed line: caldera outline. Black triangles: seismic stations.

Conclusions

We conclude from these tests that we can recover the dominant source location with a resolution of a few km with the Katla network with the data at hand. We need not assume that the tremor is dominantly composed of surface waves for a two-dimensional back-projection to work as at surface-wave velocities the body-wave components do not stack coherently. Back-projecting in 2D limits our resolution to two dimensions, so source depth cannot be recovered. If the source has a finite depth, a phase shift will be introduced into the surface waves, but this will be common to all observations and, therefore, cancel in the double-differential times of the double correlation.

For the higher frequencies (1.5-4 Hz and 4 – 9 Hz) of the Katla data we are not able to recover a coherent picture of the source with this method. We suspect that is caused by increasing vigour of scattering effects at increasing frequency in tune with the fact that addition of discrete scatterers for the 0.8-1.5 Hz range proved to be by far the most obscuring effect out of those that we synthesized.

References

Ballmer, S., Wolfe, C.J., Okubo, P.G., Haney, M.M., Thurber, C.H., 2013. Ambient seismic noise interferometry in Hawai'i reveals long-range observability of volcanic tremor. Geophys. J. Int. 194, 512–523. doi:10.1093/gji/ggt112

Battaglia, J., Aki, K., 2003. Location of seismic events and eruptive fissures on the Piton de la Fournaise volcano using seismic amplitudes. J. Geophys. Res. 108 (B8).

Di Grazia, G., Falsaperla, S., Langer, H., 2006. Volcanic tremor location during the 2004 Mount Etna lava effusion. Geophys. Res. Lett. 33, L04304. doi:10.1029/2005GL025177

Droznin, D.V., Shapiro, N.M., Droznina, S.Y., Senyukov, S.L., Chebrov, V.N., Gordeev, E.I., 2015. Detecting and locating volcanic tremors on the Klyuchevskoy group of volcanoes (Kamchatka) based on correlations of continuous seismic records. Geophys. J. Int. 203 , 1001–1010. doi:10.1093/gji/ggv342

Furumoto, M., Kunimoto, T., Inoue, H., Yamada, I., Yamaoka, K., Ikami, A., Fukao, Y., 1990. Twin sources of high-frequency volcanic tremor of Izu-Oshima volcano, Japan. Geophys. Res. Lett. 17, 25– 27.

Guðmundsson, Ó., Brandsdóttir, B., 2010. Geothermal noise at Ölkelduháls, SW Iceland. Jökull 60, 89-102.

Haney, M.M., Nies, A., Masterlark, T., Needy, S., Pedersen, R., 2011. Interpretation of Rayleigh-wave ellipticity observed with multicomponent passive seismic interferometry at Hekla Volcano, Iceland. Lead. Edge 30, 526–531. doi:10.1190/1.3589111

Konstantinou, K.I., Schlindwein, V., 2002. Nature, wavefield properties and source mechanism of volcanic tremor: A review. J. Volcanol. Geotherm. Res. 119, 161–187. doi:10.1016/S0377-0273(02)00311-6

Shapiro, N.M., Ritzwoller, M.H., Bensen, G.D., 2006. Surce location of the 26 sec microseism from cross-correlations of ambient seismic noise. Geophys. Res. Lett. 33, 1–5. doi:10.1029/2006GL027010

Zeng, X., Ni, S., 2010. A persistent localized microseismic source near the Kyushu Island, Japan, Geophys. Res. Lett. 37, 24. doi:10.1029/2010GL045774.

6. PAPER 4

The 2011 unrest at Katla volcano, Iceland: seismicity and geology context

Giulia Sgattoni[1,2,3*], Federico Lucchi[1], Páll Einarsson[2], Ólafur Guðmundsson[3], Gianfilippo De Astis[4], Claudio Antonio Tranne[1]

[1] Department of Biological, Geological and Environmental Sciences, University of Bologna, Bologna, Italy

[2] Institute of Earth Sciences, Science Institute, University of Iceland, Reykjavik, Iceland

[3] Department of Earth Sciences, Uppsala University, Uppsala, Sweden

[4] National Institute of Geophysics and Volcanology (INGV), Rome, Italy

to be submitted to *Bulletin of Volcanology*

Abstract

Katla is one of the most active volcanoes in Iceland and is characterised by persistent seismicity. It is partly covered by Mýrdalsjökull glacier and its activity is dominated by phreatomagmatic eruptions associated with catastrophic glacial floods. In July 2011 a sudden jökulhlaup was released from the glacier, associated with tremor, intense seismicity inside the caldera and a new seismicity on the south flank. This was likely caused by a hydrothermal or magmatic event, possibly a small subglacial eruption. Similar unrests occurred in 1955 and 1999. We have identified changes of the seismicity pattern in coincidence with the 2011 unrest, suggesting a modification in the volcanic system. It may be speculated that if the persistent seismicity at Katla is the indication of a pressurized system ready to erupt, a small event like those of 1955, 1999 and 2011, may trigger larger eruptions in the future. We have also conducted a pilot study of the geology of the south flank, where the new seismicity is recorded, and identified sources for flank eruptions in the recent eruptive history of Katla. These include rhyolitic domes and hyaloclastic to surtseyan craters. Renovated volcanic processes have, therefore, to be taken into account as possible source for the new seismicity. The 2011 activity has directed attention to the south flank of Katla that has so far not been considered a source of serious volcanic hazard.

Keywords: Katla volcano, Iceland, volcano seismicity, long-period earthquakes, silicic intrusion, flank eruption

1. Introduction

The study of subglacial volcanoes is crucial, as magma-ice interaction can produce highly explosive eruptions and jökulhlaups (glacial floods), but problematic, because the ice cover prevents direct observations and complicates the understanding of geophysical signals. The Katla volcanic system, in south Iceland, is a prime example. Katla hosts a large caldera covered by Mýrdalsjökull ice cap and is a peculiar volcano for its persistent seismicity also during periods of volcanic quiescence. It is one of the most active volcanoes in Iceland and its volcanic activity is dominated by explosive, hydromagmatic eruptions. The last eruption to break the ice surface occurred in 1918 and the current repose time is the longest known in history (Larsen 2000).

After the eruption of Eyjafjallajökull in 2010, the scientists' attention was pointed to Katla, as several previous Eyjafjallajökull's eruptions were followed by the neighbouring Katla

(Einarsson and Hjartardóttir 2015). However, no visible eruption occurred. But in July 2011 increased seismicity, a tremor burst and a jökulhlaup occurred that caused considerable damage to infrastructure. This episode was similar to two other events that occurred in 1955 and 1999 and some authors have interpreted as minor subglacial eruptions (Thorarinsson 1975; Guðmundsson et al. 2007). However, the interpretation is controversial, as no eruptive products were identified. The same general controversy applies to the 2011 unrest. This episode may have been related to either a geothermal event with no magma involved or a small subglacial eruption (Chapter 5).

The seismic activity at Katla has been concentrated in two main source areas, inside the caldera and at Goðabunga, with the latter being much more active, at least until the end of 2004 (Sturkell et al. 2006). Seasonal patterns have also been reported with different features for the two clusters (Einarsson and Brandsdóttir 2000; Jónsdóttir et al. 2009). Clear changes in the seismicity at Katla occurred in July 2011. The 2011 unrest was associated not only with increased seismicity inside the caldera, but also with the onset of new seismicity on the south flank of the volcano, at the glacier rim (Sgattoni et al. 2015; Sgattoni et al. subm.). No seismic activity is reported to have occurred there before and little is known about the geology of the area.

This encouraged a geological study of the Gvendarfell area, where the new seismic source is located, aimed at identifying the main geological and tectonic features possibly connected with seismic sources. This geological survey brought new light on the southern flank of Katla that had been little studied before. In this article we place the 2011 unrest episode at Katla in the broader context of its geology and eruption history. Moreover, we analyse the general changes of the historical seismicity at Katla by looking at the seismic catalogue from 1998 to 2015. We use this information to shed light on the 2011 unrest and speculate on its interpretation.

2. The Katla volcanic system

2.1. Geological overview

The Katla volcanic system, in South Iceland, consists of a central volcano mostly covered by the Mýrdalsjökull ice cap, connected to the Eldgjá fissure system extending 75 km to the northeast (Larsen 2000; Thordarson et al. 2001). The central volcano hosts an ice-filled caldera 10x14 km wide and 650-750 m deep, as revealed by radio echo measurements (Björnsson et al. 2000). Three main glaciers descend from the ice cap through deep gaps in the southeast, southwest and northwest caldera walls. These correspond to the three main

possible paths for jökulhlaups. Several ice cauldrons (at least 16) located within and at the caldera rim, represent the surface expression of subglacial geothermal activity Guðmundsson et al. 2007).

Katla is located just south of the intersection between the Eastern Volcanic Zone (EVZ) and the transform boundary of the South Iceland Seismic Zone (Sturkell et al. 2008). The active rifting in the EVZ terminates just north of Mýrdalsjökull. Therefore Katla and the neighbouring Eyjafjallajökull move completely with the Eurasia plate (La Femina et al. 2005; Geirsson et al. 2006) and may be classified as intraplate volcanoes. An occasional connection with rifting in the EVZ is exemplified by the AD 934 Eldgjá eruption. Katla and Eyjafjallajökull appear to be tectonically connected, as Eyjafjallajökull E-W fissure swarm merges with the Katla radial fissure system (Einarsson and Brandsdóttir 2000).

A zone with reduced P-wave velocities and absent S-waves was identified beneath the Katla caldera with seismic undershooting and interpreted as the evidence of a magma chamber (Guðmundsson et al. 1994). This is confirmed by an aeromagnetic survey indicating the presence of a non-magnetic body within the same region (Jónsson and Kristjánsson 2000). The occurrence of a shallow magma reservoir is consistent with geobaromety analyses on historical basaltic tephra samples by Budd et al. (2014) that imply both shallow (<6 km) and deep crustal magma crystallization. However, tephra stratigraphy studies by Óladóttir et al. (2008) suggest that Katla has currently a simple plumbing system, with no shallow magma reservoirs.

The Katla volcanic system has possibly been active for several hundred thousand years (Jakobsson 1979; Björnsson et al. 2000). Its products consist of FeTi-rich alkali basalts and mildly alkalic rhyolites, with very subordinate intermediate rocks from magma mingling (Lacasse et al. 2007; Óladóttir et al. 2008). Most outcrops along the caldera rims and glacier margins are composed of rhyolitic lavas (Jóhannesson and Sæmundsson 2009; Lacasse et al, 2007). The largest explosive eruption known at Katla occurred ~11.980 cal years BP and produced the Sólheimar ignimbrite (>6 km^3; Grönvold et al. 1995; Lacasse et al. 2007). The age of the caldera is unknown.

2.2. Seismicity

Despite its tectonic location outside the main rift zones, persistent seismicity has been detected at Katla since the first sensitive seismographs were installed in Iceland in the 60ies (Einarsson and Brandsdóttir 2000). The only other volcanoes comparable to Katla in this respect are located along the active plate boundaries (Hengill and Bárðarbunga; Einarsson 1991; Jakobsdóttir, 2008).

Until the 2011 unrest, the seismic activity at Katla has been concentrated mostly within the caldera and immediately to the west, at Goðabunga (Fig. 1). The caldera seismicity consists mostly of high-frequency and hybrid events, probably associated with the subglacial geothermal activity and volcano-tectonic processes (Sturkell et al. 2010). The Goðabunga cluster consists mainly of low-frequency shallow events with emergent P-waves, unclear S-waves and long low-frequency coda. These events have a controversial interpretation, either as a response to a rising viscous cryptodome (Soosalu et al. 2006) or due to glacial processes such as ice-fall events (Jónsdóttir et al. 2009).

The Katla seismicity also shows a seasonal variation, particularly at Goðabunga, where the seismic activity peaks in autumn. A less pronounced peak of seismicity in the caldera occurs instead during the summer (Jónsdóttir et al. 2007). This seasonal correlation has been interpreted as a result of ice-load change and resulting pore pressure variation at the base of the glacier (Einarsson and Brandsdóttir 2000) or due to enhanced glacial motion during periods of distributed subglacial water channels (Jónsdóttir et al. 2009).

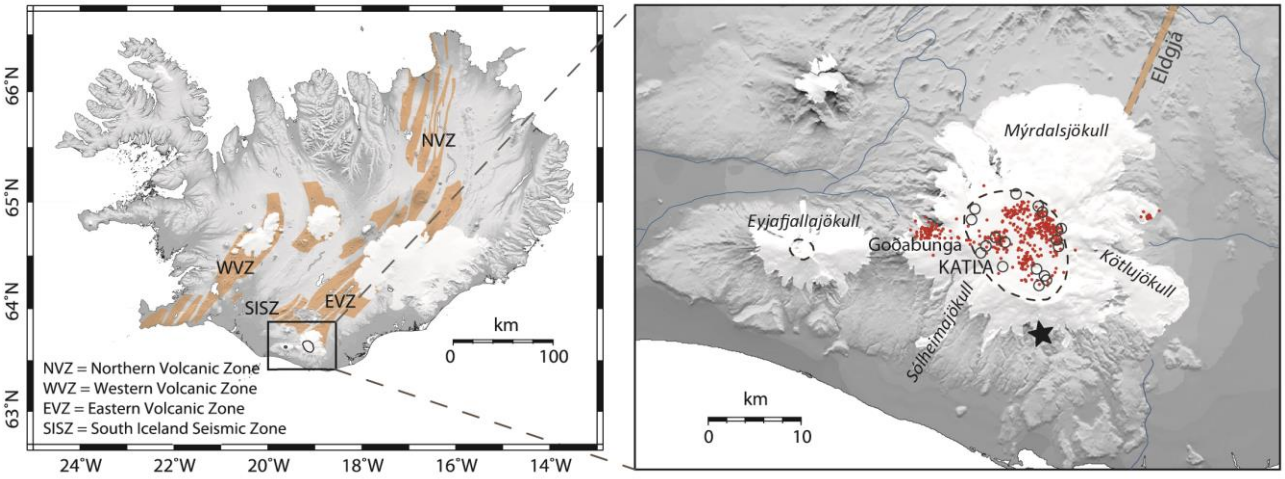

Fig. 1. Map of Iceland showing volcanic systems in orange (Einarsson and Sæmundsson 1987). In the inset, main seismic and geological features of Katla. Red dots: epicentres before July 2011, located inside the caldera and at Goðabunga. Back star: new cluster started in July 2011 (Sgattoni et al. 2015). Dashed lines: Katla and Eyjafjallajökull caldera rims. Open circles: ice cauldrons (Guðmundsson et al. 2007). White areas: glaciers. To the NE, the location of Eldgjá fissure.

2.3. Holocene volcanism

The Holocene volcanic activity at Katla has been characterized by three main eruption types. The most frequent are phreatomagmatic explosive eruptions due to magma-ice interaction below the glacier that produced jökulhlaups and widespread tephra layers (0.02-

1.5 km^3 volume; Thorarinsson 1975; Jakobsson 1979; Larsen 2000). At least 300 subglacial explosive eruptions are known during the Holocene, 20 in historical times (Óladóttir et al. 2005). The least common are effusive basaltic eruptions along the fissure system in the ice-free part of the volcanic system (8-10 during the Holocene). These include the two largest eruptions of AD 934-40 Eldgjá Fires (19.6 km^3; Thordarson et al. 2001) and ~7.7 ka Holmsá fires (≥5 km^3; Larsen 2000). Explosive silicic eruptions from the central volcano produced tephra fallout (<0.01-0.27 km^3; Larsen et al. 2001) and probably jökulhlaups (Larsen, 2000). At least 12 silicic tephra layers are recognized in the 1.7-6.6 ka time interval between the Holmsá and Eldgjá fires (Larsen 2000). A minor silicic component was erupted during the Eldgjá fires (Einarsson et al. 1980), but silicic eruptions are not reported since AD 870, possibly indicating a substantial change in the plumbing system caused by the Eldgjá eruption (Óladóttir et al. 2008).

In historical times, Katla has been the most productive volcanic system in Iceland in terms of magma volume erupted (Thordarson and Larsen 2006). It has erupted fairly regularly with 1-3 eruptions per century, with repose periods ranging between 13-95 years, 47 years on average since AD 1500 (Larsen 2000). The year of 14 Katla eruptions are known from historical records and the time of the year are known for 9 of them, in the last 400 years. All these eruptions occurred during the spring-fall seasons, suggesting a seasonal control on eruptive activity (Larsen 2000).

2.4. Recent activity

The last eruption to break the ice surface in June 1918 was an explosive basaltic eruption that, produced a ~14 km high eruptive plume and tephra fallout (0.7 km^3), accompanied by a massive jökulhlaup (Eggertsson 1919; Sveinsson 1919; Larsen 2000). The eruption site was located near the south rim of the caldera beneath ~400 m of ice.

Seismic crises, not associated with eruptive activity, occurred at Katla in 1967 and 1976-77 inside the caldera and at Goðabunga (Einarsson 1991).

Two minor subglacial eruptions with no tephra emission in the atmosphere may have occurred in June 1955 and July 1999. The 1955 event took place near the eastern rim of the caldera (Fig. 2) where two shallow ice-cauldrons formed and a small jökulhlaup drained from south-east Mýrdalsjökull (Thorarinsson 1975). In 1999, a new ice-cauldron formed on the glacier (Guðmundsson et al. 2007) and a jökulhlaup was released from south-west Mýrdalsjökull (Sigurðsson et al. 2000; Roberts et al. 2003), associated with earthquakes and bursts of tremor.

From 1999 to 2004, GPS measurements on nunataks exposed along the caldera rim revealed steady uplift of the volcano, interpreted to result from 0.01 km^3 magma accumulation (Sturkell et al. 2006; 2008). Consistently, Guðmundsson et al. (2007) showed that increased geothermal heat output occurred in 2001-2003 based on the evolution of ice cauldrons, together with the increased seismicity and ground uplift. A recent study by Spaans et al. (2015), suggested instead that the uplift may be due to glacial isostatic adjustment as a consequence of mass loss of Iceland's ice caps.

Continuous GPS measurements from stations around the caldera rim, showed that deformation consistent with inflation occurred between 2011 and 2012 consistent with inflation, which could suggest magma injection at shallow depth, although further analyses are being carried out (B.G. Ófeigsson and S. Hreinsdóttir, pers. comm.)

2.5. July 2011 unrest and new seismicity

A significant, general increase in seismicity started at Katla in July 2011 and lasted until winter. This followed a period of uplift of most ice cauldrons on Mýrdalsjökull (11-12 m at cauldron 16) between August 2010 and July 2011, resulting from water accumulation under the glacier (Guðmundsson et al. 2013)

The seismicity intensified especially in the southern sector of the caldera and culminated with a 23-hour tremor burst on July 8-9th (Chapter 5). No signs of eruption breaking the ice were observed, but a ~18 million m^3 jökulhlaup drained from Kötlujökull and some ice cauldrons deepened in the southern and eastern parts of Mýrdalsjökull (Fig. 2). The jökulhlaup swept away the bridge over Múlakvísl river early in the morning on July 9th. This coincided with a clear flood-related tremor phase lasting around 5 hours. Two main tremor sources were identified in the southern and eastern caldera, corresponding to the active cauldrons (Chapter 5).A study of the chemical composition of the flood water, conducted by Galeczka et al. (2014), did not show evidences that the water came into contact with magma.

At the same time, a new seismic source became active on the south flank in the Gvendarfell area (Fig. 2). This seismicity consists of LP (Long-Period) events with emergent P wave and an unclear S wave and has peculiar temporal patterns, with regular inter-event times modulated by a seasonal correlation. These events are located at the edge of the glaciated area and may therefore be related to both glacial and volcanic processes. Because of their temporal pattern and depth distribution of the hypocentres as inferred from relative relocation (Sgattoni et al. subm.), they have been interpreted in association with volcano-related processes, suggesting hydrothermal processes as more likely than magmatic (Sgattoni et al. 2015).

A similar, but comparatively much smaller, unrest episode occurred in July 2014. Increased water discharge was observed from Sólheimajökull and Kötlujökull outlet glaciers, accompanied by slightly increased water conductivity and increased seismicity that only lasted for a few weeks (IMO website).

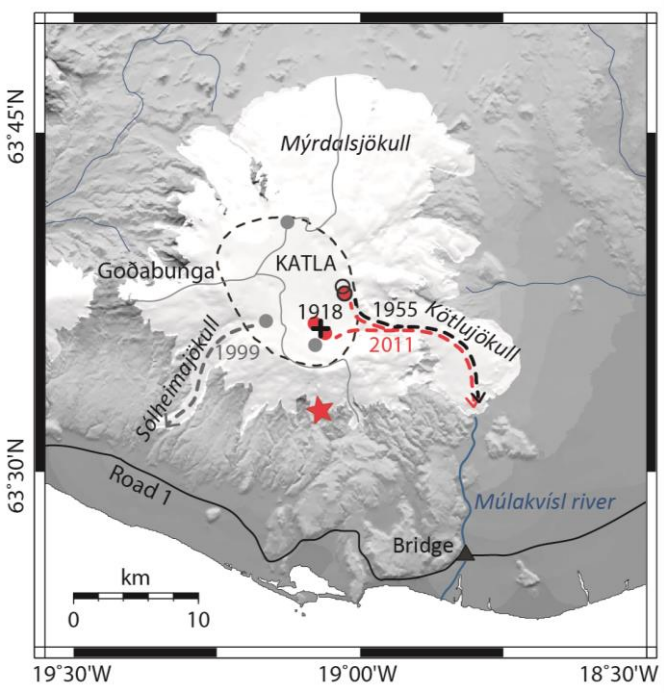

Fig. 2. Recent unrest at Katla. Black cross: 1918 eruption site. Black, grey and red dashed arrows: routes of 1955, 1999 and 2011 jökulhlaups, respectively. Circles with same outline or fill colours mark the cauldrons newly formed or deepened during the same unrest episodes. Red star: new seismic source in the Gvendarfell area. Light grey lines: water divides of main outlet glaciers (Björnsson et al. 2000).

3. Earthquake activity 1998-2015

Catalogue data from the Icelandic Meteorological Office (IMO) have been used to obtain an overview of the seismic activity at Katla during the period 1998-2015, as a framework for the interpretation of the 2011 unrest episode and new seismicity. The seismic data of this catalogue were recorded by the Icelandic national seismic network (SIL) and the earthquake location obtained using a 1D SIL-velocity model (Stefánsson et al. 1993). The permanent monitoring network around Mýrdalsjökull has been densified through time, as shown in Fig. 3. This has a consequence on event detection and localisation accuracy; however it doesn't seem to correlate with the temporal changes in seismicity pattern described below. The depth of the earthquakes is not well resolved, however most events appear to be located at shallow depth between 0 and 5 km (Vogfjörð and Slunga 2008).

This analysis shows significant changes through time in the seasonal patterns, size and location distribution of the persistent seismicity recorded at Katla since the 60ies (e.g. Einarsson and Brandsdóttir 2000). These are the main features:

- The Goðabunga cluster was more active than the caldera until the first half of 2011, with around 11600 events with magnitude Mw>1 compared to 3300 inside the caldera. The most intense seismicity occurred during the 2000-2004 seismic crisis, when inflation was observed at Katla (Sturkell et al. 2008). This sustained earthquake activity started after the 1999 unrest episode (Figs. 4, 5).
- Increased seismicity occurred at Goðabunga following the eruption of Eyjafjallajökull in 2010 (Fig. 4).
- Since July 2011, more events have occurred in the caldera than at Goðabunga, with 1610 events with Mw>1, compared to 760 at Goðabunga (Figs. 4, 5).
- The magnitude of the largest events at Goðabunga has been decreasing since 2009, with most events with Mw<2 as of 2010 (Figs. 4, 5).
- The seasonal correlation of the Goðabunga cluster as described by Soosalu et al. (2006) and Jónsdóttir et al. (2009), with seismicity peaking during fall, is still occurring, but has gradually become less clear (Figs. 4, 5). In addition, the peak of activity seems to have shifted to an earlier time of the year, probably reflecting climate and weather changes.
- The seasonal correlation of the caldera seismicity is less pronounced than at Goðabunga (as already observed in previous studies), but, opposite to Goðabunga, it has become clearer in the past few years, especially in 2012, 2013 and 2014 (Fig. 5).
- A sharp increase in seismicity rate inside the caldera occurred in July 2011, coinciding with the unrest episode and jökulhlaup, and continued until the beginning of 2012 with 660 events with Mw>1 and 20 with Mw>2.5.
- The Gvendarfell seismic cluster on the south flank became active in July 2011 (Fig. 5). It includes nearly all events located on the south flank of Katla (Fig. 3), with the spread of the hypocentres due to location uncertainty. The size of the cluster is in fact very small, on the order of one hundred meters (Sgattoni et al. subm.). The Gvendarfell seismicity appeared to be fading out since February 2015, but the activity has renewed since August 2015, possibly reflecting a delayed summer activity peak due to a colder summer than usual and a high amount of snow deposited in winter time. A slightly increased seismic rate was recorded for a few weeks in July 2014, coinciding with the small unrest episode (Fig. 4).

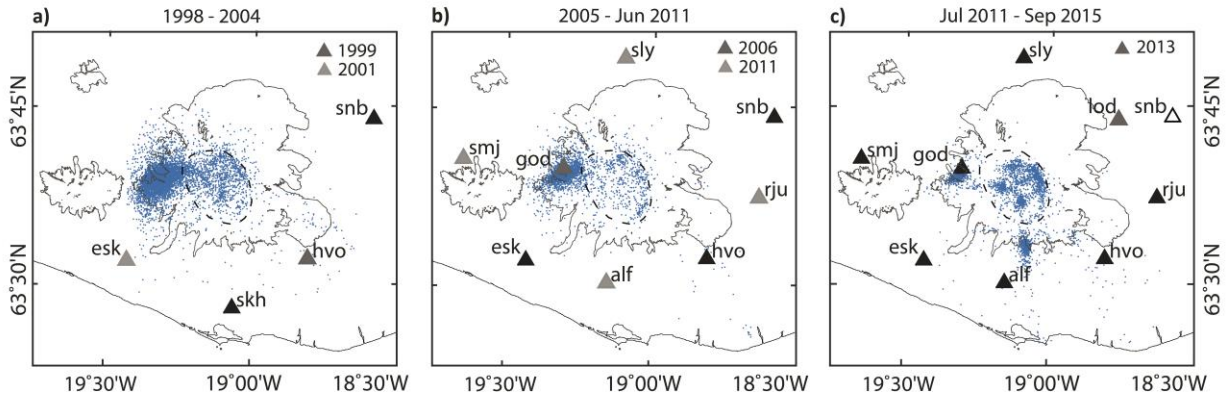

Fig. 3. Earthquake locations (in blue) at Katla during 1998-2015 from IMO catalogue. All events with magnitude M>1 were selected for the caldera and Goðabunga and events with M>0 for the south flank. Black triangles: stations operating during the whole time period of each panel. Grey triangles: stations that were deployed later. Station "snb" in (c) was substituted by "lod" in 2013.

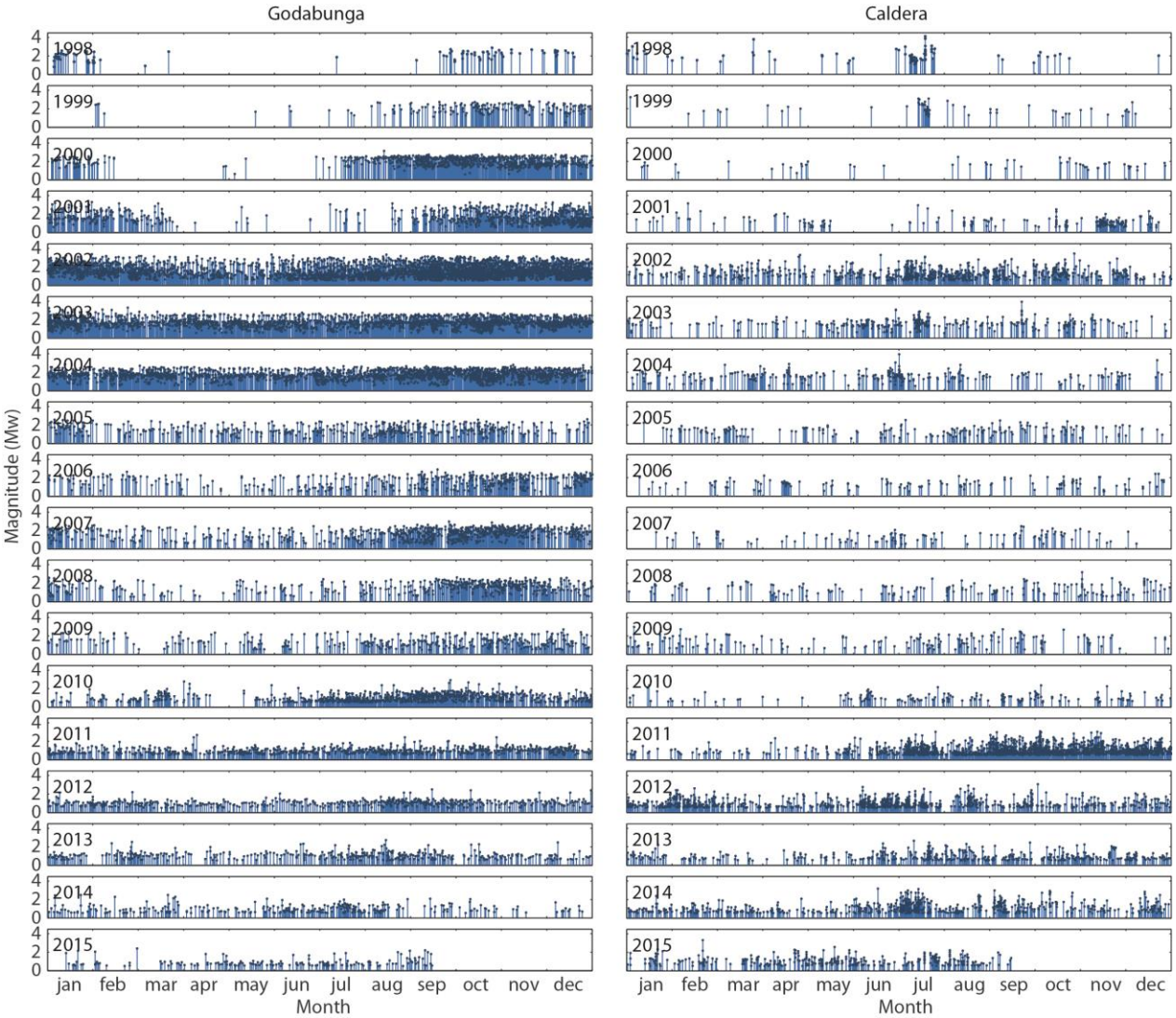

Fig. 4. Magnitude-time evolution of the seismicity at Goðabunga (left) and inside the caldera (right) between January 1998 and September 2015. Data from IMO catalogue.

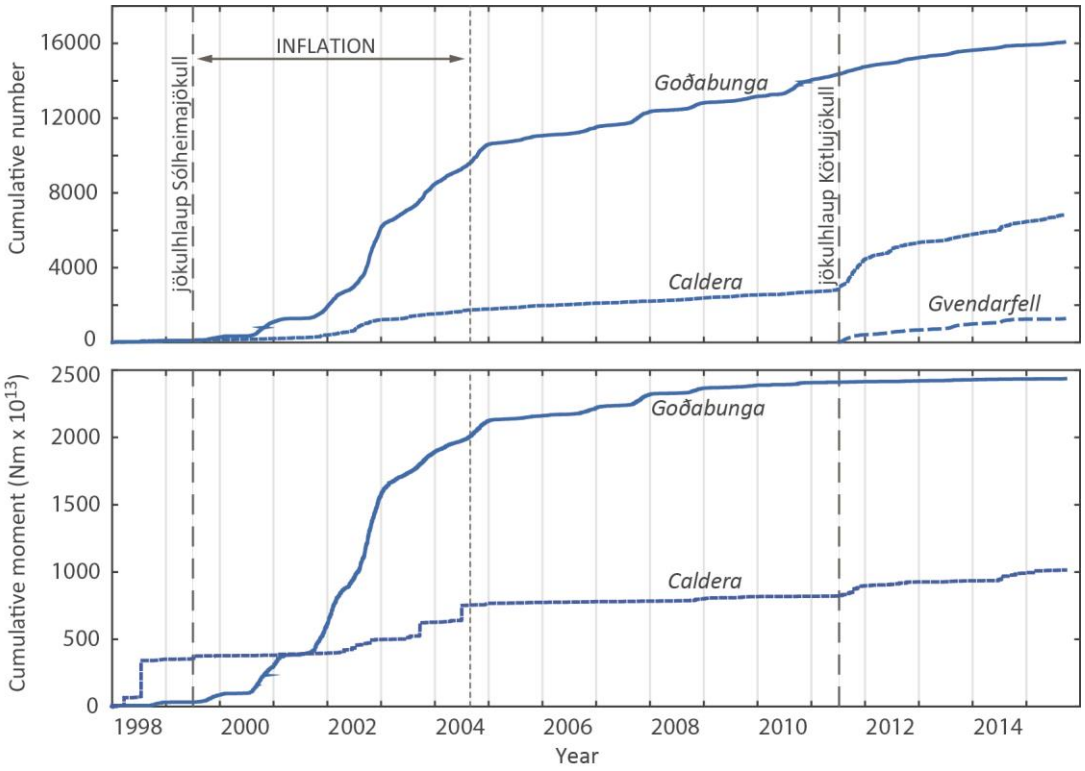

Fig. 5 Cumulative number of events and cumulative seismic moment release between January 1998 and September 2015 in the Goðabunga, caldera and Gvendarfell seismic clusters. The moment-magnitude relation used is $\log M_0 = 1.5M + 9.1$, where M_0 is the moment and M is the magnitude. The Gvendarfell cluster does not appear in the bottom plot because the seismic moment released is too small. The 1999 and 2011 events and the inflation period are marked with dashed lines.

4. Geological features of the Gvendarfell area

A geological field study was carried out on the south flank of Katla in the vicinity of the new 2011 seismic cluster in order to outline the main volcanological and tectonic features possibly relating to seismic sources (Fig. 6). No signs of recent volcanic or hydrothermal activity have been seen in the area.

The 2011 seismic cluster is located outside the southern rim of the caldera near the Gvendarfell rise. This area is partly covered by the Mýrdalsjökull glacier and the exposed region is characterized by flat top ridges bordered by steep cliffs and ravines that were eroded by the fast-retreating Hafursárjökull and Mosakambur glacier streams (Figs. 7a, b). It is known from the literature that the southern and eastern exposed flanks of Katla are characterised by basaltic hyaloclastites and lavas and silicic (rhyolitic and obsidianaceous) lavas, the latter also forming the "nunataks" emerging from the glacier along the caldera rim (Lacasse et al. 2007; Jóhannesson and Saemundsson 2009). However, no detailed description of the geological and structural features is reported.

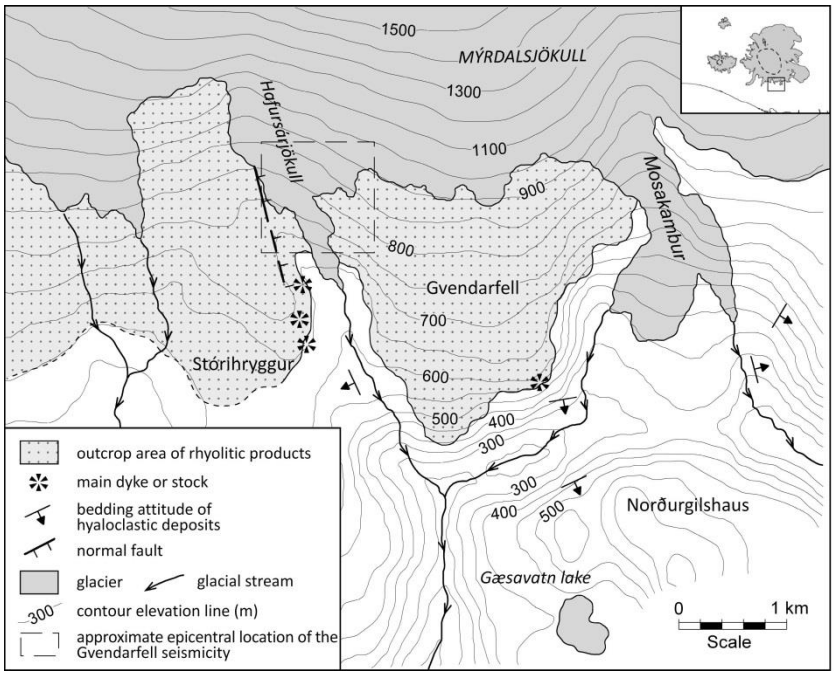

Fig. 6. Schematic map of the main geological features observed in the Gvendarfell and Norðurgilshaus area. The approximate location of the Gvendarfell seismic cluster is also drawn.

These two main lithotypes are recognized in the study area, although the presence of vertical cliffs and steep talus slopes along the ravine walls often makes the fieldwork impossible. A thick (up to 250 meters), laterally-continuous sequence of dark volcaniclastic deposits conforming to the basaltic hyaloclastites identified by Lacasse et al. (2007) is visible in the lower portion of the stratigraphic succession exposed along the Gvendarfell and Stórihryggur ridges (Fig. 6) and constitute the Norðurgilshaus ridge up to the top. The base of this hyaloclastite succession is not exposed. A few outcrops can be studied in detail near the edge of the Norðurgilshaus ridge, showing a crudely-layered succession of dark-coloured hyaloclastites, pillow breccias and compound lava flows, topped by a layer of scoriaceous lapilli and bombs (bread-crust to spindle). Overall, the hyaloclastite succession shows a general radial dipping behaviour around the Gvendarfell ridge (Fig. 6). Towards the top, the hyaloclastites gradually pass to a succession of rhyolitic products, up to ~200 m thick, on both sides of the Gvendarfell ridge. This is the largest rhyolitic unit in the area, and mostly corresponds to the silicic lavas recognized by Lacasse et al. (2007) and Joannesson and Saemundsson (2009) along the southern caldera rim. A number of pale-grey (rhyolitic) lava lobes and dome-shaped bodies with concentric to fan-shaped flow bands and obsidian-rich margins are visible. They are characterised by pervasive prismatic, sub-vertical and fan-shaped to concentric jointing with narrow fracture-spacing on the order of cm to tens of cm (Fig. 7c, d). The top of the Gvendarfell ridge consists of a sequence of tens-of-meters thick,

viscous rhyolitic lava flows with m-scale vertical columnar jointing and a tabular to gently south-wards dipping attitude (Fig. 7c).

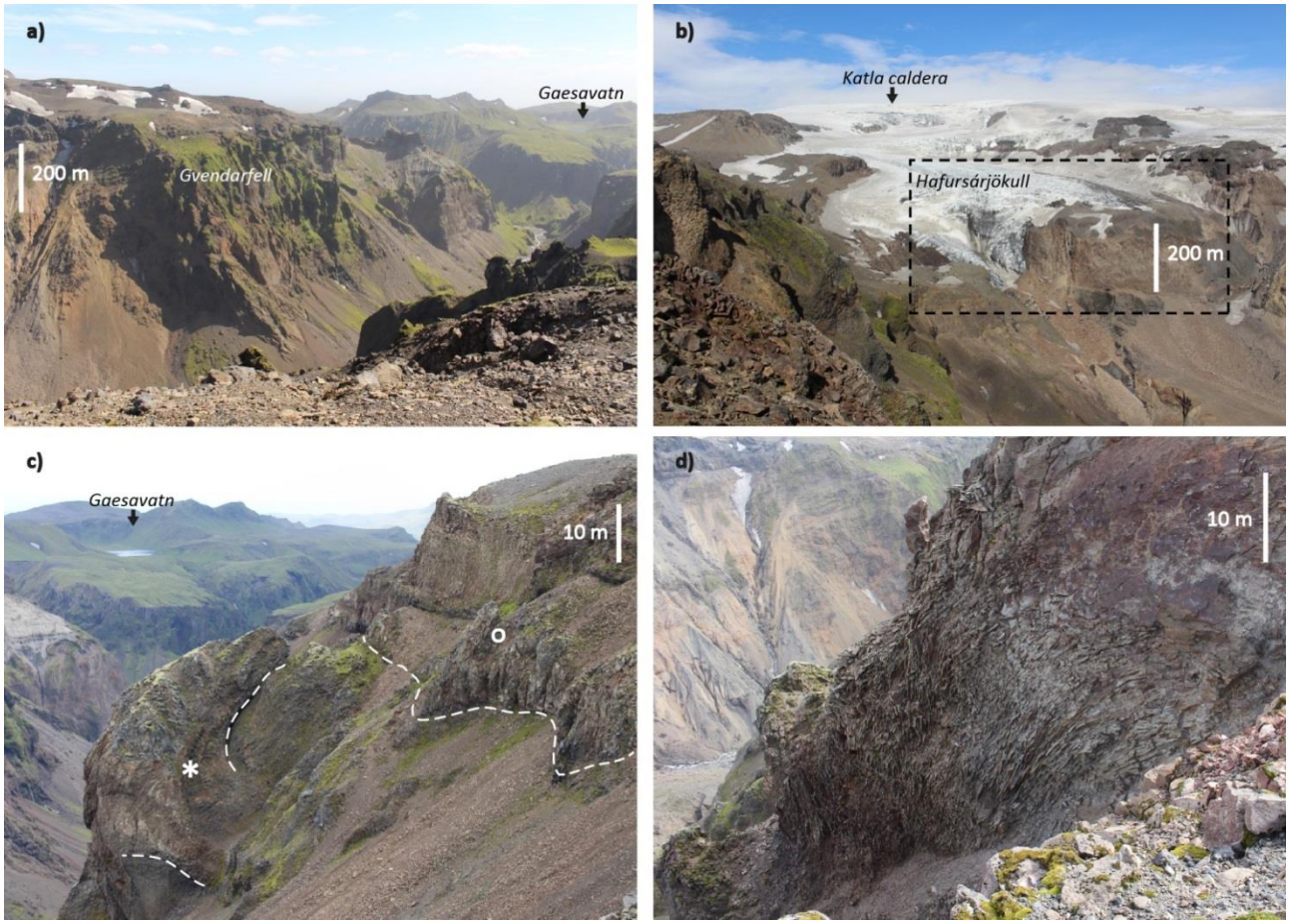

Fig. 7. a) Panoramic view of Gvendarfell ridge from the west. The location of Gæsavatn lake is also indicated. b) View of Hafursárjökull glacier from the South. The dashed box outlines the approximate source area of the seismicity according to Sgattoni et al. (2015). c) Exposure along Stórihryggur ridge of a stock-like lava body (*) embedded within brecciated deposits, which is one of the feeders of the overlying tabular to gently-dipping rhyolitic lava flows (o). d) Detail of a pervasively jointed rhyolitic lava lobe along the Stórihryggur ridge.

Rhyolitic lavas are absent in the Norðurgilshaus ridge. In the NE side of Gæsavatn lake (Fig. 6) the hyaloclastite succession passes upward to a thick succession of massive to crudely-stratified lapilli-tuffs composed of dense glass fragments, vesicular scoriae and rare lithic clasts, with several accretionary lapilli-rich layers (Fig. 8). Low-angle cross-stratification and cm- to dm-scale sandwaves are visible. A few bomb sags (<10 cm) consisting of deeply brecciated mafic lavas are recognized near the ground level, showing a SW-to-NE direction of provenance. Layers of fine ash are interlayered. These volcaniclastic deposits have an overall radial, gentle outward-dip around the Gæsavatn lake, in places showing the opposite dip-

directions typical of crater rims. An anomalous high-angle dip (up to 70°) was observed along a ravine transverse to the sub-rounded geometry of the lake, possibly due to tectonic activity.

No firm conclusions about the eruption types and the environmental conditions during the eruption of the volcanic deposits in the Gvendarfell area can be drawn due to the difficult access to the outcrops, that prevents direct observation of most lithotypes. Nevertheless, the geological and volcanological features generally conform to what has been observed in other areas in Iceland where rhyolitic lava sequences are recognized above hyaloclastite deposits (see Stevenson et al. 2006; Lescinsky and Fink 2000; McGarvie 2009 for a review). Pervasively-jointed rhyolitic lavas embedded within brecciated deposits are described e.g. at Torfajökull (Tuffen et al. 2001, 2008), Öræfajökull (Stevenson et al. 2006) and Prestahnhúkur volcanoes (McGarvie et al. 2007). They are interpreted as ice-chilled rhyolitic lavas erupted in a subglacial environment.

The same interpretation may apply to the rhyolitic lava lobes recognized in the Gvendarfell area, interpreted as dikes or stock-like bodies feeding effusive activity in subglacial conditions that are responsible for the quench-fragmented breccia accumulation that surrounds the lava bodies (Fig. 7c). Some of the lava lobes directly act as feeding points for overlying lava flows. A number of these magma feeders are located along a roughly N-S direction along the border of Stórihryggur ridge (Fig. 6). The presence of magma feeding points around of the Gvendarfell ridge demonstrates that this was an area of lateral magma supply and flank eruption during the recent history of Katla. This interpretation is corroborated by the radial dipping of the hyaloclastic deposits around the Gvendarfell rise in the lower portion of the stratigraphic succession (Fig. 6).

In this scenario, the tabular to gently-dipping lava flows at the top of the succession are likely related to subaerial conditions of effusion, consistent also with the absence of pervasive jointing and of surrounding brecciated deposits. This suggests a progressive melting of the glacier and exhaustion of the melting water due to continuous effusive activity. This is consistent with the occurrence of a strombolian scoriaceous layer with a subaerial character at the top of the Norðurgilshaus ridge. Moreover, the volcaniclastic deposits exposed in the area of Gæsavatn lake have the features of deposits from dilute pyroclastic density currents and associated ballistic fallout typical of surtseyan eruptions developed in shallow-water to subaerial conditions. Their radial outward bedding attitude around Gæsavatn lake, together with the crater-type opposite dipping and the direction of provenance of a few bomb-sags, indicate a possible source area corresponding to the lake.

No radiometric ages are available, but the proposed subglacial (to subaerial) interpretation indicates that the deposits outcropping around Gvendarfell were most likely

emplaced before (or during) the last glacial maximum which occurred in Iceland between 21 and 10 ka BP (Norðdahl 1991a,b). This corresponds to a generic pre-Holocenic age, consistent with the chronologic information by Lacasse et al. (2007) and Jóannesson and Saemundsson (2009). This is also coherent with the presence of deep ravines that were most likely eroded by glacier streams that have retreated after the last glacial maximum. The possibility that more recent phases of activity have occurred during the Holocene cannot be completely underscored.

Notably, we identified a N-S oriented, sub-vertical to gently E-dipping normal fault cutting with a tens-of-meters (vertical) displacement the volcanic succession along the eastern edge of the Stórihryggur ridge (Figs. 6, 9). This fault cuts also a m-thick heterolithological, volcaniclastic deposit with a slope-cone geometry found at the top of the succession (Fig. 9a), which is interpreted as a glacial moraine left by the retreating Hafursárjökull glacier after the end of the last glacial maximum. This indicates that the fault was likely active during the Holocene and possibly in recent times, as also confirmed by the freshness of the fault scarp (Fig. 9b). This demonstrates recent, or even active, tectonic activity in the Gvendarfell area.

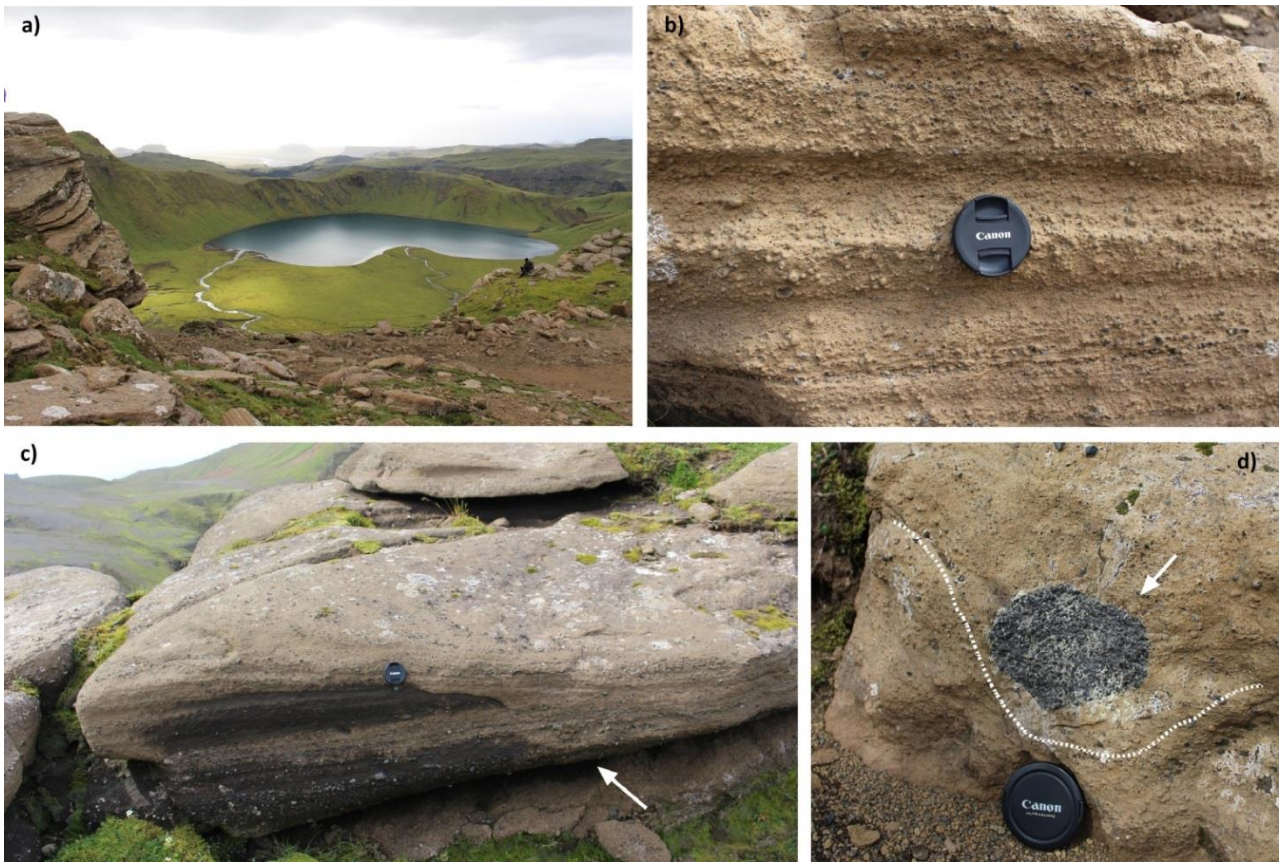

Fig. 8. Volcaniclastic deposits exposed along the NE side of Gæsavatn lake (a), represented by massive to crudely-stratified lapilli tuffs with abundant accretionary lapilli (b), locally showing low-angle cross-stratification and sandwaves (c) and a few bomb-sags (d). In (c) and (d), white arrows indicate the common SW-to-NE direction of provenance of the pyroclastic density currents that emplaced these deposits (based on the bedforms shape) and the ballistic trajectory of the bomb sag.

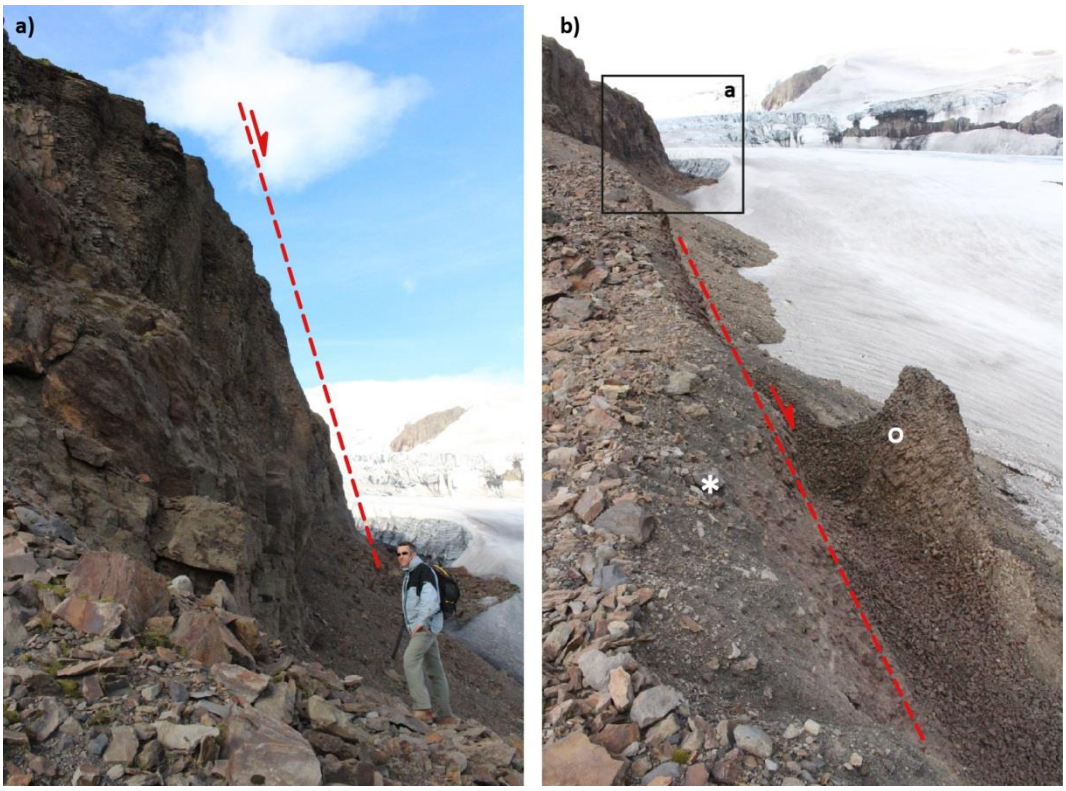

Fig. 9. N-S oriented, sub-vertical (E-dipping) normal fault cutting the volcanic succession along the eastern edge of Stórihryggur ridge. The vertical displacement is on the order of tens of meters (a). The fault scarp is fresh (a) and cuts a volcaniclastic deposit (*) representing the glacial moraine along the retreat trace of the Hafursárjökull glacier stream (b). In (b) a brecciated deposit (o) representing the collapsed part of the volcanic succession is exposed to the right of the fault.

5. Discussion

This unrest coincided with the beginning of a period of intense seismicity inside the caldera that lasted for months and the beginning of a new cluster of earthquakes on the south flank of the volcano, still active at the time of writing (October 2015). Moreover, since 2011 the seismicity rate has become higher inside the caldera than at Goðabunga, differently than before. These are noteworthy changes that are likely related to modifications in the volcanic system, which seem to be indicated also by slight ground deformation observed with GPS between 2011 and 2012 (B.G. Ófeigsson and S. Hreinsdóttir, pers. comm.). However, it is not simple to constrain the origin of these changes. The July 2011 unrest, similarly to the 1955 and 1999 episodes, was not accompanied by direct indication of volcanic activity or a clear deformation field.

As Katla is partly covered by a glacier, it is possible that a part of its persistent seismicity is related to glacial processes, since volcanic and glacial processes can produce similar waveforms (Weaver and Malone, 1976; West et al. 2010). The controversial

interpretation of the Goðabunga seismic cluster is an example (Soosalu et al. 2006; Jónsdóttir et al. 2009). The ground deformation has also controversial interpretations: the 1999-2004 inflation episode has been interpreted in association with either magma accumulation inside the volcano (Sturkell et al. 2006, 2008) or glacial rebound (Spaans et al 2015). In this respect, it is important to notice that the ground deformation coincided with a seismic crisis at Goðabunga that has had no observed equals since and started after the 1999 unrest episode. In addition, the long-term seismicity pattern and the correlation with jökulhlaups and ice-cauldron formation suggest that volcanic processes dominate.

The seasonal peak of seismicity inside the caldera, that usually occurs in July, frequently correlates with small jökulhlaups or increased water drainage from the glacier, associated also with changes in the chemical composition of the water discharged (Wynn et al. 2015). Also, many historical eruptions at Katla occurred during the summer. This indicates that seasonal variations in the geothermal-glacial system may be responsible for these summer peaks, as suggested by Wynn et al (2015). In 1955, 1999 and 2011, the jökulhlaups have been particularly catastrophic and have been accompanied by an increased seismicity rate and occasionally by tremor (in 1999 and 2011), indicating a more dramatic change in the volcanic/geothermal system than usual.

The 2011 event was associated with increased heat released by the volcano as indicated by the water accumulation under the glacier that started a year before (Guðmundsson et al. 2014). The subsequent sudden sinking of ice cauldrons and jökulhlaup that occurred in July 2011, may have been due to a geothermal event, a volcanic (magmatic) event such as a subglacial eruption or a combination of the two, such as a shallow magma intrusion leading to increased geothermal activity. It is not straightforward to draw conclusions about whether a subglacial eruption occurred or not. According to Galeczka et al. (2015), the chemical analysis of floodwater does not show evidence that the water came into contact with magma. The analysis of the tremor suggests that most of the signal is associated with volcano-related processes occurring at the sites of the active cauldrons and an additional small portion of the signal is instead associated with the flood. The duration of the tremor and the inferred velocity of the flood indicate that the tremor burst may have been generated by boiling phenomena and/or explosions induced by the water release from the hydrothermal system (Chapter 5). This would imply that a geothermal source may have sufficed to generate the tremor and the flood, with no need for a magmatic event. However, the notable increase of seismic activity inside the caldera that continued for months after the jökulhlaup is hardly consistent with an exclusively geothermal event and may indicate that the unrest did involve magma, although no eruptive products were identified (Chapter 5). Concerning this, it must be noted that, in a

subglacial volcano like, Katla small eruptions may escape the geological and historical records because they are concealed by the thick glacier.

The absence of clear signs of surface deformation at Katla might be explained by very shallow processes responsible for the persistent seismicity, sometimes evolving into real seismic crises. If, for example, a shallow magma chamber exists, as postulated by Guðmundsson et al. (1994) and the unrest episodes are related to small batches of magma reaching or approaching the surface, the associated deformation signal might be negligible and hidden beneath the glacier. In this scenario, it is important to note that the 1955, 1999 and 2011 unrest episodes occurred in different parts of the caldera, indicating that a large portion of the volcanic system has been activated recently. This could be related to the rise of different, small batches of magma.

Although no evidence of large-scale inflation is currently observed at Katla, the possibility that the volcano is ready or getting ready for an eruption cannot be discarded. It is not unlikely that the edifice is already in an inflated state that was reached before the deformation measurements started. At Krafla, for example, inflation of the edifice occurred right after the 1975-1984 rifting episode and since then the volcano has been slowly deflating, but the pressure inside the edifice is currently on the same order as before the rifting episode (Buck et al. 2006). The scenario at Katla may be similar and rapid inflation might have occurred after the last 1918 eruption. Accordingly, the persistent seismicity may reflect the processes taking place in a pressurized system persistently close to failure. The 1955, 1999 and 2011 episodes might be signs of this. If this was the case, these unrest episodes would represent important warnings, because they occurred suddenly with no precursory activity and could have triggered a bigger eruption, or could do it in the future.

The 2011 unrest marked not only the beginning of increased seismicity inside the caldera, but also a new seismic source on the south flank. Sgattoni et al.(2015) proposed that these events may be associated with a shallow hydrothermal system activated in association with the unrest episode, although no direct evidence of hydrothermal activity was found. A possible connection to magmatic processes cannot be ruled out. The geological study of the Gvendarfell area demonstrated that the south flank of Katla acted as a source area for flank eruptions during its pre-Holocene (to recent?) history. One source is represented by the Gvendarfell ridge, which is characterized by several lava domes and lobes feeding a rhyolitic lava succession that fills a largely eroded hyaloclastite crater inferred from the radial outward dipping of the hyaloclastite deposits. Another source is the Gæsavatn lake, located south of Gvendarfell, which is a surtseyan crater, as shown by the radial outward dipping of the surtseyan deposits exposed along its NE side and the direction of provenance of a few bomb-

sags. The occurrence of flank eruptions on the southern flank of Katla outside the caldera is an important finding that was never pointed out before. This implies that volcanic activity has already occurred in the same area where the current south-flank seismicity is recorded. It is therefore plausible that the Gvendarfell seismic cluster is related to renewed volcano-related processes. As an example, the (small) lava bodies of silicic composition exposed in the Gvendarfell area are comparable in size to the volume occupied by the hypocentre distribution that was obtained from relative relocation (Sgattoni et al. 2015). The intrusion of a similar lava body should therefore be taken into account as a possible source for the seismic events.

The volcanic succession cropping out in the Gvendarfell area seems to belong to a pre-Holocenic stage of Katla's volcanic activity, however no radiometric information is available to date these deposits. There is also evidence for recent tectonic activity, testified by a normal fault exposed on the west side of Hafursárjökull glacier. Our pilot geological study of the Gvendarfell area has highlighted volcanic features and new scenarios for the Katla's eruptive history and, possibly, future activity. In light of the new seismic activity in this area, further studies are needed to better constrain the volcanic history of the south flank, possibly also with new radiometric dating.

6. Conclusions

The 2011 unrest episode marked a clear change of the seismicity pattern at Katla volcano. It was characterized by a sudden jökulhlaup, tremor bursts originating at the source of the water flood (were ice cauldrons deepened), increased earthquake activity inside the caldera and the appearance of a new source of earthquakes on the south flank. This change likely highlights a modification of the volcanic system, likely involving magma movements.

The 2011 unrest, similarly to the 1955 and 1999 episodes, may have involved hydrothermal system or magma movements, possibly a small subglacial eruption. All unrest episodes were apparently accompanied by only small deformation fields. In the absence of evidence for recent large scale recharging of a magma chamber beneath Katla, it may be speculated whether Katla is already in an inflated state, having inflated immediately following the latest large 1918 eruption. This may be the cause of the persistent seismicity at Katla. In that case a small event like the ones of 1955, 1999 and 2011, may be sufficient to trigger a large eruption in the future.

The 2011 unrest motivated a pilot study of the geology of the south flank in the source area of the new seismicity. We have found evidences that flank eruptions occurred during the pre-Holocene (to recent) history of the volcano. We have identified two sources in particular, of different types. One is the Gvendarfell ridge, characterized by rhyolitic lava domes and lobes

feeding the overlying rhyolitic lava succession filling a hyaloclastite crater. The other one is Gæsavatn lake, a surtseyan crater associated with airfall and pyroclastic density currents deposits.

Since volcanic activity has occurred in the same area where the south-flank seismicity is recorded, magma movements (e.g. rising of magma batches) should not be neglected as a potential seismic source. This study also opens new scenarios for hazard and risk assessment of the south flank of Katla, where the village of Vík is located. It also underscores the need for further research on the flank areas of Katla.

References

Björnsson H, Pálsson F, Guðmundsson MT (2000) Surface and bedrock topography of the Mýrdalsjökull ice cap, Iceland: The Katla caldera, eruption sites and routes of jökulhlaups. Jökull 49:29-46

Buck WR, Einarsson P, Brandsdóttir B (2006) Tectonic stress and magma chamber size as controls on dike propagation: Constraints from the 1975-1984 Krafla rifting episode. J Geophys Res-Sol Ea 111:1–15. doi:10.1029/2005JB003879

Budd DA, Troll VR, Dahren B, Burchardt S (2014) Persistent shallow magma storage beneath Katla Volcano. Paper presented at: Goldschmidt Annual Meeting, Sacramento, USA

Eggertsson S (1919) Ymislegt smavegis vidvıkjandi Kotlugosinu 1918. Eimreidin 25:212–222

Einarsson EH, Larsen G, Thorarinsson S (1980) The Sólheimar tephra layer and the Katla eruption of ~1357. Acta Naturalia Islandica 28:2–23

Einarsson P (1991) Earthquakes and present-day tectonism in Iceland. Tectonophysics 189:261–279

Einarsson P, Brandsdóttir B (2000) Earthquakes in the Mýrdalsjökull area, Iceland, 1978–1985: Seasonal correlation and relation to volcanoes. Jökull 49:59–73

Galeczka I, Oelkers EH, Gislason SR (2014) The chemistry and element fluxes of the July 2011 Múlakvísl and Kaldakvísl glacial floods, Iceland. J Volcanol Geotherm Res 273:41–57. doi:10.1016/j.jvolgeores.2013.12.004

Geirsson H, Arnadóttir Th, Volksen C, Jiang W, Sturkell E, Villemin T, Einarsson P, Sigmundsson F, Stefánsson R (2006) Current plate movements across the Mid-Atlantic Ridge determined from 5 years of continuous GPS measurements in Iceland. J Geophys Res 111:B09407.

Grönvold K, Oskarsson N, Johnsen SJ, Clausen HB, Hammer CU, Bond G, Bard E (1995) Ash layer from Iceland in the Greenland GRIP ice core correlated with oceanic and land sediments. Earth Planet Sci Lett 135:149–155

Guðmundsson Ó, Brandsdóttir B, Menke W, Sigvaldason G.E. (1994) The crustal magma chamber of the Katla volcano in South Iceland revealed by 2-D seismic undershooting. Geophys J Int 119:277–296

Guðmundsson MT, Högnadóttir Þ, Kristinsson AB, Guðbjörnsson S (2007) Geothermal activity in the subglacial Katla caldera, Iceland, 1999–2005, studied with radar altimetry. Ann Glaciol 45:66–72

Guðmundsson MT, Larsen G, Sigmarsson O (2013) In: Sólnes J, Sigmundsson F, Bessason B (ed) Náttúruvá á Íslándi. Eldgos og jarðskjálftar. Viðlagatrygging Íslands/Háskólaútgáfan, pp 2013

Jakobsdóttir SS, 2008 Seismicity in Iceland: 1994–2007. Jökull 58:75–100

Jakobsson SP (1979) Petrology of recent basalts of the eastern volcanic zone, Iceland. Acta Naturalia Islandica 26:1–103

Jonsson G, Kristjansson L (2000) Aeromagnetic measurements over Mýrdalsjökull and vicinity. Jökull 49:47–58

Jóhannesson H, Saemundsson K (2009) Geological Map of Iceland. 1:600.000. Bedrock Geology. Icelandic Institute of Natural History, Reykjavík (1st edition).

Jónsdóttir K, Roberts R, Phjola V, Lund B, Shomlai ZH, Tryggvason A, Böðvarsson R. (2009) Glacial long period seismic events at Katla volcano, Iceland. Geophys Res Lett, 36:L11402

Jónsdóttir K, Tryggvason A, Roberts R, Lund B, Soosalu H, Böðvarsson R (2007) Habits of a glacier covered volcano: seismicity and a structure study of the Katla volcano, South Iceland. Ann Glaciol 45:169–177

Lacasse C, Carey SN, Sigurðsson H (1998) Volcanogenic sedimentation in the Iceland Basin: influence of subaerial and subglacial eruptions. J Volcanol Geoth Res 83:47–73

Lacasse C, Sigurðsson H, Carey SN, Jóhannesson H, Thomas LE, Rogers NW (2007) Bimodal volcanism at the Katla subglacial caldera, Iceland: Insight into the geochemistry and petrogenesis of rhyolitic magmas. B Volcanol 69:373–399

Larsen G (2000) Holocene eruptions within the Katla volcanic system, south Iceland: characteristics and environmental impact. Jökull 49:1–28

Larsen G, Newton AJ, Dugmore AJ, Vilmundardóttir EG (2001) Geochemistry, dispersal, volumes and chronology of Holocene silicic tephra layers from the Katla volcano system, Iceland. J Quat Sci 16:119–132

Lescinsky DT, Fink JH (2000) Lava and ice interaction at stratovolcanoes: use of characteristic features to determine past glacial extents and future volcanic hazards. J Geophys Res 105(B10): 23,711–23,726

McGarvie D (2009) Rhyolitic volcano-ice interactions in Iceland. J Volcanol Geoth Res 185:367–389. doi:10.1016/j.jvolgeores.2008.11.019

Norðdahl H (1991a) Late Weichselian and Early Holocene deglaciation of Iceland. Jökull 40:27–50

Norðdahl H (1991b) A review of the glaciation maximum concept and the deglaciation of Eyjafjordur, North Iceland. In: Maizels JK, Caseldine C (ed) Environmental Change in Iceland: Past and Present. Kluwer Academic Publishers, Netherlands, pp 31–47

Óladóttir BA, Larsen G, Thordarson Th, Sigmarsson O (2005) The Katla volcano, S-Iceland: holocene tephra stratigraphy and eruption frequency. Jökull 55:53–74

Roberts MJ, Tweed FS, Russell, AJ, Knudsen Ó, Harris TD (2003) Hydrological and geomorphic effects of temporary ice-dammed lake formation during jökulhlaups. Earth Surf Processes Landforms 28:723–737

Sgattoni G, Guðmundsson Ó, Einarsson P, Lucchi, F Relative relocation of earthquakes without a predefined velocity model: an example from a peculiar seismic cluster on Katla volcano's south-flank (Iceland). Submitted to J Geoph Int

Sgattoni G, Jeddi Z, Guðmundsson Ó, Einarsson P, Tryggvason A, Lund B, Lucchi, F (2015) Long-period events with strikingly regular temporal patterns on Katla volcano's south flank (Iceland). arXiv:1511.05852 http://arxiv.org/ftp/arxiv/papers/ .

Sigurðsson O, Zóphoníasson S, Ísleifsson E (2000) Jökulhlaup úr Sölheimajökli 18. júlí 1999 (The jökulhlaup from Sólheimajökull July 18, 1999, in Icelandic with English summary). Jökull 49:75–80

Soosalu H, Jónsdóttir K, Einarsson P (2006) Seismicity crisis at the Katla volcano, Iceland – signs of a cryptodome? J Volcanol Geoth Res 153:177–186

Spaans K, Hreinsdóttir S, Hooper A, Ófeigsson B.G. (2015) Crustal movements due to Iceland's shrinking ice caps mimic magma inflow signal at Katla volcano. Sci Rep 5, 10285. doi: 10.1038/srep10285

Stefánsson R, Böðvarsson R, Slunga R, Einarsson P, Jakobsdóttir S, Bungum H, Gregersen S, Havskov J, Hjelme J, Korhonen H (1993) Earthquake prediction research in the south Iceland seismic zone and the SIL project. B Seismol Soc Am 83(3):696–716

Stevenson JA, McGarvie DW, Smellie JL, Gilbert JS (2006) Subglacial and ice-contact volcanism at the Öræfajökull stratovolcano, Iceland. B Volcanol 68:737–752. doi:10.1007/s00445-005-0047-0

Sturkell E, Einarsson P, Sigmundsson F, Geirsson H, Ólafsson H, Pedersen R, de Zeeuw-van Dalfsen E, Linde AT, Sacks SI, Stefánsson R (2006) Volcano geodesy and magma dynamics in Iceland. J Volcanol Geoth Res 150:14–34. doi:10.1016/j.jvolgeores.2005.07.010

Sturkell E, Einarsson P, Roberts MJ, Geirsson H, Guðmundsson MT, Sigmundsson F, Pinel V, Guðmundsson GB, Ólafsson H, Stefánsson R (2008) Seismic and geodetic insights into

magma accumulation at Katla subglacial volcano, Iceland: 1999 to 2005. J Geophys Res 113(B03212)

Sturkell E, Einarsson P, Sigmundsson F, Hooper A, Ófeigsson BG, Geirsson H, Ólafsson H (2010) Katla and Eyjafjallajökull Volcanoes. In: Schomacker A, Krüger J, Kjær KH (ed) The Mýrdalsjökull icecap, Iceland. Glacial processes, sediments and landforms on an active volcano. Developments in Quaternary Science 13. Elsevier, Amsterdam. ISBN 1571-0866, pp 5–21

Sveinsson G (1919) Kotlugosid 1918 og afleidingar thess (The Katla eruption of 1918 and its consequences). Reykjavık, Prentsmidja Gutenbergs, pp 61

Sæmundsson K (1982) Calderas in active volcanic regions in Iceland (in Icelandic). Eldur er í Norðri, Reykjavík, Sögufélag, pp 221–239

Thorarinsson S (1975) Katla og annáll Kötlugosa. Árbók Ferðafélags Íslands. Ferðafélag Íslands, Reykjavık, 125–149

Thordarson T, Larsen G (2006) Volcanism in Iceland in historical time: Volcano types, eruption and eruptive history. J Geodyn. doi:10.1016/j.jog.2006.09.005

Thordarson T, Miller DJ, Larsen G, Self S, Sigurðsson H (2001) New estimates of sulfur degassing and atmospheric mass-loading by the 934 AD Eldgjá eruption, Iceland. J Volcanol Geoth Res 108:33–54

Tuffen H, McGarvie DW, Pinkerton H, Gillbert JS, Brooker RA (2008) An explosive-intrusive subglacial rhyolite eruption at Dalakvisl, Torfajokull, Iceland. B Volcanol 70: 841-860

Tuffen H, Gilbert J, McGarvie DW (2001) Products of an effusive subglacial rhyolite eruption: Bláhnúkur, Torfajökull, Iceland. B Volcanol 63:179–190

Vogfjörð K, Slunga R (2008) Imaging subsurface mass movement through relative earthquake locations in the Katla volcano, Iceland, and the possible location of a magma chamber. Reykjavık, Iceland, IAVCEI General Assembly.

Weaver CS, Malone SD (1979) Seismic evidence for discrete glacier motion at the rock-ice interface. J Glaciol 23:171– 184

West ME, Larsen CF, Truffer M, O'Neel S, LeBlanc L (2010) Glacier microseismicity. Geology, 38(4):319–322. doi:10.1130/G30606.1

Wynn PM, Morrell DJ, Tuffen H, Barker P, Tweed FS, Burns R (2015) Seasonal release of anoxic geothermal meltwater from the Katla volcanic system at Sólheimajökull, Iceland. Chem. Geol. 396:228–238. doi:10.1016/j.chemgeo.2014.12.026

7. CONCLUSIONS

The July 2011 unrest marked a significant change in the seismicity pattern at Katla volcano. Since the beginning of July 2011, the seismicity intensified inside the caldera and on July 8-9th a 23 hour tremor burst was recorded. No eruption broke the ice surface but a sudden jökulhlaup drained from the south-east Mýrdalsjökull glacier and three ice cauldrons deepened in the southern and eastern parts of the caldera. Before the jökulhlaup, a few meters uplift of some ice cauldrons was observed. In addition, together with increased earthquake activity inside the caldera, a new area on the south flank of Katla near Gvendarfell became seismically active.

A detailed study of the tremor burst and features of the new southern seismicity has been carried out in order to suggest possible source interpretations. The changes of the seismicity pattern that occurred in 2011 have been analysed using the seismic catalogue in the years 1998-2015. This information, integrated with a review of the geological and eruptive history of Katla and a pilot geological study of the Gvendarfell area, where the new seismicity is located, allowed to discuss the volcanological implications of the 2011 unrest.

Particular care has been dedicated to optimize the methods used for signal analysis and for the location of the tremor and earthquake sources. A new cross-correlation method, based on double cross-correlation rather than the single cross-correlation previously used by other authors, was used for the volcanic tremor location. This method has improved significantly the resolution of the source energy distribution and higher order correlation methods appear to be promising tools to further optimize volcanic tremor location.

A relative-relocation method has been specifically designed to locate the Gvendarfell seismic events. This was required by the extreme similarity of all waveforms, suggesting a very small spatial distribution of hypocentres, and by the strong crustal heterogeneities affecting wave propagation. The differential-time measurements have been optimized to minimize uncertainty and the relocation strategy has been designed to relocate events without a predefined velocity model, inverting instead for changes in location and for slowness. This relocation strategy has considerably improved the data fit. A careful estimation of uncertainty has also been conducted, in order to evaluate the resolved size of the hypocentre distribution. This was in turn relevant information that helped constraining the source process.

As shown by the seismic catalogue provided by IMO for the last 17 years, the whole seismic activity of Katla until the middle of 2011 has been located inside the caldera and at Goðabunga, the latter being much more active. In July 2011, intense seismicity began inside the caldera and lasted until January 2012. At the same time, the new Gvendarfell seismic cluster became active on the south flank of Katla. Since July 2011, the seismicity rate inside the caldera has become higher than at Goðabunga. This highlights a modification of the volcanic system, likely involving magma movements. This hypothesis is supported by indication of inflation between 2011 and 2012 from GPS data.

The analysis of the tremor signal revealed that the tremor consists of three different components that were identified and described based on amplitude and frequency features. One tremor phase, dominated in amplitude by the station closest to the river that flooded south-east of Mýrdalsjökull glacier, is associated with the jökulhlaup. The other two tremor phases constitute most of the tremor signal and have been located with cross-correlation methods in two source areas close to the ice cauldrons that deepened in the eastern and southern sectors of the caldera. These two source areas are interpreted to be associated with either hydrothermal processes, such as boiling of the hydrothermal fluid, or volcanic processes with magma involved, possibly a subglacial eruption or magma intrusion. A combination of the two, e.g. increased hydrothermal activity induced by a shallow intrusion, is also possible. The occurrence of volcanic processes involving magma is indicated by i) the increased seismicity inside the caldera that started a few days before the jökulhlaup, ii) the evidence of rapid sinking of ice cauldrons that led to the glacial flood. On the other hand, the duration of the tremor signal, compared to plausible travel times for the flood from the source to the river, suggests that it is also possible that the tremor was generated by boiling and/or explosions induced in the hydrothermal system by the pressure drop triggered when the water started to flow out of the subglacial hydrothermal system. Any interpretation requires an increase of heat released by the volcano, as suggested by the water accumulation under the glacier before the tremor (indicated by uplift of the ice cauldrons).

The seismicity that started on the south flank in July 2011 is still active and consists of shallow, repeating LP seismic events located at the southern edge of Mýrdalsjökull glacier. They occur at regular time intervals with a seasonal modulation with the highest frequency of occurrence in the summer time. These seismic events are significantly different from other LP events at Katla and, although some of their features are similar to those observed for LP events at other volcanoes worldwide, they represent a peculiar case study because of their temporal evolution. The non-linear absolute location of the cluster, with ~400 m horizontal uncertainty, corresponds to the outer margin of the small, fast retreating Hafursárjökull glacier stream. The absolute depth location is not resolved well enough to be discerned from the surface, therefore a glacial origin of the Gvendarfell events, such as glacier sliding and ice-falls, cannot be ruled out. However, the thickness of the ice in this area is not likely to exceed few tens of meters, while the depth distribution of the hypocentres, as estimated from relative relocation, is on the order of 100 m. Moreover, it is unlikely that such a small glacier stream can produce such remarkably stable seismicity over years. These arguments, together with the temporal coincidence of the onset of the Gvendarfell seismicity with the July 2011 unrest episode, suggest that volcano-related processes are more likely than glacial to generate this seismicity. Among volcano-related processes, a hydrothermal source appears more likely than magma movement, mainly because of the marked seasonal correlation of the seismicity, which appears easier to reconcile with a source involving water. The similarity of the waveforms over a long time (at least 3.5 years) indicates a stable, non-destructive source mechanism and the regular temporal pattern suggests that the process must be controlled by a critical parameter such as a temperature-pressure condition. These features may be consistent with a steady process of heating and cooling (geyser-like) of a hydrothermal fluid. In this scenario, the seasonal correlation may be explained as a response to the summer ice melting that increases the water supply to the system. Therefore, it is possible that a small hydrothermal system was activated on the south flank of Katla in coincidence with the July 2011 unrest episode. This may have been powered by either a short lived dike intrusion or a crack connection to a heat source established during the unrest. As no evidence for hydrothermal activity has been found in the area, this hydrothermal system has to be entirely concealed by the glacier or acting below the ground surface.

The possible occurrence of hydrothermal or magmatic activity on the south flank of Katla is a new finding. This is supported by the geological field study in the Gvendarfell area that has revealed evidence for flank eruptions during the pre-Holocene to recent eruptive history of Katla. In particular, two sources were identified, of different types. One is represented by the Gvendarfell ridge where several lava domes and lobes were found feeding a rhyolitic lava succession overlying thick hyaloclastite deposits with a radial outward dipping

around the Gvendarfell ridge. The other source corresponds to Gæsavatn lake, a surtseyan crater located south of Gvendarfell, associated with hyaloclastite to surtseyan deposits exposed along the NE side of the lake. These deposits show a radial outward dipping and contain a few bomb sags originated from the direction of the lake. These results reveal that magma movements, such as rising small magma batches, should not be discarded as a potential source for the Gvendarfell seismicity or even for future flank eruptions at Katla. This has important impact on the assessment of volcanic hazard for the south flank of Katla.

As a final remark, this study has further highlighted the difficulty and importance of discriminating glacier-related and volcano-related seismic sources at subglacial volcanoes, for both tremor and earthquake activity.